CONTACT MODELING AND DIRECTIONAL ADHESION FOR CLIMBING ROBOTS

A DISSERTATION
SUBMITTED TO THE DEPARTMENT OF MECHANICAL
ENGINEERING
AND THE COMMITTEE ON GRADUATE STUDIES
OF STANFORD UNIVERSITY
IN PARTIAL FULFILLMENT OF THE REQUIREMENTS
FOR THE DEGREE OF
DOCTOR OF PHILOSOPHY

Daniel Oliveira Santos
October 2007

UMI Number: 3292413

INFORMATION TO USERS

The quality of this reproduction is dependent upon the quality of the copy submitted. Broken or indistinct print, colored or poor quality illustrations and photographs, print bleed-through, substandard margins, and improper alignment can adversely affect reproduction.

In the unlikely event that the author did not send a complete manuscript and there are missing pages, these will be noted. Also, if unauthorized copyright material had to be removed, a note will indicate the deletion.

UMI®

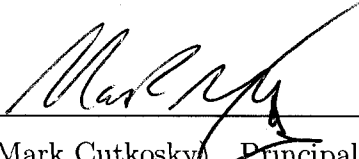I certify that I have read this dissertation and that, in my opinion, it is fully adequate in scope and quality as a dissertation for the degree of Doctor of Philosophy.

(Mark Cutkosky) Principal Adviser

I certify that I have read this dissertation and that, in my opinion, it is fully adequate in scope and quality as a dissertation for the degree of Doctor of Philosophy.

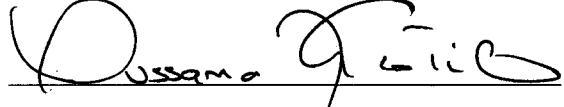(Kenneth Waldron)

I certify that I have read this dissertation and that, in my opinion, it is fully adequate in scope and quality as a dissertation for the degree of Doctor of Philosophy.

(Oussama Khatib)

Approved for the University Committee on Graduate Studies.

Abstract

Climbing robots have the potential to perform a variety of useful tasks including maintenance, exploration, and search and rescue. Unfortunately, current climbing robots have not achieved robust performance in unstructured real-world environments, except when tasked with very limited and specific goals. Examples from Nature, such as the gecko lizard, can provide insight for achieving a new level of robot performance, potentially able to climb a wide range of surfaces and materials.

Developing such robots requires a detailed understanding of the interaction between the feet and the climbing substrate. Climbing is a relatively new challenge for legged robots and there has been little previous work on adhesion models specifically for climbing. The adhesive characteristics of the contact govern the magnitudes of forces that can be applied at the feet without them popping off or slipping along the surface. Classical contact and adhesion models between elastic materials, as well as most synthetic adhesives, are not able to describe the adhesion systems observed in animals such as the gecko lizard.

The gecko lizard is able to climb vertical and even overhanging surfaces composed of materials ranging from glass to painted wallboard. Its adhesion system contains an important property necessary for robust climbing — directionality. A new adhesion model, termed Frictional Adhesion, captures the directionality of the gecko's adhesive system. This model differs from many previous adhesive models and provides distinct advantages for climbing vertical surfaces.

A new synthetic adhesive is presented that duplicates the directionality of the gecko adhesion system. Directional adhesives present new challenges when testing and characterizing their adhesive qualities compared to non-directional adhesives.

A custom experimental setup and procedures used for testing this adhesive are described. Results characterizing the adhesive are given and its ability to duplicate the directionality of the gecko adhesion system is discussed.

The nature of directional adhesion also presents new considerations for the design and control of climbing robots. Simplified two- and three-dimensional analyses highlight the differences between non-directional and directional adhesion models. In many cases the optimal force control and foot orientation strategies are quite different when using directional adhesion as opposed to conventional, isotropic adhesion. These simple models also explain some of the climbing behaviors seen in gecko lizards.

Directional adhesion enables control of the adhesion forces, which in turn facilitates smooth attachment and detachment of feet and robust climbing. However, appropriate use of directional adhesion necessitates added consideration of the force distribution to and orientation of the feet. With proper application, directional adhesion can greatly improve overall performance in climbing robots.

Para os meus pais,
Fernando Bastos dos Santos e Ilda Marques de Oliveira Santos

Acknowledgment

I would not have been able to complete this dissertation without support from the people in my life.

I would like to thank the following people who have helped make this possible: First and foremost, my adviser, Prof. Mark Cutkosky, who gave me the opportunity and guidance necessary to pursue this research. Prof. Kellar Autumn for many useful collaborations and discussions on the gecko adhesion system. My reading committee members, Prof. Kenneth Waldron and Prof. Oussama Khatib. Sangbae Kim, for providing me with many samples of synthetic directional adhesives to test. All of the current and past members of BDML. Dr. Noe Lozano and the Dean's Doctoral Diversity Fellowship for funding during my Masters degree. Prof. Channing Robertson, Prof. Jim Swartz, and the NIH-Stanford Biotechnology Training Grant for funding during my Doctoral degree.

Most importantly, I would like to thank my family, especially mom and dad, for their love and support, as well as all the friends I have been lucky to have over the years.

Contents

List of Tables

List of Figures

Chapter 1

Introduction

While the idea of robots has existed for centuries, it is only in the last fifty years that robots have begun performing useful tasks. The first significant application of robotics was in industrial automation where robots range from simple pick-and-place machines to multi-jointed serial-chain manipulators used for manufacturing automobiles. These types of robots perform well-defined tasks in structured environments and will continue to be an important part of robotics.

However, recent research in robotics has been driven by a desire to create robots capable of functioning in unstructured and unknown environments. One such topic area is locomotion [68, 101]. Robots that are able to maneuver around obstacles and traverse terrain ranging from hard asphalt to a sandy beach possess the capability of revolutionizing the day-to-day aspects of human life. Walking and running robots that can interact with humans have recently started to appear [51, 98]. While this field will continue to grow, many researchers have now turned their attention to climbing [1, 114]. This thesis focuses specifically on the study of climbing robots using Nature as a source of inspiration.

1.1 Motivation

Climbing robots have the potential to perform tasks that are difficult, dangerous, and/or simply impossible for humans to do. Many researchers have already created

climbing robots to perform very specific tasks. Such tasks include maintenance [46, 83, 119] and exploration [10, 67]. Other research has studied climbing more generally [24, 79]. While much progress has been made in this field, researchers are far from developing robots capable of climbing unstructured environments in a robust fashion.

When it comes to the problem of locomotion, Nature has produced a variety of solutions that can provide a source of inspiration for science and engineering. Geckos, squirrels, and frogs are all good examples of biological solutions to the climbing problem. Geckos in particular are arguably Nature's best climbers, able to climb vertical and overhanging surfaces including glass, painted wallboard, and trees [8]. Because of this, the gecko has become a major topic of study in the fields of adhesion and climbing robotics [11, 68].

This thesis will use the gecko adhesion system to gain insight into important climbing principles. These principles can then be used to further the development of climbing robots for the benefit of mankind.

1.2 Thesis Outline

The field of climbing robots can be thought of as the intersection of two other well-studied fields — the study of running and walking robots and the study of grasping and dexterous manipulation. In running and walking, the kinematics and dynamics of the system largely dictate the overall performance [68, 93]. In contrast, grasping is much more concerned with the forces acting at the contacts of the system [26, 65]. Legged climbing involves the application of forces at the foot-substrate contacts in order to propel the body upwards. It combines grasping and locomotion since the limbs must grab on to the wall while the body must also ascend the wall.

This thesis focuses on the grasping aspects of climbing, specifically the contact interaction between the feet and the substrate. In the study of horizontal locomotion it is sometimes possible to ignore the contact details or use a simple friction model to describe the contact. The interaction forces transmitted between the feet and the substrate become much more important when climbing because failures can be catastrophic. First and foremost, unlike horizontal locomotion, climbing vertical flat

surfaces requires adhesion. Simple friction models are insufficient to study climbing and new contact descriptions that properly capture the nature of adhesion are required. These adhesive contacts dictate the magnitudes and directions of forces that can be applied at the feet and ultimately the stability of the system.

This thesis is organized into three main parts. Chapter 2 provides relevant background information and puts it into the context of this thesis. This section covers theoretical and experimental aspects of contact and adhesion modeling. Background on the gecko lizard, specifically its adhesive system, and previous work on synthetic gecko-inspired adhesives is also covered. The concept of directional adhesion is introduced and its usefulness for climbing is discussed. Chapter 3 presents the experimental investigation of a new synthetic adhesive that captures the directional properties of the gecko adhesion system. The new synthetic adhesive is briefly described along with details of an experimental setup and experimental procedures designed to test directional adhesives. Experimental results for the synthetic adhesive are given and its ability to duplicate some of the aspects of the gecko adhesion system is discussed. Finally, Chapter 4 formulates a theoretical study of the static equilibrium of multilegged climbers. Simplified two- and three-dimensional representations of robots or animals on inclined planes are described. A mathematical analysis is given that uses the internal forces of the system to maximize stability. The analysis reveals important considerations when using directional adhesion and explains some aspects of the gecko's climbing behavior.

1.3 Contributions

This thesis builds upon and adds to the general body of knowledge surrounding climbing, focusing on modeling adhesive contacts and on how the nature of the contact greatly influences climbing performance. Specifically, this thesis contributes the following:

- *Provides an experimental framework for studying and characterizing directional adhesives.* Details are given of an experimental setup and experimental procedures used for testing directional adhesives. Important considerations that

arise when testing an adhesive in more than just the normal axis are discussed.

- *Explores the detailed properties of a new synthetic directional adhesive that captures some of the gecko's adhesion properties.* Design and manufacturing process of synthetic gecko-inspired adhesive patches is briefly described. Experimental results are given that explore the relationship between common adhesive metrics and various experimental parameters. Compact limit surface description of the synthetic adhesive is presented and discussed.

- *Presents a theoretical analysis that predicts useful force-distribution strategies for climbing with directional adhesion.* Two- and three-dimensional models of multi-legged climbers are described. An analytical method is given that optimizes contact forces at different limbs using the internal force space in order to maximize stability. Results from the analysis are used to compare different contact models and to gain insight into the climbing behavior of geckos.

Chapter 2

Background Literature

The work presented here involves theoretical and experimental aspects of contact modeling with a specific focus on modeling adhesion for the purpose of studying and understanding climbing vertical surfaces. Contact modeling describes the interaction between two objects in physical contact with one another. Research topics in this area have included surface roughness [89, 90], area of real contact [49, 61], friction [29, 88], adhesion [61, 64], and fracture mechanics [80, 102], among others. Understanding the contact between two objects is crucial for many modern aspects of life ranging from Scotch Tape™ to car tires. The following sections will summarize previous research on contact modeling in general and adhesion modeling in particular.

When studying climbing, it is useful to look to Nature for insight and inspiration. The gecko lizard is arguably Nature's best climber, able to locomote on vertical and even overhanging surfaces of almost any material [8]. This noteworthy climbing ability has been well-known for many centuries, but recently, the gecko has become a source of inspiration for designing artificial adhesive structures due to its remarkable adhesion system [40]. Sections 2.3 and 2.4 will focus on the gecko lizard's adhesion system and experimental work being done to synthesize this system. Recent discoveries on the directional nature of the gecko's adhesion system will be examined along with a discussion of why directional adhesion is beneficial for climbing vertical surfaces.

2.1   Contact Modeling

In many ancient civilizations, the study of contact began with the study of friction. Potters' wheels and grinding stones required some kind of bearing support and friction was of great important in the transportation of heavy objects, especially when using only human- or animal-generated power. Indeed, there are examples in both the Egyptian and Roman civilizations of the use of lubrication to reduce friction in wheel axles and transportation sleds [19]. The formal beginning of the study of contact between two objects began with Leonardo da Vinci (1452-1519); however, he is generally not given credit because his notebooks were not published until many centuries later. Nevertheless, he first introduced the concept of a coefficient of friction, the ratio of the frictional force to the normal force between two objects.

In 1699 some of the principles governing friction were first published by Guillaume Amontons [3]. The French physicist observed certain rules by studying the dry friction behavior between two flat surfaces in contact. He found that the friction force resisting sliding is directly proportional to the normal load between the two objects (Rule #1). He also found that the amount of friction force is independent of the apparent area of the contact (Rule #2). In 1785, Charles-Augustin Coulomb verified Amontons' observations and added more to the understanding of friction [29]. Coulomb introduced a third rule to the friction laws, namely that the friction force is independent of the sliding velocity once motion has started. He also introduced the idea of different static and kinetic coefficients of friction.

2.1.1   Hertz Contact Theory

The first published study looking strictly at the contact between two objects, ignoring friction, did not come until 1882 from Heinrich Hertz. While working on optical interference patterns between two glass lenses, Hertz developed a theory that describes how two spherical surfaces deform when loaded against each other [58]. Hertz made the following assumptions to work out this theory: 1) surfaces are continuous, smooth and non-conforming, 2) the strains are small, 3) each solid is an elastic half-space in the vicinity of the contact region, and 4) the contacting surfaces are frictionless. An
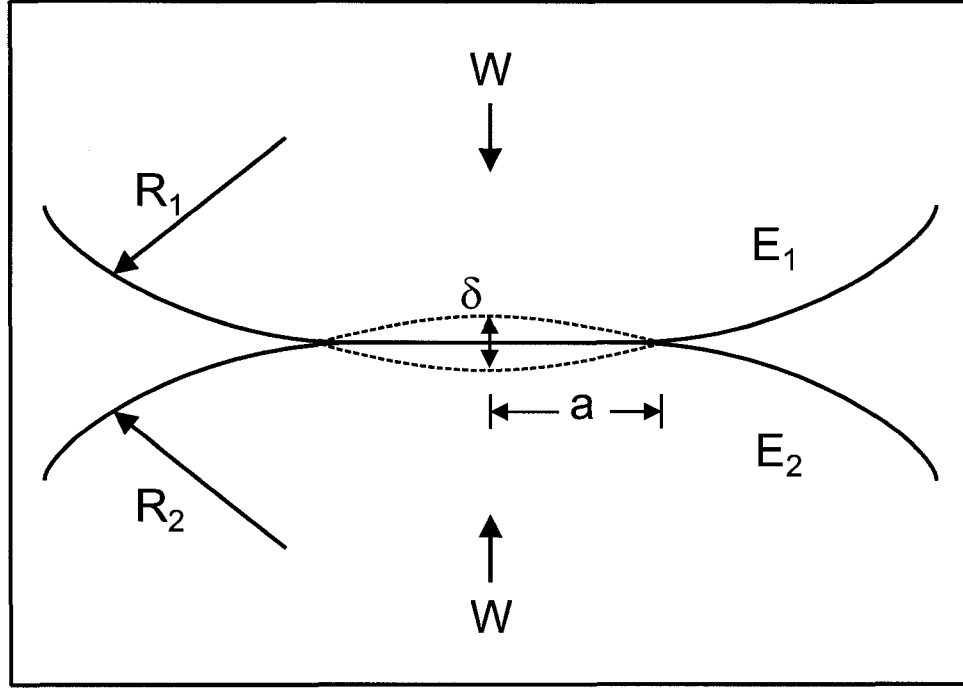
Figure 2.1: Schematic representation of Hertzian contact. Deformation of two spheres under an applied load.

elastic half-space is simply a semi-infinite elastic solid bounded by a plane surface [58], i.e. shape of the object, supporting method, and strains far away from the contact area are negligible.

Given these assumptions, Hertz was able to calculate the size of the contact area and the pressure distribution over the contact area under a given applied load [49]. For two spheres in contact, the contact area is a circle and its radius, a, is given by

$$a = \left(\frac{3WR}{4E^*}\right)^{\frac{1}{3}}, \tag{2.1}$$

where W is the applied normal load. The equivalent radius, R, is given by

$$\frac{1}{R} = \frac{1}{R_1} + \frac{1}{R_2}, \tag{2.2}$$

where R_1 and R_2 are the radii of the two spheres. The equivalent Modulus of Elasticity is given by

$$\frac{1}{E^*} = \frac{1 - \nu_1{}^2}{E_1} + \frac{1 - \nu_2{}^2}{E_2}, \tag{2.3}$$

where ν_1 and ν_2 are the Poisson's ratios and E_1 and E_2 are the Young's Moduli of the two spheres. The pressure distribution over the contact area varies with the radius as

$$p\left(r\right) = p_0\sqrt{1 - \left(\frac{r}{a}\right)^2}, \tag{2.4}$$

where p_0 is the maximum contact pressure given by

$$p_0 = \frac{3W}{2\pi a^2}. \tag{2.5}$$

Due to the applied load, the two spheres undergo a displacement, δ. The contact radius given in Equation 2.1 goes to zero and the objects separate as the applied load, W, goes to zero. A schematic representation of the contact between two spheres is shown in Figure 2.1.

2.1.2 Coulomb Friction

Hertzian contact theory provides a description of a contact that relates applied loads to the deformation of the objects involved. While such analyses and descriptions are essential for understanding contact phenomena, the work presented here is more concerned with descriptions of the forces that can be transmitted and withstood by the contact without failure. Failure of the contact occurs when either the objects slide relative to each other or physically separate from each other. The friction laws discovered by Amontons and Coulomb, generally referred to as "Coulomb friction", are an example of such a description of the forces involved in the contact between two dry solids. The Coulomb friction model is an empirical model based only on observations and not necessarily on any mathematical analysis. Nonetheless, it continues to prove useful at describing dry friction between two objects. Coulomb friction can
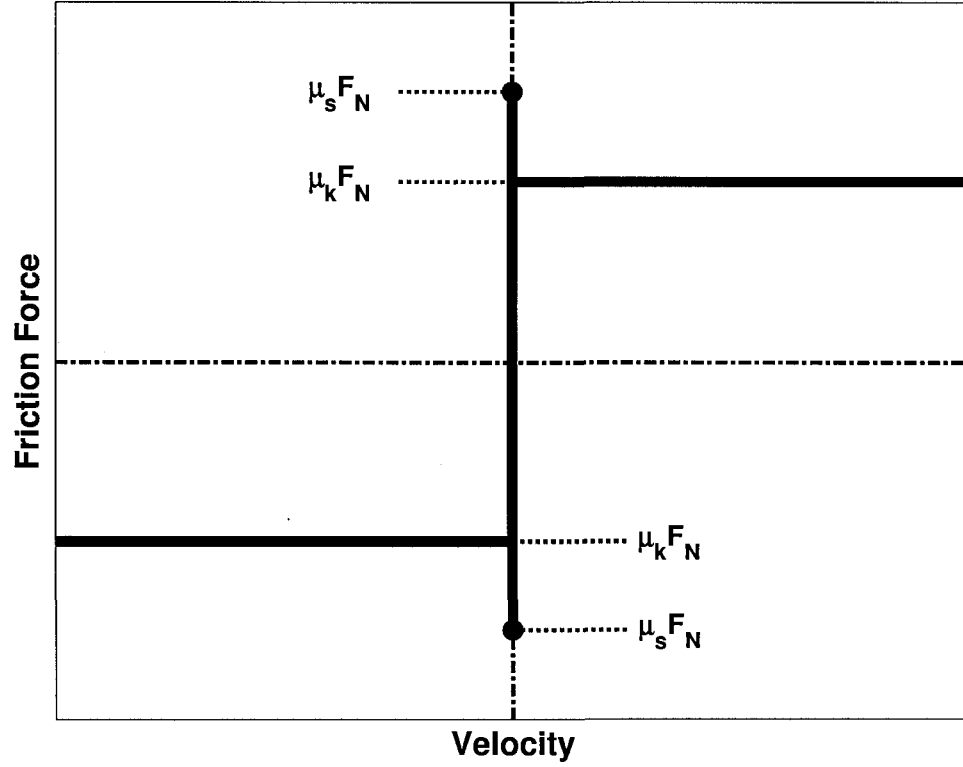
Figure 2.2: Relationship between Coulomb friction force and relative velocity of the two contacting objects. At zero velocity, the friction force can take any value to resist motion up to the static friction limit (dependent on the normal force). During sliding, the friction force is a constant equal to the kinetic friction limit (dependent on the normal force). μ_s and μ_k are the static and kinetic coefficients of friction, respectively, and F_N is the normal force at the contact.

be captured mathematically by the following set of equations:

$$\begin{aligned} |F_T| &\leq \mu_s F_N \\ F_T &= -\operatorname{sgn}(v)\mu_k F_N \end{aligned} \quad \left\{ \begin{array}{l} v = 0 \\ v \neq 0 \end{array} \right. , \tag{2.6}$$

where F_T is the tangential force, F_N is the normal force (taken positive when compressive), μ_s is the static coefficient of friction, μ_k is the kinetic coefficient of friction, and v is the relative velocity between the two objects. Graphically, Figure 2.2 shows

the dependence of the friction force on the relative velocity of the objects and coefficients of friction. Generally, the static coefficient of friction is equal to or greater than the kinetic coefficient of friction.

The above is a rather simplistic view of friction, and real friction is a much more complicated phenomenon than what is shown in Figure 2.2. Theoretical treatments of friction consider both the effects due to mechanical interlocking at the surface and intermolecular forces present at the atomic level [121]. Both experimental and theoretical research has discovered various friction effects not captured in the classical Coulomb friction model [5, 6]. Fluid boundary layers can add velocity-dependent damping terms to the friction force [94], and the Stribeck effect can produce stick-slip behavior at small velocities due to a negative viscous damping term [110], in addition to many other dynamic effects. Even the static friction forces can be affected by the dwell time of a contact [91].

Nevertheless, the static friction description in Equation 2.6 is a useful model for the present discussion. This work is primarily concerned with the static or quasi-static, and not the dynamic, behavior of contacts. When climbing, statically unstable contacts can produce slipping and falling, thus causing catastrophic failure. Adhesive contacts, which are discussed in the next section, can fail even under relatively small displacements. Therefore, velocity effects at a contact interface are not primarily important for climbing, and the scope of this work is limited to studying only the static or quasi-static nature of contacts.

Returning in more detail to the Coulomb friction model, only the case of static equilibrium needs now to be considered, i.e. no relative sliding between the objects. In this situation, the forces at the contact are not explicitly defined. Instead, there is a limit on the magnitude of the normal and tangential components of the contact force given by the inequality constraint in Equation 2.6. In order to prevent sliding between the objects, the inequality must be satisfied. Figure 2.3 shows this graphically, with the classic "Coulomb friction cone." The solid lines represent the limits of the inequality constraint in Equation 2.6 and the shaded region represents all combinations of forces that satisfy the constraint. In other words, Figure 2.3 represents the "limit curve" (solid lines) and the region of stability (shaded area) for the contact
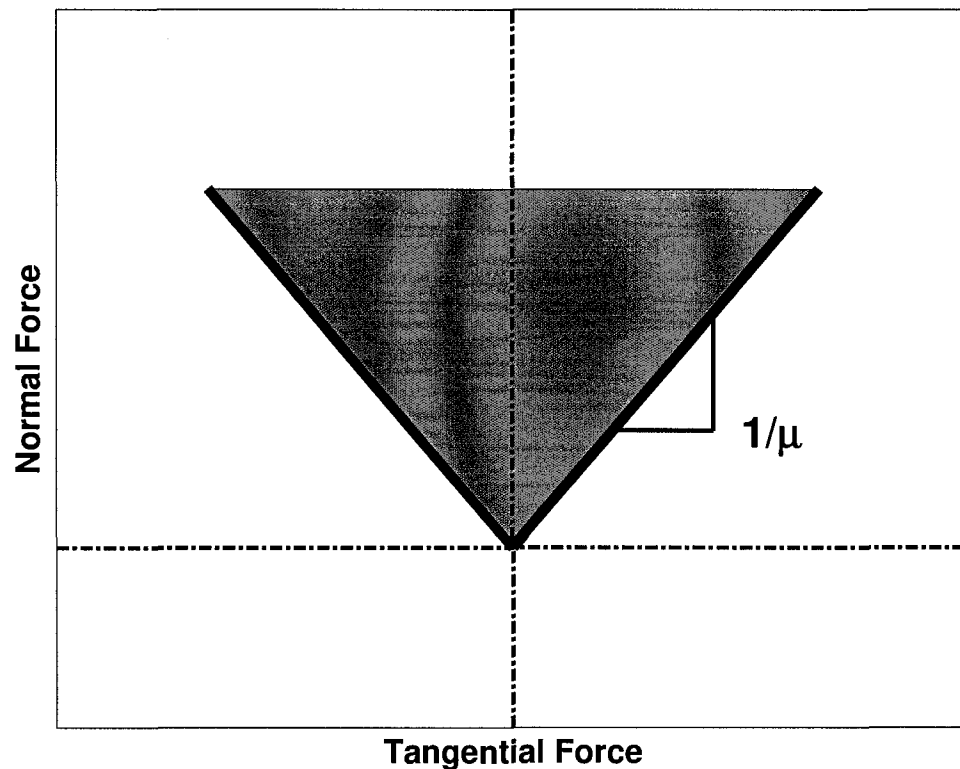
Figure 2.3: Coulomb friction cone. Lines show the force limits on the tangential and normal forces for static equilibrium to be maintained. Combinations of tangential and normal forces that lie within the shaded region will not cause sliding at the contact. This plot gives the 2-dimensional limit curve of the contact for static equilibrium.

[44, 45]. Of course, contacts will generally involve forces in three dimensions and the limit curve becomes a "limit surface" in three-dimensional force space.

The limit surface is a useful tool for the design, analysis, and control of robotic systems that interact with the environment. It provides a concise description of what forces can be sustained without slipping at the points that a robot interacts with its environment. Much research on walking robots [54, 72, 75, 116], dexterous manipulation [22, 26, 65, 78], and climbing robots [24, 25, 53, 79] has made use of the contact limit surface implicitly or indirectly. In addition, [62] explicitly uses the limit surface to study manipulation with compliant fingertips.

While essential for understanding contact, the models covered so far fail to capture

at least one important aspect of contact — adhesion. The Hertz contact theory predicts that as the applied load falls to zero the contact area will also go to zero and eventually the objects simply separate. Coulomb friction predicts a similar behavior. The region of stability defined by the limit curve shown in Figure 2.3 is strictly in the positive half-plane of the Normal Force axis. Hence, contacts are only stable in the presence of compressive forces. The ability of contacts to withstand tensile forces at the contact interface is the subject of the next section.

2.2 Adhesion Modeling

2.2.1 Early Work

Early studies of friction attributed the forces seen at the contact to the mechanical interlocking of small asperities. It was not until 1734 that adhesion from molecular forces was also introduced as a component in the friction process by Desaguliers [36]. This combined view of friction and adhesion caused by both mechanical interlocking and molecular forces experienced relatively little attention until it was revived by Prandtl and Tomlinson in 1928 and 1929, respectively, and further studied by Derjaguin in 1934 [36]. The prevailing modern understanding is that friction and adhesion are fundamentally related, although the exact details of said relationship may be complicated and sometimes only experimentally determined [121]. The nature of adhesion has been studied extensively, and while general relationships between friction and adhesion do not always exist, simple macroscopic models have been proposed and certain specific configurations have been analyzed in detail.

Derjaguin [34, 36] was the first to perform a quantitative study of combined adhesion and friction, using a statistical analysis of intermolecular forces and crystal structure, to arrive at the following simple equation for the coefficient of friction,

$$\mu = \frac{F}{a\,(p + p_0)},\tag{2.7}$$

where μ is the coefficient of friction, F is the friction force, a is the contact area, p is the mean pressure caused by externally applied loads, and p_0 is the mean pressure caused
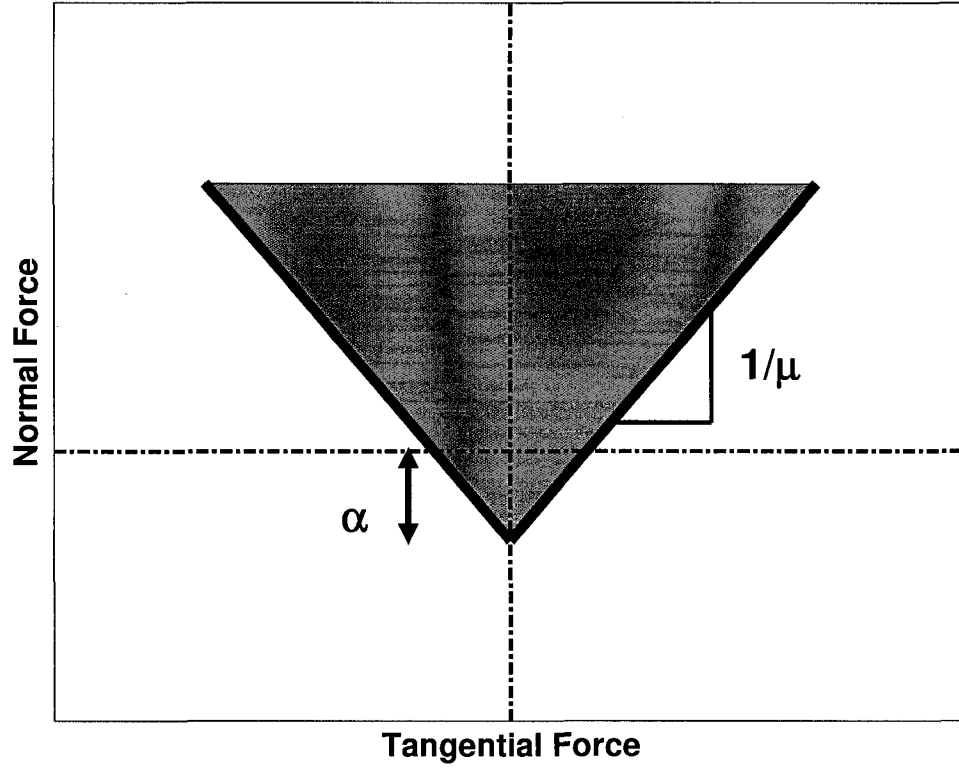
Figure 2.4: Embedded Coulomb friction cone. A modified friction cone that has taken into account adhesive forces acting at the contact via an offset in the normal axis. Parts of the cone now lie beneath the tangential axis, representing the adhesive loads that the contact can sustain without failure.

by molecular adhesive forces [36]. Equation 2.7 can be simplified and re-written as

$$F_T = \mu \left(F_N + \alpha \right), \tag{2.8}$$

to have the same form as the Coulomb friction law, where F_T is the friction force (tangential), F_N is the external force (normal), and α is the net force arising from adhesion.

Equation 2.8 has since appeared in similar forms in [113, 121] and is perhaps the simplest modification to the classic Coulomb friction equation in order to incorporate adhesion. As was done earlier, Equation 2.8 can be viewed graphically as a relationship between the normal and tangential forces at a contact. Figure 2.4, here termed

the "embedded-cone model", is very similar to Figure 2.3 of the Coulomb friction cone. Here, however, the friction cone has been shifted downward such that the cone now extends into the negative normal axis, representing adhesion. Again, this figure shows a limit surface, and in this case, there are areas inside the cone that are stable in the presence of negative normal loads, i.e. adhesive forces.

2.2.2   Johnson-Kendall-Roberts Model

Further work continued in attempts to better understand the nature of adhesion [23] leading up to the publication of the well-known JKR theory of adhesion by Johnson, Kendall, and Roberts [61]. This analysis extended the Hertz contact theory and looked at the contact between two spherical objects undergoing elastic deformations in the presence of adhesive forces. Johnson et al. looked at adhesion as the force associated with a change in the surface energy between the two solids. In this sense, the adhesive force is caused by the work required to create two new surfaces when the objects are pulled apart. This new theory shows that in the absence of an externally applied load there is still a finite contact area. The energy released from formation of the contact is balanced by the elastic strain energy stored in the deformation of the two solids. According to JKR theory, under no external load the contact radius is

$$a = \left(\frac{9\gamma\pi R^2}{2E^*} \right)^{1/3}, \tag{2.9}$$

where γ is the surface energy of the contacting solids and R and E^* are the equivalent radius and stiffness given by Hertz theory. The surface energy refers to the free energy of molecules at the boundary of an object that can go into forming new bonds with molecules on another object. Typical surface energies for solids range from hundreds to thousands of mJ/m^2 [19]. The JKR theory also predicts that a finite pulloff force is necessary to separate the objects and is given by

$$P = \frac{3}{2}\gamma\pi R. \tag{2.10}$$

JKR theory was better able to predict the contact area and separation forces in

experiments between soft rubber spheres than Hertz theory [61].

Using the same surface energy approach, Derjaguin et al. [35] reached slightly different results. They found that the pulloff force was given by

$$P = 2\gamma\pi R. \tag{2.11}$$

This discrepancy arose because of differing assumptions about how the solids would deform outside of the contact region. It was not until 1977 when Tabor showed that both of these theories were correct and were simply at opposite ends of the spectrum of a non-dimensional parameter [112]. That parameter is defined as

$$\lambda = \left(\frac{R\gamma^2}{E^{*2}z_0^2} \right)^{1/3}, \tag{2.12}$$

where z_0 is the equilibrium spacing of the Lennard-Jones potential [76]. When λ is less then ≈ 0.1 the contacting spheres are relatively small and stiff and the Derjaguin-Muller-Toporov (DMT) theory is valid but when λ is greater than ≈ 5 the contacting spheres are relatively large and soft and the JKR theory is valid. At values in between these two, the actual behavior is somewhere in between these two theories.

Using the JKR theory of adhesion, a more accurate contact model than the one shown in Figure 2.4 can be constructed. The area of contact as a function of the applied load is given by

$$a^3 = \frac{3R}{4E^*} \left(P + 3\gamma\pi R + \sqrt{6\gamma\pi RP + (3\gamma\pi R)^2} \right) \tag{2.13}$$

As a first approximation, the tangential friction limit can be considered to be independent of the adhesion limit given in Equation 2.10. The area of the contact given by JKR theory, which is a function of the applied load, and the shear strength of the interface then completely define the friction limit. Under this assumption, the tangential friction limit is given by

$$F_T = \sigma_T \pi a^2. \tag{2.14}$$
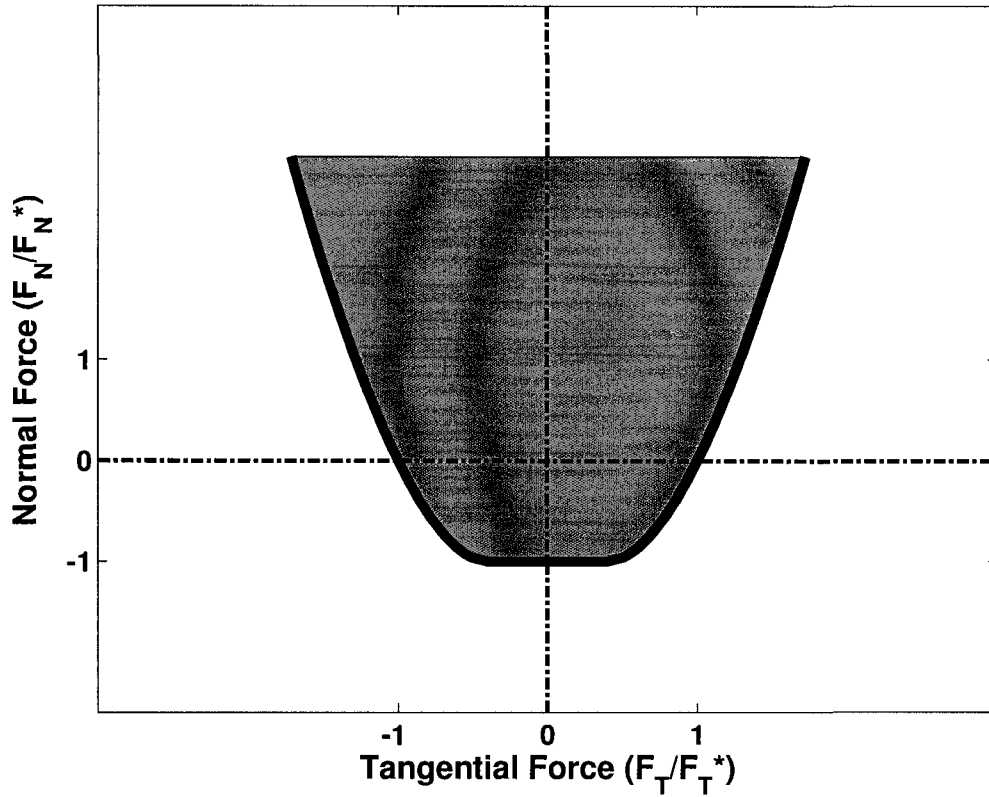
Figure 2.5: Illustration of the JKR model limit surface. Relationship between the applied normal load in JKR theory and the shear traction limit under the assumption that tangential loads are independent of adhesive loads. Forces have been normalized to show general characteristic behavior (see Appendix A). Tangential forces are shown normalized to the maximum tangential force at zero normal load and normal forces are shown normalized to the maximum adhesion force at zero tangential load.

Using Equations 2.10, 2.13, and 2.14 the force limits on the normal force and tangential force can be calculated (see Appendix A). The normalized forces given by this analysis are shown graphically in Figure 2.5. The behavior of the JKR limit surface is similar to that of the simple embedded-cone model. Both are symmetric about the vertical axis, and in both cases, increasing the amount of tangential force applied at the contact decreases the amount of adhesion that can be sustained. However, the JKR model, a more accurate model, is not just a simple linear relationship but has a non-linear, bowl shape. Also note that the bottom portion of the limit surface shown

in Figure 2.5 is flat. This is a result of the initial assumption that the shear limit is independent of the adhesion limit and is solely dependent on the shear strength of the contact interface and the contact area.

2.2.3 Savkoor-Briggs and Other Advances

Further work in the field of adhesion concentrated on understanding the relationship between normal and tangential loads. The first such experiments were conducted by Savkoor and Briggs [102] on rubber hemispheres in contact with a flat glass substrate, although the theory developed can be generalized to spheres of arbitrary radii in contact. These studies found that increasing the tangential force at the contact reduced the contact area, and thus that the friction and adhesion forces are not independent. The authors were able to use an energy balance method to determine a critical tangential force where the contact would peel given an applied normal load. That relationship is given as

$$F_T = \frac{4}{\sqrt{K\lambda}} \left(2\gamma\pi R F_N + 3\gamma^2\pi^2 R^2\right)^{\frac{1}{2}}, \tag{2.15}$$

where K, γ, and R are the same effective stiffness, surface energy, and effective radius, respectively, as in the JKR model. Here, λ is the effective shear modulus and is given by

$$\lambda = \left(\frac{2-\nu_1}{G_1} + \frac{2-\nu_2}{G_2}\right), \tag{2.16}$$

where G_1 and G_2 are the respective shear moduli of the two solids. The same adhesive limit derived in the JKR theory also applies here and when the applied normal load is at this pulloff limit, the critical tangential force becomes zero. As before, the normalized relationship between the tangential and normal forces is shown graphically in Figure 2.6.

There has been other work in the area of a combined understanding of the tangential and normal forces at the contact between two spherical (or spherical and flat) elastic solids in contact under adhesive forces, in particular [28, 59, 60]. While there
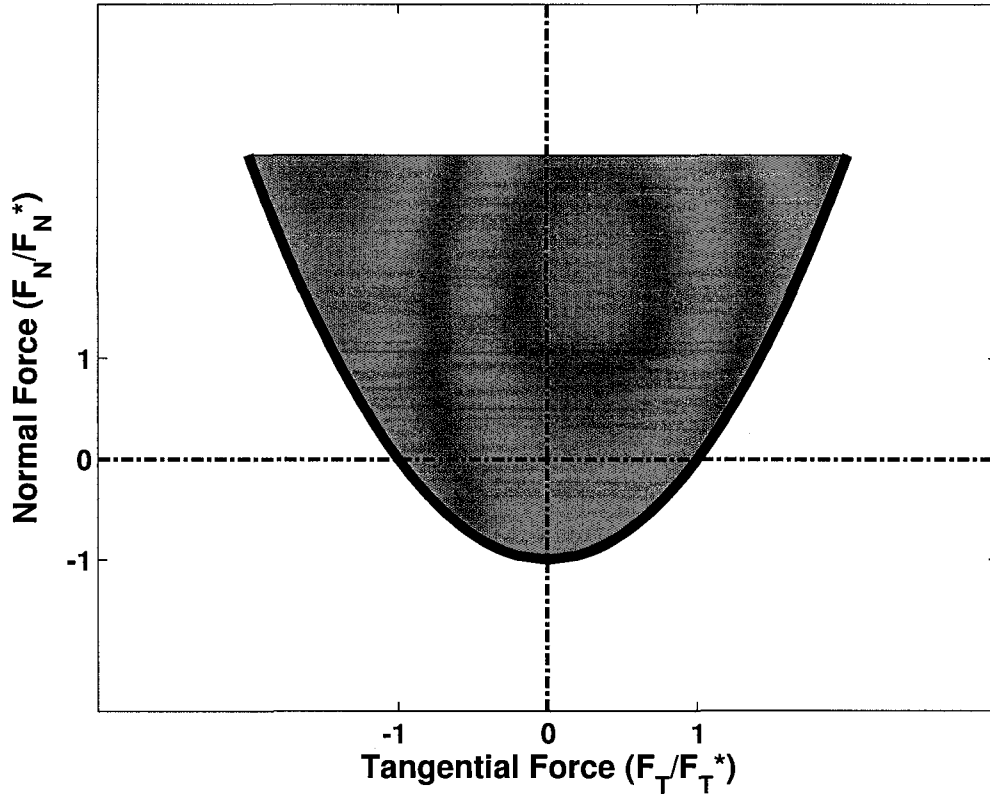
Figure 2.6: Illustration of the Savkoor-Briggs model limit surface. Relationship between the critical tangential force and the applied normal force given by the Savkoor-Briggs theory [102]. Forces have been normalized to show general characteristic behavior. Tangential forces are shown normalized to the maximum tangential force at zero normal load and normal forces are shown normalized to the maximum adhesion force at zero tangential load.

are some differences in the treatments and results of these different works, they all conclude that increasing tangential forces decrease the area of contact and thereby decrease the maximum pulloff force (or, applying more adhesive load at the contact decreases the amount of tangential force that can be sustained). As will become clear later, the exact details of each of these different models is not of paramount importance to this work, rather, it is merely important to understand the general behavior of this class of adhesive models. The limit surfaces that can be derived from these different theories will all exhibit the same general behavior, namely that they
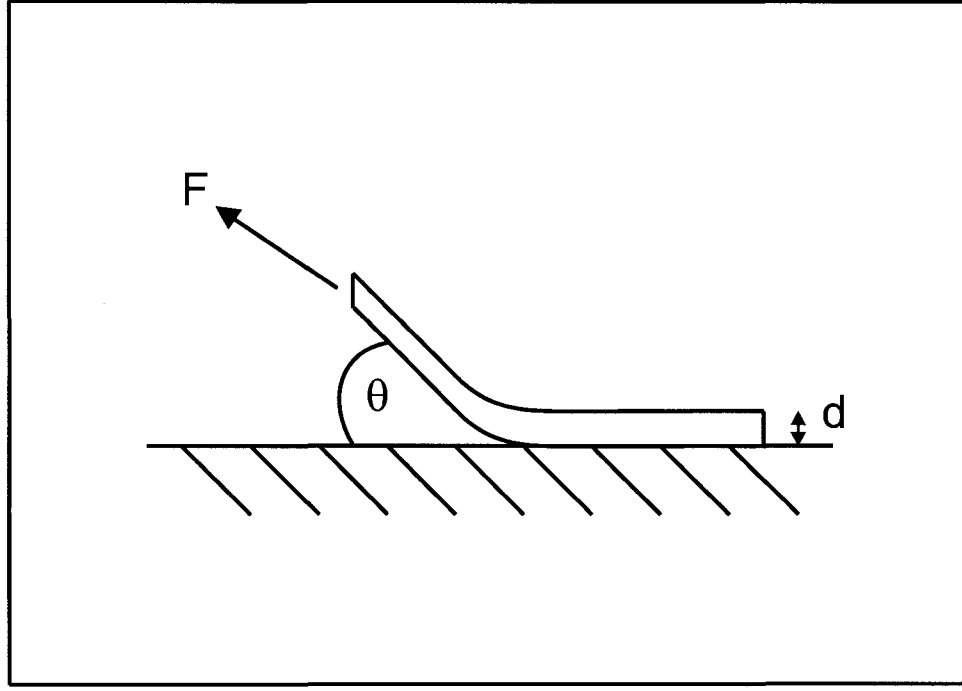
Figure 2.7: Kendall Peel Model Schematic. Diagram shows a thin elastic film peeling from a rigid flat substrate. The peeling force, F, will be dependent on the peeling angle, θ, and the peel rate.

are bowl-shaped, symmetric about the normal axis, and have a pulloff force somewhere along the negative normal axis (adhesive force). Either the JKR model shown in Figure 2.5 or the SavkoorBriggs model shown in Figure 2.6 will suffice for future discussions of this class of models.

2.2.4 Kendall Peel Model

Before ending this discussion on adhesion models it is important to mention one more well-known adhesive model. The Kendall Peel model [63] describes the peeling behavior of a thin elastic film from a smooth flat substrate. Figure 2.7 shows a diagram of the process being analyzed. As the tape is peeled, work goes into breaking the adhesive bonds at the interface to create two new surfaces and into potential energy

stored in the elastic strain of the thin film. Using an energy-balance method, Kendall found that the pulloff force is dependent on the pulloff angle and is given by

$$F = bdE \left(\cos\theta - 1 + \sqrt{\cos\theta^2 - 2\cos\theta + 1 + 2\frac{R}{dE}} \right), \qquad (2.17)$$

where b is the width of the film, d is the thickness of the film, E is the Modulus of Elasticity of the film, θ is the pulloff angle, and R is the adhesion energy per unit area of the interface. The width of the film allows the pulling force to be linearly scaled while the adhesion energy, stiffness, and thickness of the film will change the relationship between the peeling force and peeling angle. It should also be noted that, in general, the adhesion energy (R) is rate dependent.

Equation 2.17 can be decoupled into normal and tangential force components and normalized to produce a characteristic limit surface shape, shown in Figure 2.8, which exhibits a very different behavior than any of the models previously discussed. The most clear distinction is that this model is not symmetric about the normal axis. When pulling the film at shallow angles (positive tangential axis in the figure), the pulling force can be quite high. As the pulling angle is increased, the pulloff force decreases, reaching a minimum when the film is peeled back on itself. The model is not defined for positive values of normal force since this would account to peeling the film "into itself". Maximum adhesion is attained when pulling at an angle between 0° and 90°, coupled with a tangential force as well. This differs from the previous models where tangential forces decrease the amount of adhesion that can be sustained. This behavior also gives the Kendall model "directionality."

2.2.5 Summary

The previous sections have covered the origins and history of contact and adhesion modeling. In particular, the main theoretical adhesive models from the literature have been summarized and some of their more important aspects have been discussed. The concept of a limit surface was introduced and how it captures the forces that can be sustained at a contact interface without failure. The embedded-cone, JKR, DMT, and SavkoorBriggs models all provide a similar description of the interaction forces
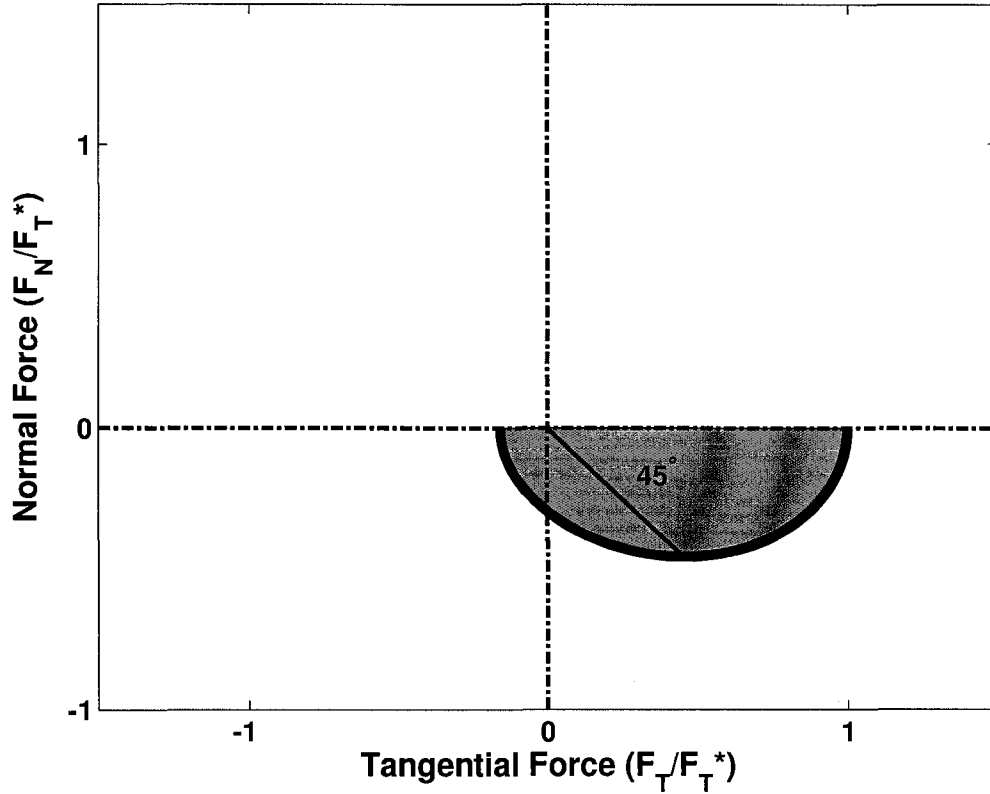
Figure 2.8: Illustration of the Kendall Peel model limit surface. Pulloff forces in the normal and tangential directions predicted by the Kendall thin-film peeling model [63]. Forces have been normalized and maximum adhesion has been set to coincide with a peeling angle of 45° in order to show general characteristic behavior. Both tangential and normal forces are shown normalized to the maximum tangential force at a peeling angle of 0°.

at a contact with adhesion. In this class of models there exists a finite pulloff force in the normal direction representing the adhesion between the two objects in contact. As tangential loads are applied to the interface, the amount of adhesion that can be sustained decreases. The Kendall Peel model differs from these others by exhibiting an asymmetry. Maximum adhesion is achieved when also pulling to the side.

This work is concerned with studying and understanding climbing and these models and concepts provide a framework for that end. The next sections will deal with the gecko lizard adhesion system and ongoing research into duplicating that adhesive
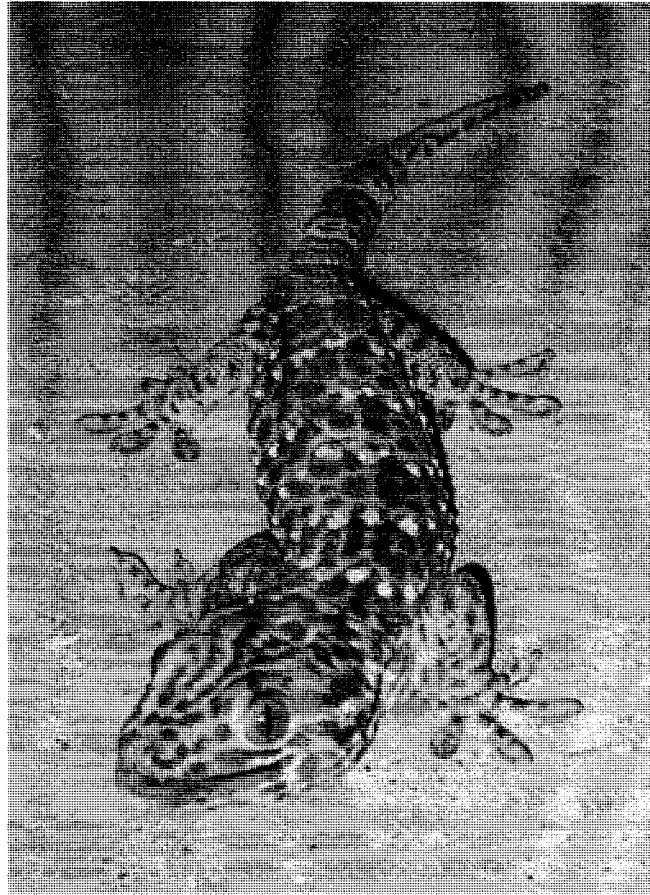
Figure 2.9: Example of a typical gecko lizard [77].

system.

2.3   The Gecko Adhesive System

Nature has evolved many different mechanisms in vertebrates for climbing. These are mostly for the purposes of arboreal life although some of these mechanisms work remarkably well on a variety of surfaces including rock faces and even smooth glass. While simple friction will allow animals to climb inclined flat planes or vertical circular poles that can be gripped, without an infinite coefficient of friction it cannot explain how some vertebrates are able to climb flat vertical surfaces.   To achieve robust
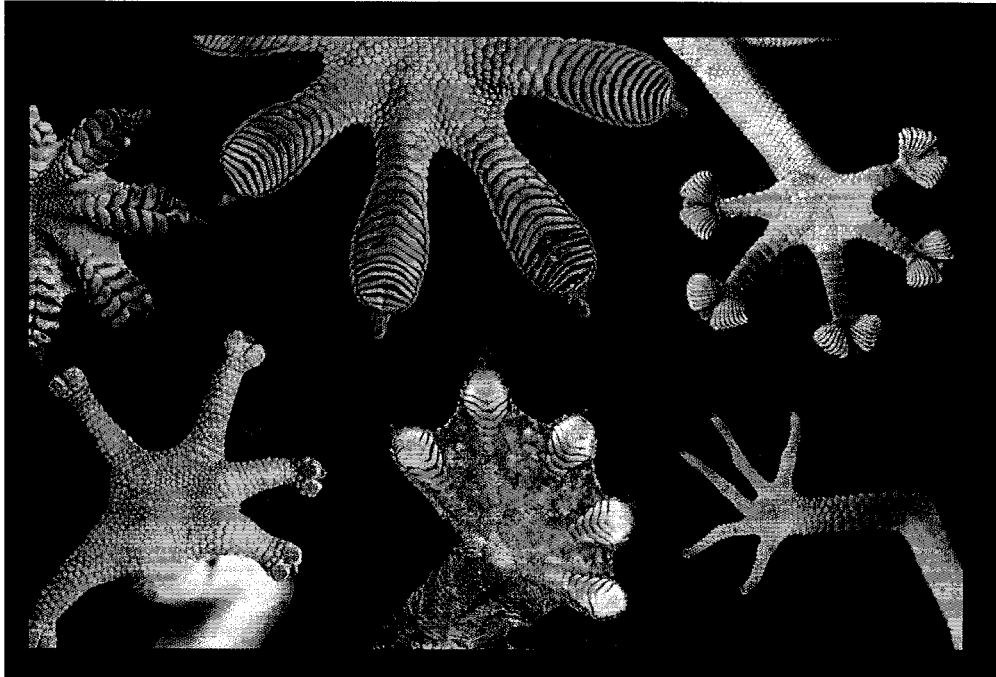
Figure 2.10: Some of the different types of gecko feet [109].

climbing, vertebrates use claws, capillary forces, dry adhesion, and suction to climb either by interlocking the surface of the animal with that of the support, developing adhesive bonds between the two surfaces, or a combination of the two [27]. These different mechanisms have evolved separately in many different species to produce agile climbers, but perhaps the most exceptional is the gecko lizard.

Geckos (Figure 2.9) are relatively small, agile lizards that are able to locomote on vertical and even overhanging surfaces. They range in size from only about 3cm long and 10g to 40cm long and 400g and their average lifespan is between 10 and 20 years [48]. Gecko skin is comprised of scales made of dead keratin cells and geckos periodically shed their skin at regular intervals. Gecko skin is generally gland-less, except in a few species where the gecko is able to secrete a foul-smelling liquid to ward off predators [48]. The most remarkable feature of the gecko is its foot structure, which varies significantly among the different species, although there are common characteristics that bestow the incredible climbing ability. Figure 2.10 shows some of

the different shapes and styles of gecko feet.

The impressive climbing ability of the gecko was noted as far back as during the time of the Greeks when Aristotle stated that geckos "can run up and down a tree in any way, even with the head downwards" [4]. This extraordinary climbing behavior is derived from the gecko's dry adhesion system [17, 27]. Dry adhesion is the name given to an adhesive system that does not rely on any type of capillary forces from fluid films and is able to resist contamination by dirt. In the case of the gecko, the adhesion arises from intermolecular forces commonly known as van der Waals or London dispersion forces.

Van der Waals forces are caused by the formation of instantaneous dipoles in two neighboring molecules that will then attract each other [64]. The magnitude of the van der Waals force between a flat circular punch geometry (i.e. flat end of a cylinder) and a flat substrate is given by

$$F_{vdw} = \frac{AR^2}{12D^3} \tag{2.18}$$

where A is the Hamaker constant, R is the radius of the contact area, and D is the gap distance between the objects (typically 0.2nm for solids in contact) [56]. The Hamaker constant is a function of the molecules in contact but is typically on the order of 10^{-19}J [8, 56]. Van der Waals forces are extremely sensitive to the distance between the two objects and become negligible at distances of more than about 10nm [27, 64].

The ability of the gecko to climb by using van der Waals forces is a direct result of its microstructured feet. While gecko feet come in different shapes and sizes (Figure 2.10) they all share some common features, namely lamellae, setae, and spatulae. Each toe is covered in a dense array of setae arranged in rows called lamellae that run transversely across the toe and can be raised and lowered by a system of tendons [27]. The setae are small vertically oriented stalks approximately 100μm long and 5μm in diameter and have a density of about $5,000 - 15,000$setae/mm^2 [16, 96]. The tips of the setae branch into about 100 to 1,000 finer stalks called spatulae [95]. The spatulae terminate in a triangle-shaped, thin structure about 200nm wide [95, 96] resembling
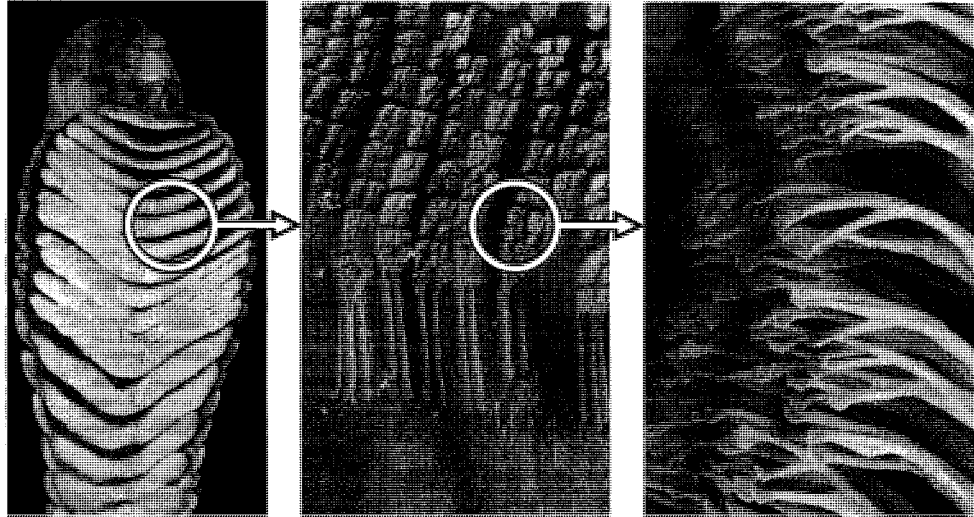
Figure 2.11: Gecko Foot Microstructures: Lamellae, Setae, and Spatulae. Photos show the different structures of the gecko toe pad. Setae are organized into rows called lamellae and branch at their tips into spatular-shaped tips called spatulae. Images reproduced with permission [9].

a spatula. Figure 2.11 shows the hierarchical microstructures just described.

While the superb climbing ability of the gecko has been well-noted for some time, it is only in the last ten years that advances in science have allowed quantitative studies of the gecko adhesion system. Indeed, only recently was experimental evidence published to support that claim that the gecko adhesion system is based on van der Waals forces [17]. Previous studies had concluded that the primary mechanism for gecko adhesion was mechanical interlocking [33] or capillary forces acting at the contact interface [50]. In [17], the adhesion force of single gecko setae were tested on both a hydrophobic and hydrophilic, molecularly smooth, microelectro-mechanical force sensor. Gecko setae are themselves highly hydrophobic with a water contact angle of about 160° [17]. If capillary forces were the dominant mechanism, it should be the case that the hydrophobicity of the substrate should determine the amount of adhesion. Setae adhered equally well to both the hydrophobic and hydrophilic substrates, providing direct evidence that van der Waals forces and not capillary forces must be the dominant mechanism of adhesion, mechanical interlocking being

ruled out due to the smoothness of the substrates. However, while this currently seems to be the prevailing consensus, there are is still some debate on this issue [111].

Geckos are able to generate significant *macroscopic* adhesion via van der Waals forces because of the hierarchical structures on their feet and toes. For van der Waals forces to become significant, molecules must be brought into extremely close proximity to one another, on the order of a few nanometers [64]. When two apparently flat objects contact each other, they do not stick because, upon closer inspection, they are only contacting at a few points along their surfaces. At the molecular level, visually flat surfaces are actually quite rough, appearing not unlike a mountain range with peaks and valleys throughout.

In order for van der Waals forces to become significant at the macroscopic level ($> 1 \text{cm}^2$), a large real area of contact must be generated. Usually, in order to achieve this one of the materials must be quite soft so that it can conform to the other surface and create a large real contact area [37]. This is precisely the way that Pressure Sensitive Adhesives (PSAs) such as Scotch Tape$^{\text{TM}}$ work. This softness requirement has been well studied by C.A. Dahlquist [32]. This work led to the "Dahlquist Tack Criterion", which states that a material must have a stiffness less than about 100kPa in order to be "tacky". When a material is softer than this limit, it is able to "flow" and conform to the other surface and create a large real area of contact, and hence, is tacky.

The gecko's setae and spatulae structures are made from β-keratin, which is a very rigid material with a stiffness of approximately $1 - 2 \text{GPa}$ [8, 95]. This would normally prevent the gecko's feet from generating enough real contact area for van der Waals forces to become significant. However, the hierarchical nature of the microstructures reduces the stiffness of the bulk β-keratin to an effective stiffness of about 100kPa [15, 41]. Studies of how the hierarchical structure operates to reduce overall stiffness and how splitting of the contact area produces more robust adhesion have been done in [7, 120], but the end result is that it allows large numbers of the spatulae to make good contact with both smooth and rough surfaces, thus creating a large real contact area.

The gecko adhesive system also has other quite extraordinary characteristics in

addition to its primary adhesive capabilities. These properties have been described in [8] and are listed here: 1) Directionality, 2) High Coefficient of Adhesion (μ', the ratio of pulloff to preload force), 3) Low detachment force, 4) Material independence, 5) Self-cleaning, 6) Anti-self sticking, and 7) Non-sticky default state. Properties 4-7 have been well studied in the literature [12, 38, 47, 120], and have been the predominant focus in recent research aimed at creating synthetic, gecko-inspired adhesives. Some of these synthetic adhesives will be discussed in the next section. More detailed studies into properties 1-3 have only recently been published and will be the subject of Section 2.5.

2.4   Gecko-Inspired Synthetic Adhesives

Because the gecko adhesive system is so effective, it has been the focus of research aimed at creating better synthetic adhesives. Many researchers have been modeling the structures of the gecko toes to gain insights into their operating principles. Questions in this area have involved the scaling of the hierarchical system, the shape of the terminal contact points, and the subdivision of contact area via fibrillar structures [20, 39, 71, 108]. Other researchers have been developing techniques for manufacturing synthetic structures that resemble those of the gecko toe out of artificial materials including polyurethane, silicone, and carbon nanotubes [43, 69, 105, 122]. Common adhesion descriptors that are used to compare theoretical models to natural and synthetic adhesive systems include the Coefficient of Adhesion (μ'), the Work of Adhesion (W_{adh}), and the maximum pulloff force (or pressure). The Coefficient of Adhesion is the ratio of the maximum normal pulloff force (or pressure) measured during the separation process and the preload force (or pressure) applied to bring the adhesive into contact with the substrate initially [19]. The Work of Adhesion is the energy per unit area (J/m^2) dissipated during the formation and failure of the contact interface [31]. Finally, the maximum pulloff force is simply the maximum measured value of adhesion during the separation of the adhesive from the substrate.

2.4.1 Theoretical Considerations

The relationship between tip shape, stiffness, feature size, and hierarchical levels is complicated. All of these parameters can affect the amount of real contact area generated by a natural or synthetic adhesive and its robustness to contamination and surface roughness, which will all, in turn, affect the overall levels of adhesion. Even a simple subdivision of the contact area into short "pancake" posts of varying diameter and spacing has been shown to affect adhesion [30]. In this study, the adhesion of a smooth and flat polyurethane was compared to relatively simple structured versions of the same material. Different patches of circular posts 4μm in height and with varying diameters and edge-to-edge spacings between $50 - 500\mu$m were fabricated out of Polydimethylsiloxane (PDMS). The different pattern geometries were able to alter the adhesion from 20% to 400% of commonly accepted adhesion descriptors for the bulk material (unpatterned).

While [30] showed that simple pattern variations can affect adhesion, it did not explore how the size and shape of the tip features affect adhesion. Studying beetles, flies, spiders, and geckos, shows that there is a relationship between the size of the tip features and the body mass of the organism [7]. As body mass increases, the size of the tip features becomes smaller and the structures become more complex. Further studies in [39, 103, 108] explored the relationship among tip shape, size, and adhesion of these structures. In general, these studies show that as the feature size is reduced the tip shape and precision become less critical to the overall adhesion, but at larger scales the tip shape can have a dramatic affect on the adhesion. In particular, [39] has shown that adhesion only becomes shape-insensitive at length scales below about 100nm; however, it is still possible to achieve high adhesion at larger scales if the tip shape is optimal and very precise. Optimal tip shapes are those that prevent premature crack formation at the perimeter and evenly distribute the stress along the contact area.

Another important aspect of any natural or synthetic adhesive is the compliance of the system to rough surfaces. While many surfaces appear smooth at the macroscopic scale, at the molecular scale they may be very rough [18]. When these surfaces contact one another, only a fraction of the apparent contact area is in real contact

at the molecular level. Asperities caused by microscopic surface roughness and the elasticity of the materials creates a situation in which only the asperity tips are in close contact and the rest of the surfaces are separated by a gas or fluid. The elastic restoring forces caused by material deformation are in constant opposition to the attractive adhesion forces [90], thus preventing greater areas of intimate contact.

To create practical adhesives that attain large real contact areas, researchers, using examples in Nature, have employed the use of hierarchical fibrillar structures [20, 38, 55, 71]. Such structures are essentially arrays of individually compliant JKR spheres each intimately and independently contacting the surface [20]. An effective adhesion system needs to be compliant at all relevant length scales in order to attain intimate contact with the substrate over a large contact area. Multi-level hierarchical systems were shown to achieve better adhesion on rough surfaces with roughnesses at the same scales as the hierarchical structures [20, 71]. Analyses of single fibrils were also shown to enhance adhesion by stretching and absorbing energy before detaching, thereby increasing the overall work of adhesion [55]. The need for multiple levels of hierarchy with decreasing features sizes was shown in [38], which calculated an upper limit to the length of fibrils at which the fibrils will self-stick and clump, reducing the adhesion.

In general, hierarchical fibrillar structures reduce the stiffness of the bulk material to a lower effective stiffness. When this effective stiffness is lower than the Dahlquist Tack criterion [32] the structures become tacky even though the bulk material is not. While adhesion could be achieved by simply using a soft material, using a stiff bulk material has advantages. When the bulk material is above the tack limit, the adhesive can be self-cleaning because the bulk material is non-sticky by default. In contrast, when using an initially soft material such as a Pressure-Sensitive Adhesive (PSA) the adhesive will become contaminated after a few uses and lose its adhesive ability.
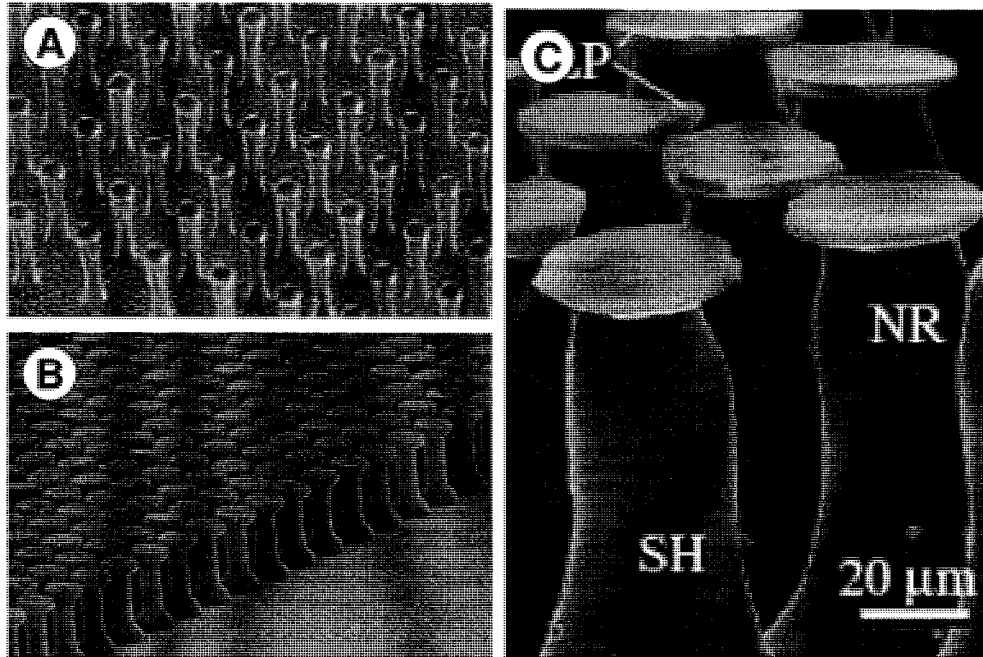
Figure 2.12: A - Polyimide fibrils 2μm long and 500nm in diameter [40]. B - Polyurethane stalks 20μm long [69]. C - Polyvinylsiloxane biomimetic mushroom-shaped fibrillar adhesive [43].

2.4.2 Experimental Examples

One of the first attempts at creating a gecko-inspired synthetic adhesive used electron-beam lithography and dry etching in oxygen plasma to create microstructured poly-imide patches (Figure 2.12)[40]. The patches (about $1cm^2$) had 500nm diameter and 2μm long hairs, spaced 1.6μm apart. When on a hard backing these adhesive patches exhibited a pulloff force of only .01N with a preload of 200N; however, when on a soft backing the patches exhibited pulloff forces of up to 3N when subjected to a 50N preload. The soft backing allowed more of the hairs to make contact with the substrate, further emphasizing the need for compliance. However, the patches were quickly destroyed after a few attachment/detachment cycles due to broken and fallen over hairs.

Another synthetic adhesive used silicone rubber molded into a polycarbonate

membrane with an array of nanopores [104, 105, 106]. The molding process created a random array ($\approx 5\text{x}10^4\text{pores/cm}^2$) of hairs about 6$\mu$m in diameter and length. A maximum adhesive pressure of 2.8mN/cm^2 was measured on a flat glass substrate with an applied preload of 25mN. The same authors also tried molding 200nm diameter and 60μm long hairs out of polyimide but found that the aspect ratio of the hairs was too high, leading to clumping and self-sticking, effectively eliminating any possible adhesion.

Other techniques for fabricating synthetic adhesives have focused on creating even smaller feature sizes. In one case, multi-walled carbon nanotubes (MWCNT) $10 - 20$nm in diameter and 25μm long were constructed on a polymer backing [122] and exhibited an adhesion strength of $\approx 16\text{x}10^2\text{N/cm}^2$ (more than 200 times higher than that of a single gecko setae, 10N/cm^2 [14]) when tested using atomic force microscopy (AFM) with probe tips < 10nm. A more recent study tested flat, $4 - 8$mm^2 patches of MWCNT, $20 - 30$nm in diameter and $5 - 10\mu$m long, grown on a silicon substrate with preloads less than 20N on glass and other substrates [123]. These samples exhibited pulloff strengths of up to ≈ 12N/cm^2 for the smaller patches and up to ≈ 2N/cm^2 for the larger patches, and Work of Adhesion values between 20mJ/m^2 and 80mJ/m^2 [123]. Another approach used micro-electromechanical systems (MEMS) techniques to grow organic looking polymeric nanorods ("organorods") on a compliant silicon substrate [84, 85, 86]. The organorods, ≈ 200nm in diameter and 3μm long, were tested with a 25mm^2 flat punch and exhibited adhesive strength of up to 1.7mN/cm^2.

While the adhesion values quoted for the MWCNT samples discussed above are quite impressive, there were also some problems with the samples and assumptions in the calculation of adhesive strength. The samples required rather large amounts of preload force compared to the adhesive force that was measured and, in one case, the MWCNT's performance quickly degraded with repeated attachment/detachment cycles. But perhaps even more problematic are the test sample sizes, only on the order of tens of nm in [122]. In [123] it was already seen that adhesion began to drop as the sample size increased. One of the outstanding features of the gecko adhesive system is that it generates significant adhesion at the macroscopic scale of

centimeters. While very fine structures such as MWCNT can generate significant adhesion at small scales, there is still the challenge of creating compliance at larger length scales to allow the MWCNT to make intimate contact with rough surfaces. The organorods were fabricated on a compliant backing and tested with a relatively large patch area ($25mm^2$), however, they showed orders of magnitude less strength than that observed for a gecko.

A number of researchers have recently been focusing on using polymers and molding techniques to create synthetic adhesive patches (Figure 2.12) [42, 57, 66, 69]. Materials used have included polymethylmethacrylate, polystyrene, UV-curable polymer resin, polydimethylsiloxane, and polyurethane. All of the synthetic adhesives are comprised of arrays of vertically oriented fibrils ranging in diameters from 80nm to $4.5\mu m$ and in length from $1\mu m$ to $20\mu m$. Testing these patches has been done using AFM probes as small as 90nm to as large as 6mm in diameter, and in one case, using a flat substrate with a sample size of $25mm^2$. Adhesion strengths have been reported as large as $18N/cm^2$ for a preload of $12N/cm^2$ with a corresponding Work of Adhesion of up to $11J/m^2$ [69].

Of the synthetic adhesives fabricated from molding, the most promising work to date has been reported in [21, 43, 87, 115]. This research has led to a biomimetic mushroom-shaped fibrillar adhesive molded from polyvinylsiloxane (PVS). The fibrils in this adhesive are about $100\mu m$ in height, have a $60\mu m$ base diameter, a $35\mu m$ middle diameter, and a $25\mu m$ neck diameter just below a terminal plate (Figure 2.12). At the tip of the structures is a thin plate ($2\mu m$ thick at the plate edges) about $40\mu m$ in diameter, giving rise to their mushroom shape. Testing of an $\approx 5mm^2$ patch of this synthetic adhesive produced an adhesion strength up to $5.6N/cm^2$ for a wide range of preloads ($50 - 130mN$). These samples were also shown to have better contamination resistance compared to bulk PVS, and completely regained their adhesive strength after contamination upon a thorough cleaning with soap and water. Finally, the friction characteristics of the structured PVS were also higher than the unstructured sample. The structured sample exhibited a static friction coefficient of 3.5 versus 3.2 for the unstructured PVS and a kinetic friction coefficient of 3.5 versus 0.8 for the unstructured PVS.

Measure	Gecko[a]	Geim[b]	Sitti[c]	Zhao[d]	Northen[e]	Kim[f]	Gorb[g]
Material	β-Keratin	Polyimide	Silicone Rubber	Carbon Nanotubes	Polymer Nanorods	Poly-urethane	Polyviynl-siloxane
Typical Bulk Stiffness (GPa)	1-3	3	.0006	1000	Not given	0.003	0.003
Feature Diameter (μm)	0.2	0.5	6	20-30	0.2	9	40
Feature Length (μm)	30-130	2	6	5-10	3	20	100
Tested Patch Size (mm²)	100	100	50	4	25	225	6.6
Max Adhesion Pressure (kPa)	100	30	.028	117	0.017	180	60
μ' (at kPa)	8 to 16	0.06 (30)	0.06 (.028)	0.02 (117)	0.3 (0.017)	1.5 (180)	7.5 (55)
Dirt Resistant	Yes	Likely	No	Likely	Likely	No	No

Table 2.1: Comparison of different gecko-inspired synthetic adhesives. a, References [8, 14, 16]; b, References [40]; c, References [104, 105, 106]; d, References [123]; e, References [84, 85, 86]; f, References [69]; g, References [21, 43, 87, 115].

Important characteristics of some of the more notable synthetic adhesives described above are summarized in Table 2.1. Each of the solutions shown in Table 2.1 has certain advantages and mimics various aspects of the gecko adhesion system. The adhesives that use stiff bulk materials have the potential to be self-cleaning and non-sticky by default. The softer adhesives tend to achieve adhesive pressures on the same order as the gecko for relatively large test areas, and some of the synthetics discussed exhibit μ' values approaching those of the gecko. However, none of these adhesives has demonstrated the first three characteristics listed previously: directionality, high μ', and low detachment force.

Some of the most recent work has produced slightly angled fibrillar arrays in an effort to better mimic the gecko adhesion system [2]. The polyurethane fibrils are about 20μm in diameter, 30μm to 100μm in length, and angled at about 25° from vertical. Adhesion pressures between 10kPa to 30kPa were reported for preload values of about the same range. These values are promising but results were not reported

on whether or not the angled stalks exhibit any of the directional characteristics observed for the gecko. While all aspects of the gecko adhesion system are desirable, the directionality, high μ', and low detachment force and why they are important for climbing are discussed next.

2.5 Directional Adhesion for Climbing

In Section 2.3 many aspects of the gecko adhesion system were discussed. Here, the focus will shift to one aspect of the gecko adhesion system in particular — directionality. Visual inspection and microscope photographs [16, 95, 96, 97] of gecko toes show that the lamellae, setae, and spatulae are angled and not perpendicularly oriented with respect to the gecko toe. However, it was not until recently that studies have shown why the gecko may have developed this geometric feature.

The first study to show the directional nature of the gecko adhesion system performed experiments on single gecko setae [14]. This study tested the adhesion of individual setae and found that adhesion was strongly dependent on three-dimensional orientation. When loading the setae with the spatulae pointing away from the surface less than 0.3μN of adhesive force was measured and when loading the setae with the spatulae pointing toward the surface up to 0.6μN of adhesive force was measured. However, when loading the setae in *both* the perpendicular *and* parallel directions with spatulae pointing toward the surface up to 13.6μN of adhesive force was measured. Using this method of perpendicular preload combined with a parallel drag preload, the maximum adhesive force of a single seta averaged 194μN [14]. These results clearly show that the gecko adhesive system needs to be loaded in the right direction in order to achieve good adhesive performance.

The same study also looked at the detachment of a single gecko seta. At detachment, the angle between the setal stalk and the test substrate was found to be similar among setae, at about 30°. Further tests were performed by controlling the adhesive force while rotating the setae. A critical angle of detachment at about 30° was found that was roughly independent of the adhesive force at detachment $(0 - 20\mu$N). This finding predicts that the loading vector at a seta (or foot) contact must be within 30°

of the surface to sustain adhesive forces. Another study of the climbing dynamics of the gecko provides qualitative support for these findings [13]. While climbing, geckos tend to pull all four of their feet inwards toward their center of mass, which may be one mechanism by which they load their feet in the proper parallel directions to generate adhesion and keep the loading vectors at their feet below the critical angle of detachment.

Further studies were performed on gecko lamellae (setal arrays) and whole toes. In [11] lamellae were dragged along surfaces with and against their natural curvature while measuring the generated contact forces. When dragged *with* the natural curvature of the arrays, adhesion was present, but, when dragged *against* the curvature, only friction was observed. The combined force vector at the contact, perpendicular and parallel force components, during sliding of the lamellae had a roughly constant angle of about 30°. Whole toes of the gecko were tested by first adhering a single toe of a live gecko, with and without added weight in the form of a "backpack", to a smooth vertical surface. The angle of the vertical substrate was then rotated past 90°, toward overhanging, and the angle at which the gecko's toe detached from the surface was recorded. The detachment angle across a range of backpack weights was roughly constant at 30°. These results, along with previous results on single setae, have led to a simple empirical model to describe the directionality of the gecko adhesive system. This model, termed "Frictional Adhesion," states that the adhesion force is directly proportional to the applied shear load at the contact when loaded in the primary adhesive direction. When loaded in the opposite direction, simple Coulomb friction describes the contact behavior.

The directional nature of the Frictional Adhesion model is readily seen in Figure 2.13, which shows the limit surface of the model in force-space in the same way that contact and adhesion models were described in Sections 2.1 and 2.2. When loaded in the proper adhesive direction, adhesive forces can be sustained in proportion to the tangential load applied. When loaded in the opposite direction, Coulomb friction is observed. An upper limit is placed on the shear load that can be applied, which is a function of the substrate strength, limb strength, and adhesive strength; however, the exact relationship between the perpendicular and parallel forces at high shear
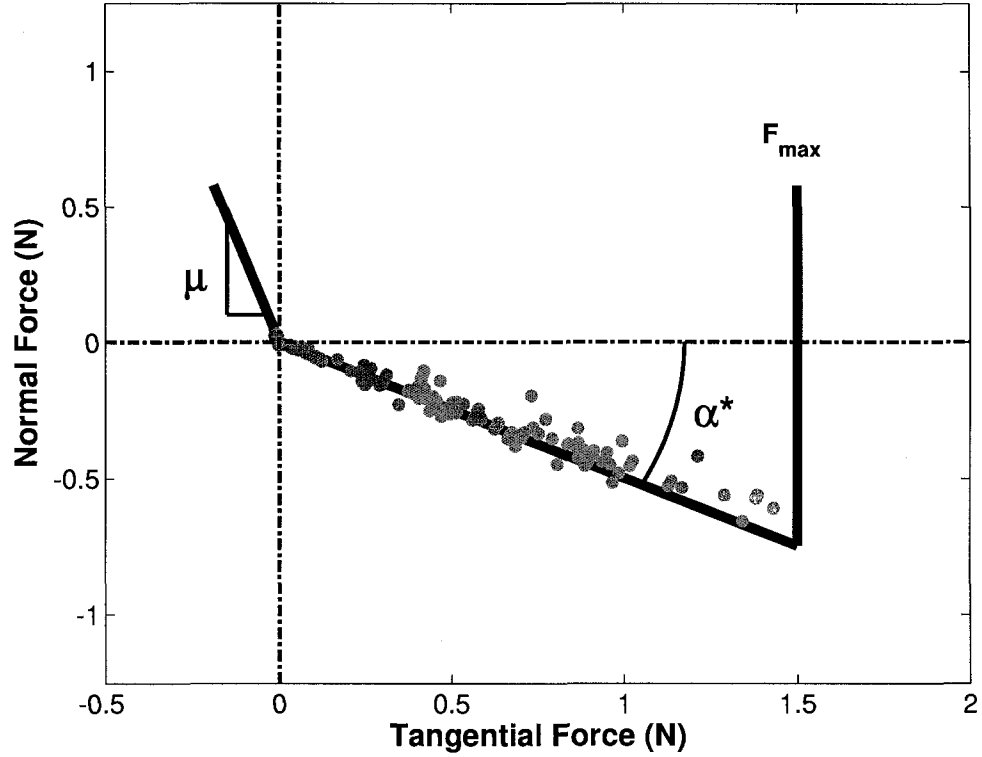
Figure 2.13: Frictional Adhesion model in force-space given in [11]. Data points are from [11, 14] for gecko setae, lamellae, and whole toes. In the preferred adhesive direction (positive tangential), adhesion force is directly proportional to applied tangential force. In the negative tangential direction, Coulomb friction is observed. An (currently arbitrary) upper limit is placed on the amount of tangential force that can be applied, which is a function of material, contact, and limb strength.

loads is currently unknown for the gecko (i.e. the saturation details are unknown). Mathematically, the Frictional Adhesion model is described by the following set of equations:

$$
\begin{array}{ll}
F_N \geq -\frac{1}{\mu}F_T \\
F_N \geq -\tan(\alpha^*)F_T
\end{array}
\left\{
\begin{array}{l}
F_T < 0 \\
0 \leq F_T \leq F_{max}
\end{array}
\right.
\tag{2.19}
$$

F_N is the normal (perpendicular) force, F_T is the tangential (parallel or shear) force, μ is the coefficient of friction, α^* is the critical angle, and F_{max} is the maximum limit on tangential force. Data from [11, 14] for setae, lamellae, and whole toes are also

plotted in Figure 2.13, representing the maximum forces at the time of pulloff and forces sustained during sliding, both of which characterize the forces that the contact can sustain without failure.

The Frictional Adhesion model captures the first three features of the gecko adhesive system listed in Section 2.3. Directionality is simply achieved because frictional adhesion only exhibits adhesion when there is a positive tangential force, corresponding to the preferred loading direction of the gecko adhesive. Frictional adhesion can also achieve a high value of μ' because the adhesive pulloff forces are not solely a function of the applied normal preload force. In practice, a small preload force is needed to establish initial contact; however, the applied tangential force is what then aligns the setae and brings large numbers of spatulae into contact. Finally, low detachment forces also follow from the model — it suffices to relax the applied tangential force, thereby moving toward the origin in Figure 2.13. As the tangential force is reduced to zero, the amount of sustainable adhesion also drops to zero allowing the foot contact to separate with very small detachment forces. In summary, the Frictional Adhesion model describes a *controllable adhesive system*: adhesion in the normal direction is controlled indirectly by controlling the applied tangential force.

2.6   Summary

When studying climbing, it becomes important to study contact. Climbing vertical surfaces requires some amount of adhesive force to resist pitch-back moments. In order to design and control climbing robots it is necessary to have a good understanding of the interactions at the contact interface that will provide the necessary adhesive forces for climbing.

The discussion in the previous sections has provided a background in contact and adhesion modeling. Some of the fundamental contact and adhesion models have been presented and summarized, including the Coulomb friction model, JKR model, and Kendall Peel model. This work is concerned with the *forces* that can be transmitted at a contact, and as such, the concept of a limit surface has been introduced. A limit surface is a concise description of the forces that can be withstood by a contact

interface without failure of the contact. Failure of the contact has been defined to be when the two objects in contact slide relative to one another or physically pull apart from one another.

These topics provide a framework for understanding the directional adhesive system of the gecko lizard and how it allows the gecko to climb so well. The Frictional Adhesion model was introduced as a simple way to capture the macroscopic behavior of the gecko adhesive system. While the synthetic adhesives that have been created to date have been able to duplicate some of the extraordinary features of the gecko adhesive, none have duplicated the directional nature of the gecko adhesive. The next chapter will cover the design, manufacture, and testing of a synthetic adhesive that does have the directional property so desirable for climbing.

Chapter 3

Experimental Investigation of Directional Adhesion

The previous chapter discussed various desirable aspects of the gecko adhesive system. Many synthetic adhesives have been developed in order to capture some of the gecko's abilities; however, none have focused on the aspects of gecko adhesion that are most important for climbing. This chapter looks at a new synthetic adhesive designed to capture the three characteristics of gecko adhesion that enable smooth controlled climbing — directionality, high pulloff to preload ratio, and low detachment forces.

The design and fabrication of this synthetic adhesive are discussed briefly. To asses this adhesive, experiments were performed to quantify its behavior when in contact with a glass substrate. The details of a custom experimental setup are given along with a description of the experimental procedures that were developed to test this adhesive. The experiments improve upon previous work by testing the adhesive structure in a three-dimensional manner, whereas previous investigations have only looked at adhesion in the normal direction. This discussion provides a general methodology for testing arbitrary adhesive structures.

The main focus of this chapter is to present experimental results gathered for the adhesive. The effects of various experimental parameters, including preload magnitude, pulloff angle, and speed, are explored. Contact failure forces are compared to

some of the adhesive contact models discussed in the previous chapter. The new synthetic adhesive is primarily assessed in terms of its ability to reproduce the desired qualities of the gecko adhesion system for climbing.

3.1 Design and Fabrication of a Directional Adhesive

The directional nature of the gecko's adhesion system arises from the geometry of its adhesive structures. Figure 2.11 shows how the lamellae, setae, and spatulae are not oriented vertically or straight. Instead, these structures are all angled and curved with respect to the contact normal when the gecko's toes are in contact with a flat substrate. The angled and curved nature of these structures imparts an overall direction to the adhesive system. Any synthetic adhesive attempting to reproduce this directionality cannot be vertically symmetric but must instead also use some type of angled geometry.

This chapter presents a synthetic adhesive, termed Directional Polymer Stalks (DPS), that reproduces the directional nature of the gecko's adhesive system [100]. Like other synthetic adhesives, the DPS consist of a fibrillar array that interacts with a surface to produce adhesion mainly via van der Waals forces. The directional behavior of the DPS arises from their geometry, which is inspired by the angled, curved shape of gecko setae.

3.1.1 Design Parameter Effects

The primary goal of the new synthetic adhesive is to reproduce the directional property of the gecko adhesion system. Angled stalks with angled faces were tentatively chosen for this based loosely on observations of the geometry of gecko setae. In order to achieve this geometry, conventional manufacturing technologies (e.g. drilling and milling) were used rather than many of the lithographic techniques described in Section 2.4. Those methods offer the potential to create very small features; however, they are generally limited to creating two-dimensional patterns or three-dimensional

patterns with stair-stepping effects. This initial design choice limited many other aspects of the design.

While the primary goal of the DPS is to exhibit directionality, they must also still remain adhesive. A material's stickiness is related to something mentioned earlier called the Dahlquist Tack criterion [32]. The Dahlquist Tack criterion states that a material becomes tacky if its modulus of elasticity is less than about 100kPa and is based on experimental results testing different Pressure Sensitive Adhesives (PSAs). Below 100kPa a material becomes soft enough to "flow" into the substrate and create enough real area of contact that van der Waals forces become significant. However, the gecko adhesion system is made from β-keratin, which has a bulk stiffness of approximately 1GPa. It achieves an effective stiffness less than the Dahlquist Tack criterion because of the hierarchical branching system, extremely small features, and the ability of individual fibrils to conform to surface asperities.

Previous synthetic adhesives were primarily interested in reproducing the dry and self-cleaning properties of the gecko adhesion system. To this end, they also use relatively stiff bulk materials; however, large real areas of contact are still generated by using very small features. When using conventional manufacturing processes, the smallest size of the features is very limited when compared to the lithographic techniques discussed in Section 2.4. Specifically for the DPS, the features were limited by the size of available drills and end mills, among other tools.

The size limitation can potentially cause problems when creating an adhesive that makes use of van der Waals forces. Because of the larger feature sizes, the DPS require a much softer bulk material to achieve good conformation to the substrate. The DPS are made from an elastomeric material with a Young's modulus of $\approx$ 300kPa that allows enough conformation for van der Waals forces to remain significant. Essentially, as feature size increases and the adhesive structures approach the case of a featureless bulk material, the stiffness must decrease in order to maintain good conformation.

However, problems can also arise if the bulk materials is too soft. As mentioned before, previous efforts have tried to reproduce the self-cleaning properties of the gecko by using stiff bulk materials. Unlike the stiff β-keratin of the gecko, the DPS attract dirt and become contaminated with extended use. This is similar to the manner in

which PSA tapes quickly stop working after repeated use. Although in contrast to PSAs, the bulk material of the DPS is not so soft that it cannot be cleaned and regain its adhesive properties.

Various other parameters must also be considered in addition to the overall feature size and material stiffness. The fibrillar nature of the DPS and other synthetic adhesives increases their adhesive capabilities. The individual fibrils are able to conform independently to the substrate and thereby increase the real contact area. They also serve to stop cracks from propagating since if one fibril detaches a new crack must initiate at the next fibril before it can detach. Splitting up of the contact area as a method of enhancing adhesion has been noted by others as well [87].

When using fibrillar structures to enhance adhesion, their geometric properties must be specified — in particular, the aspect ratio of the fibrils [120]. If the fibrils are too long and skinny they start to clump together and the overall adhesion is reduced. On the other hand, if they are too short and fat, then their ability to individually conform to surface asperities is reduced. The optimal range for the aspect ratio of the fibrils depends on the bulk material stiffness, the surface energy of the bulk material, and the spacing of the fibrils [120]. In general, the higher the aspect ratio (length to width) the greater the ability of the structures to conform to the surface and generate real contact area. The fibrils in the DPS have a length to width ratio of about 3 to 1. Any longer and significant clumping of the fibrils begins to reduce the overall adhesion. Stiffer materials can achieve higher aspect ratios, most notably the gecko, whose setae have an aspect ratio on the order of 10 or 20 to 1 [96, 97].

Finally, tip geometry must also be carefully chosen. Poor tip geometries can lead to high stress concentrations causing crack initiation leading to quick detachment. Good tip geometries distribute stress evenly across the entire contact area so that at failure, the entire surface detaches almost at once. The influence that tip geometry plays is also dependent on the feature size of the contacting elements [39]. The difference between good and bad tip geometries becomes insignificant when feature sizes are less than about 100nm, but at feature sizes on the order of hundreds of micrometers the pulloff forces can vary by a factor of 100 [39].
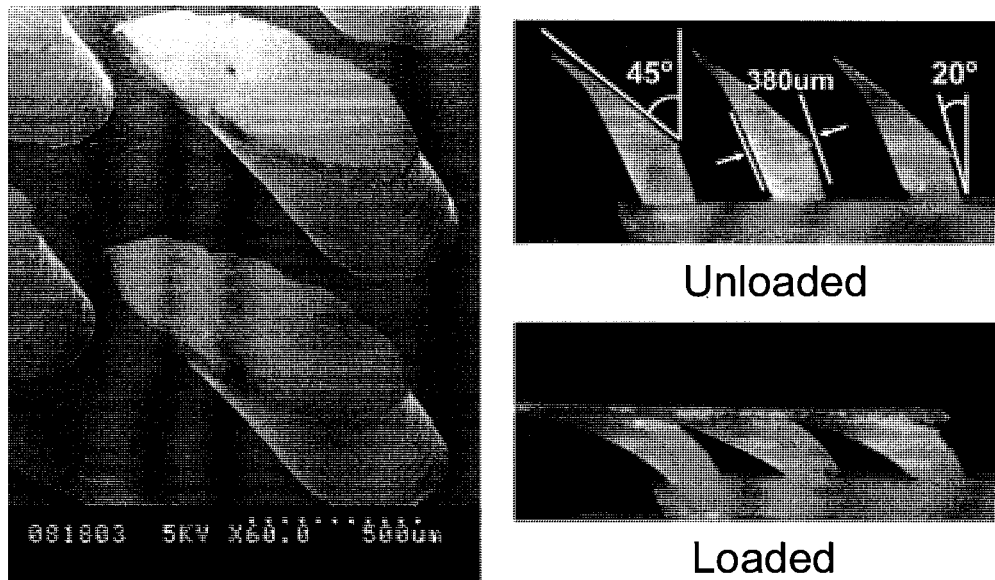
Figure 3.1: DPS geometry. The geometry of the DPS is shown in the upper right. The stalks are 380μm in diameter and about 1mm long. They are angled at 20° with respect to vertical, and the stalk faces are angled at 45° with respect to vertical. An SEM photograph of the DPS is shown on the left, and the DPS in the loaded state are shown in the bottom right, illustrating how the DPS conform to a substrate.

All of these different design parameters must be considered when creating a synthetic adhesive. Ideally, it would be possible to mimic all of the aspects of the gecko adhesion system but current technology is not yet capable of doing so. However, by making certain design trade-offs and understanding the relationship between some of these different parameters it is possible to reproduce some of the characteristics of the gecko adhesion system while sacrificing others. Here, those choices were made to primarily capture the directional nature of gecko adhesion by using angled stalks with angled faces. The initial choice of these angles was made somewhat arbitrarily based loosely on the geometry of the gecko adhesion system and was limited by readily available tools. It remains an area of future work to more fully understand the relationship between the specific angles of the fibrils and their adhesive characteristics.
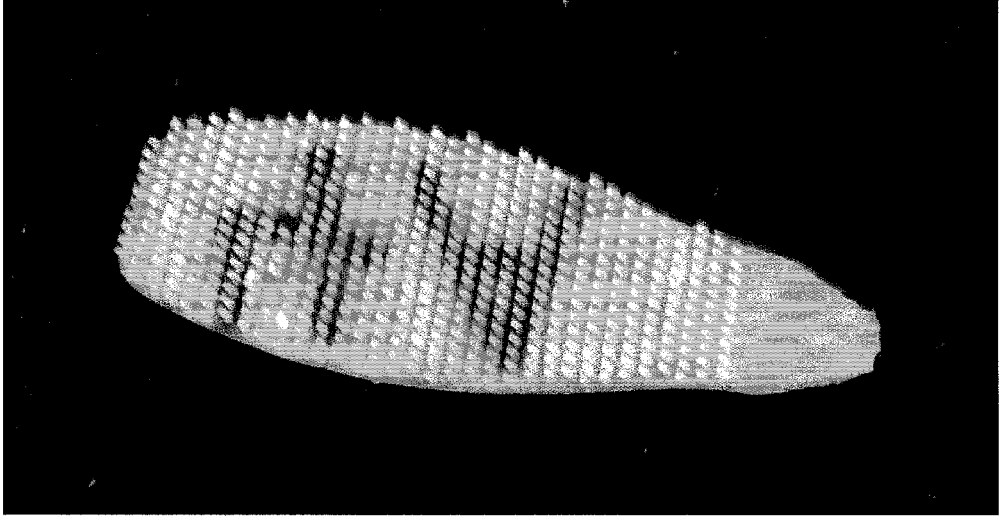
Figure 3.2: Typical patch of DPS. The DPS are manufactured in roughly elliptical patches about 4cm^2 in area for use on a climbing robot.

3.1.2 Directional Polymer Stalks

Figure 3.1 shows the final geometry of the DPS. Stalks are $\approx$ 1mm long from base to tip and 380μm in diameter, extending from a substrate of bulk material that is roughly 250μm thick. The stalks are angled at 20°, and the stalk faces are angled at 45° with respect to vertical. They are arranged in a hexagonal pattern for maximum stalk density, and their centers are spaced 1mm apart. The DPS are manufactured in patches that are ultimately used as toes on a climbing robot [70]. Each patch is about 4cm^2 in area, roughly elliptical in shape, and contains about 500 angled stalks. Figure 3.2 shows a picture of one patch of the DPS.

The DPS patches are created by casting a liquid polyurethane (Innovative Polymers IE-20 AH Polyurethane, 20 Shore-A hardness, E $\approx$ 300kPa) into a custom mold (Figure 3.3). The mold used to create the DPS consists of three parts. The middle mold is created from 1.6mm thick Delrin, which has low-surface energy so it does not bond to the curing polymer. First, V-shaped grooves are cut into the Delrin using a custom slitting saw with a 45° bevel. A silicone rubber (TAP Plastics Silicone RTV Fast Cure Mold-Making Compound) is cast on top of the middle mold to create a
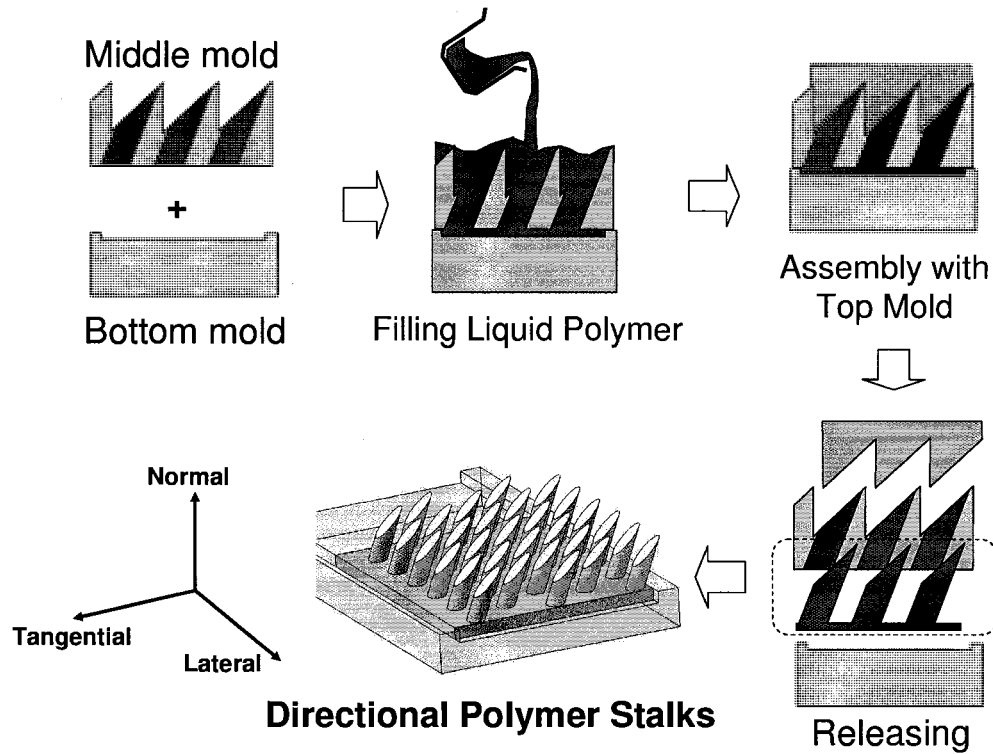
Figure 3.3: Manufacturing process of the DPS. Liquid polyurethane is poured into a three part mold. Once the polymer cures, the mold is disassembled, releasing patches of DPS.

well-matched top mold. Holes are then drilled at 20° on the 45° faces left from the earlier cutting operation, completing the middle mold. The bottom mold is made from hard wax and provides the final patch shape.

The bottom and middle molds are assembled, and then liquid polymer is poured into the mold. The top mold is then applied and squeezes any excess polymer out the sides of the fully-assembled mold. The polyurethane cures and the DPS patches are released by disassembling the mold. An alternative molding process not involving a top mold has also been used. In this process, excess polymer is simply wiped away and the tips of the DPS are allowed to cure while exposed to air and atmospheric moisture, resulting in a softer final product. This process creates stickier tips; however, results are less repeatable due to variations in ambient humidity and the wiping process.

Consequently, the second process was abandoned and all results shown in this chapter are from patches manufactured using the first method.

3.2 Experimental Apparatus

The DPS were designed and manufactured to reproduce the directionality of the gecko adhesive system. In order to test the adhesion characteristics of the DPS it was necessary to setup an experimental testing system. The experimental apparatus should allow the DPS to be brought into contact with and pulled away from various substrates. As in previous studies ([11, 14]; Section 2.4), controlled motions can be applied to the DPS patches causing forces to be transmitted at the contact that can then be measured.

Previous investigations of synthetic adhesives (Section 2.4) have generally involved preloading samples against a substrate and then pulling them off, applying motions and measuring forces only along the normal direction. This has allowed researchers to compare maximum pulloff forces, the Coefficient of Adhesion (μ'), and the Work of Adhesion (W_{adh}) of synthetic adhesives to each other and to the gecko adhesion system. However, this type of testing, purely in the normal direction, results in a one-dimensional characterization of adhesion. To study directionality, it is implicitly necessary to explore how motions and forces in the two parallel directions affect adhesion. The adhesive forces of single gecko setae are strongly dependent on three-dimensional orientation and loading [14]. Furthermore, the directionality of lamellae only became apparent when they were brought into contact with the substrate and *dragged* across the substrate — motion and forces in two directions [11]. While one-dimensional experiments offer some insight into adhesion, three-dimensional experiments are necessary in order to fully characterize a directional adhesive such as the DPS.

3.2.1   Mechanical Setup

The mechanical setup of the experimental apparatus consists of a motion stage and a sensing device. The motion stage is a 3-axis positioning stage (Velmex, Inc.; MAXY4009W2-S4, MA2506B-S2.5) that uses lead screws to provide linear motion. Two of the lead screws have a pitch of 0.2in/rev, and the third lead screw has a pitch of 0.05in/rev. The axes with the two coarser lead screws are used to generate motions in the directions parallel to the contact normal (X and Y axes) while the axis with the finer lead screw is used to generate motions along the contact normal (Z axis). The three lead screws are each driven by a 24V DC motor (Pittman; GM9236S015-R1) with a gear head ratio of 5.9 : 1. Each motor has a 500count/rev quadrature encoder used to provide relative position measurements for each axis of motion. The entire positioning stage was rigidly clamped to a typical laboratory bench.

The sensing device consists of a 6-axis force/torque sensor (ATI Industrial Automation; Gamma Transducer SI-32-2.5) mounted to a 2-axis manual tilt stage (Newport Corporation; 30 Series Tilt Platform, Model 39). The force/torque sensor has a resolution of 1.56mN in F_X and F_Y, 3.13mN in F_Z, and 125μNm in T_X, T_Y, and T_Z. The sensing range is $\pm$32N in F_X and F_Y, $\pm$100N in F_Z, and $\pm$2.5Nm in T_X, T_Y, and T_Z. The sensor has a resonant frequency of 1.4kHz in F_X, F_Y, and T_Z and 2.0kHz in F_Z, T_X, and T_Y. The tilt stage is used to provide rotations about X and Y to align the sensing device to the motion stage in the two axes perpendicular to the contact normal. The rotation about each axis is controlled manually via an adjustment screw. The entire sensing structure is rigidly mounted to a laboratory wall near the motion stage.

An end effector arm is attached to the motion stage to position the sensing device within the work range of the motion stage. The motion stage also includes limit switches to prevent any axis from crashing into its physical limits. Each axis was cycled approximately 1,000 times to "break-in" the motion stage. All of the ways and lead screw nuts were then adjusted via their respective adjustment screws in order to minimize wobble in the ways and backlash in the lead screws. Using this setup, test substrates can be mounted to the sensing device and adhesive samples can be mounted to the motion stage, or vice versa. A schematic diagram of the
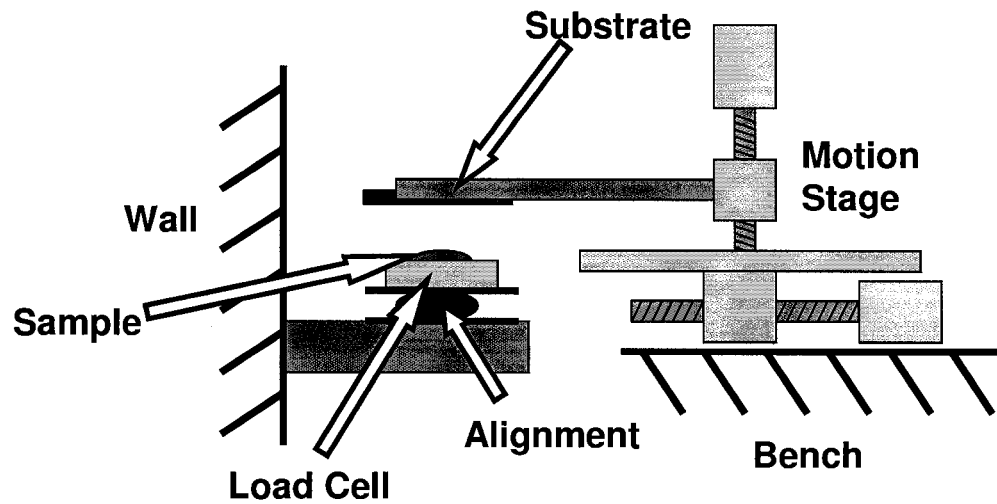
Figure 3.4: Schematic diagram of mechanical setup.
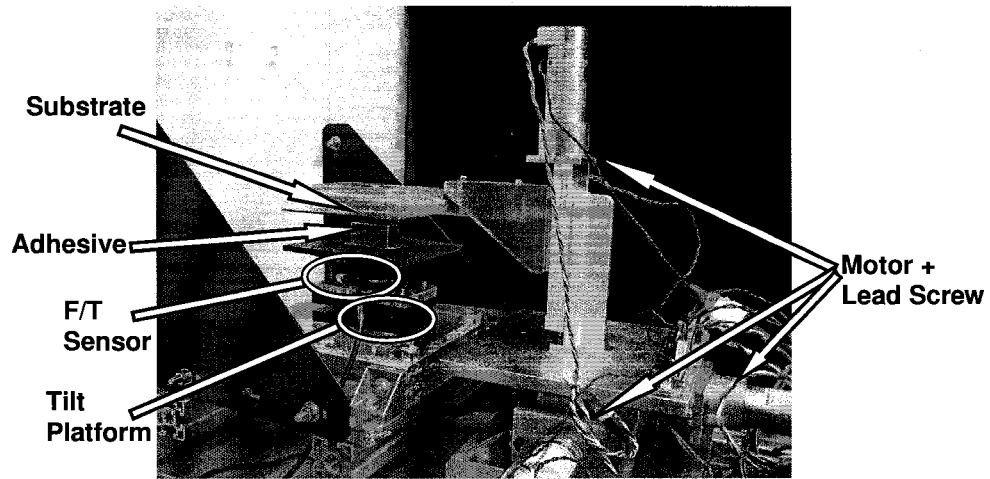
Figure 3.5: Photograph of mechanical setup.

mechanical setup is shown in Figure 3.4, and a photograph of the setup is shown in Figure 3.5.

```
┌──────────┐      ┌──────────────────┐      ┌──────────┐
│ Desktop  │◄─────│  Power Supply and│◄────►│   F/T    │
│ Computer │◄─────│   Interface Box  │◄────►│  Sensor  │
└──────────┘      └──────────────────┘      └──────────┘
     ↕
┌──────────────────┐                        ┌──────────┐
│ Microcontroller  │◄───────────────────────│    DC    │
│      Board       │◄───────────────────────│ Encoders │
└──────────────────┘                        └──────────┘
        │           ┌──────────┐            ┌──────────┐
        └──────────►│Protection│◄───────────│  Limit   │
                    │  Board   │◄───────────│ Switches │
                    └──────────┘            └──────────┘
                         ↓
                    ┌──────────┐            ┌──────────┐
                    │ H-Bridges│═══════════►│ DC Motors│
                    └──────────┘            └──────────┘
```
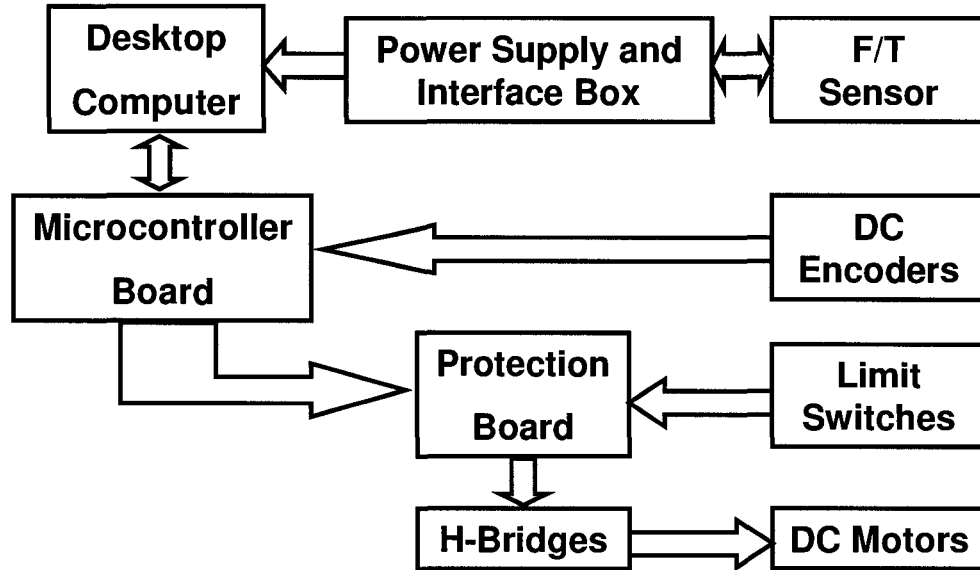
Figure 3.6: Schematic diagram of the electronic setup.

3.2.2 Electronic Setup

The electronic setup of the experimental apparatus consists of both custom-built and off-the-shelf components. The force/torque sensor is connected through a Power Supply and Interface Box (ATI Industrial Automation) to a data acquisition card (National Instruments; PCI-6034E) inside a desktop computer. Each of the DC motors is driven by a standard H-bridge (National Semiconductor; LMD18200) capable of sourcing up to 3A. The motion stage limit switches and H-bridges are connected to a custom Protection Board that prevents any of the motors from driving the stage axes into their physical limits. The motor encoders and the Protection Board are connected to a microcontroller development board (Microchip Technology, Inc.; PICDEM2 PLUS) with an 8-bit microcontroller (Microchip Technology, Inc.; PIC18F4431). Finally, the microcontroller board is connected to the desktop computer via an RS-232 serial cable. A schematic of the electronic system is shown in Figure 3.6.

3.2.3 Software Control and Data Acquisition

The software required to run the experimental apparatus consists of two custom-written modules. An embedded C program residing on the microcontroller is responsible for control of the motion stage. The microcontroller sets the voltage applied at the motors via Pulse-Width Modulation (PWM) at 39kHz and keeps track of the relative position of the stage via the encoder signals. The software can perform both open-loop and closed-loop control of the stage in order to provide useful operation modes for the user. When closed-loop control is used, a simple proportional controller operates at a 1kHz update rate. The gain of the proportional controller is $\approx 90\text{mV}/\mu\text{m}$ for the X and Y axes and $\approx 360\text{mV}/\mu\text{m}$ for the Z axis. The mechanical damping in the motion stage itself is sufficient to ensure a stable controller. The final type of controller and controller gain used was arrived at empirically.

The embedded software has 5 different modes of operation: 1) Manual Jog, 2) Manual Step, 3) Cycle, 4) Alignment, and 5) Trajectory. A simple keypad is provided to switch between modes and provides full control within a mode except for the Trajectory mode, which also requires the serial interface. The serial interface operates at a baud rate of 115200. In Manual Jog mode the user can apply a voltage input to each motor in order to jog each axis to a desired position. While Manual Jog mode can quickly move the end effector of the stage to an approximate position, it is not intended to provide precise motions. In Manual Step mode the user can move the stage to a desired set point. The microcontroller runs the closed-loop proportional controller using the set point given by the user. Cycle mode repeatedly jogs each axis of the stage from one end of its work range to the other at a speed controlled by the user. The Alignment mode is a combination of jogging the Y axis back and forth while stepping the Z axis to a desired set point using the closed-loop controller. While these first four modes are used to setup the stage for running experiments, the Trajectory mode is used to actually perform experiments.

The Trajectory mode is able to execute prescribed motion paths in three dimensions. In this mode, the microcontroller looks for two different commands on the serial interface: 1) 'T' for Trajectory or 2) 'G' for Go. After receiving the Trajectory command the microcontroller expects to receive a properly formatted trajectory. A

trajectory consists of a series of entries, each of which is a timestamp in milliseconds and a position in encoder ticks. The microcontroller uses these entries and linear interpolation to create a discrete function in time of desired positions for the closed-loop controller. Once a trajectory has been properly downloaded the Go command can be issued and the microcontroller will execute the last trajectory that was downloaded. While executing a trajectory the microcontroller will send the motion stage's current position (in encoder ticks) every 2ms (500Hz) to the desktop computer via the serial interface.

The second part of the software required to run the experimental apparatus consists of a custom-written LabView program (National Instruments, Inc.; LabView 7) running on the desktop computer. The computer runs WindowsXP with a 2.0GHz processor and 1GB of RAM. The LabView program interfaces with the Trajectory mode of the microcontroller software. It is able to log the position data from the microcontroller at 500Hz and also the force and torque data from the data acquisition card at 1kHz. The LabView program first loads a trajectory file, which is simply a series of tab and line delimited numbers written in a plain text file. LabView then converts this file into the proper format and downloads the trajectory to the microcontroller. The Go command is sent to the microcontroller and LabView begins to log both force/torque and position data to a log file specified by the user. Multiple experiments can be run in batches by providing the LabView program with a batch file containing a list of trajectory files and corresponding log files.

3.2.4 System Characterization

The closed-loop performance of the system was characterized by looking at the step-input and ramp-input responses of the motion stage. A 100μm step-input was given to each of the three axes and the actual position (as recorded via the motor encoders) of the stage was recorded. The typical response to a step-input for each axis is given in Figure 3.7. The steady-state error is typically less than $\pm10\mu$m for the X and Y axes and less than 1μm for the Z axis. The damping ratio for axes X and Y is about 0.35 and the natural frequency is about 140Hz. For the Z axis, the damping ratio is
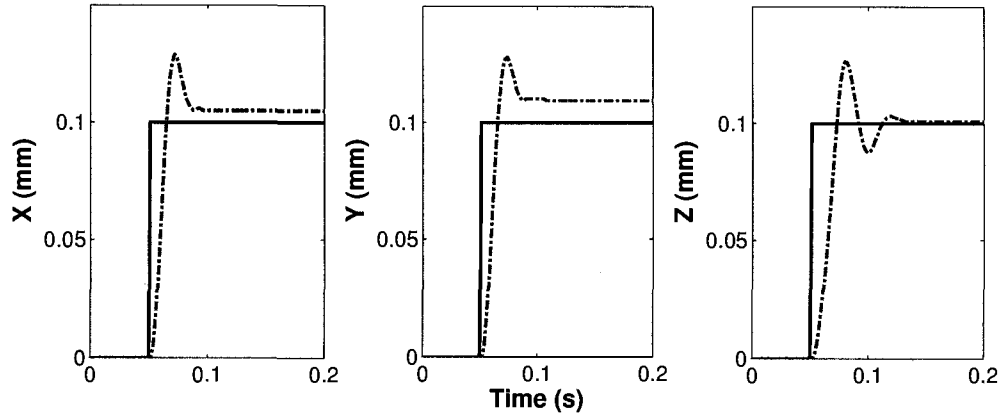
Figure 3.7: Typical step response of each axis of the positioning stage to a 100μm step input. Steady-state errors are less than about 10μm in X and Y and less than about 1μm in Z.
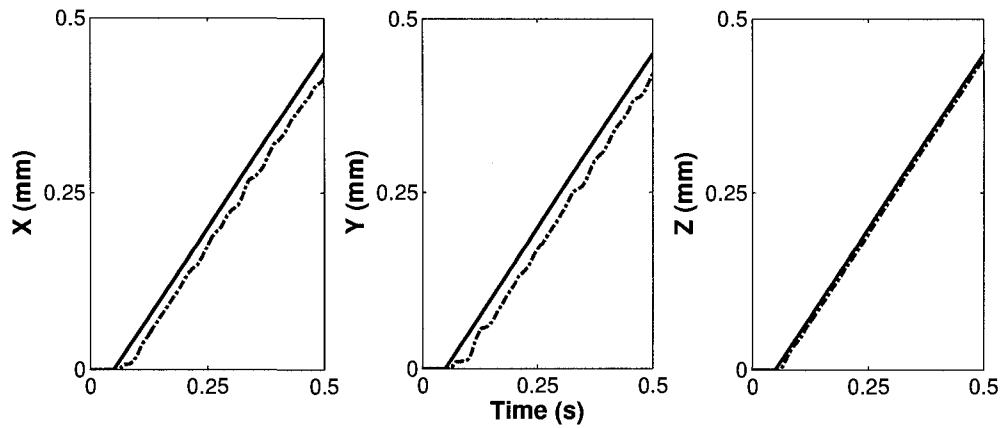
Figure 3.8: Typical ramp response of each axis of the positioning stage to a 1mm/s ramp input. Steady-state errors are less than about 25μm in X and Y and less than about 5μm in Z.

about 0.40 and the natural frequency is about 105Hz.

A ramp input of 1mm/s was also given to each axis to determine the tracking ability of the stage. The typical response from each axis is shown in Figure 3.8. The steady-state error is less than about $\pm$35μm for the X and Y axes and less than about $\pm$8μm for the Z axis.

3.3   Experimental Procedure

Adhesion tests were performed on the synthetic adhesive patches described in Section 3.1 using the experimental apparatus described in the previous section. After manufacturing, samples were prepared for experimental testing, affixed to the experimental setup, and aligned to a flat glass substrate. The actual experiments consisted of moving the samples along prescribed trajectories in order to study the contact interaction with the substrate. Motion trajectories were varied to study the adhesive characteristics of the synthetic patches. During the experiments, raw data was acquired using the software described previously and then analyzed using Matlab (The Mathworks, Inc.; Matlab R14).

3.3.1   Sample Preparation and Alignment

Before beginning each set of experiments samples were first cleaned by washing thoroughly with liquid soap and water, and then dried with compressed air. Samples were then exposed to a typical laboratory environment throughout experiments. This procedure was performed whenever samples were first mounted to the experimental setup and periodically thereafter (approximately every 5 days) if samples remained mounted for extended periods of time. Samples were fixed to either the force/torque sensor or the end-effector of the motion stage using thin double-sided tape.

Previous experimental investigations of fibrillar adhesives have usually involved tests with spherical substrates (e.g. glass hemispheres) in order to avoid alignment problems. In the present work a flat glass substrate was used and an alignment procedure is required to ensure the adhesive sample is properly aligned to the flat substrate. Alignment is performed via manual positioning of the stage and adjustment of the screws on the tilt platform. If the substrate is mounted to the force/torque sensor and the adhesive sample mounted to the end-effector of the motion stage alignment can be performed visually by inspecting the adhesive patch from the sides of experimental apparatus. This method can be used for alignment to non-transparent substrate.

When a glass substrate is used, the substrate is mounted to the motion stage

and the sample to the force/torque sensor. This configuration allows the user to see through the substrate and inspect the adhesive sample more clearly. The Alignment mode on the microcontroller is used to move the motion stage back and forth perpendicular to the contact normal while allowing the user to adjust the position along the contact normal. This allows visual inspection of all of the stalks on an adhesive sample and adjustment of the tilt stage such that all of the stalk tips make contact at roughly the same position in the normal direction. As the glass substrate moves back and forth perpendicular to the normal and is brought close to the sample, stalk tips begin to "catch" the surface, providing a clear indication of contact. The position coordinates are then set to zero at a point where the stalk tips are just off of the surface of the substrate.

3.3.2 General Procedure Description

After preparation and alignment of the sample, relative motion trajectories between the adhesive and the substrate are applied. In general, a specific trajectory first contains a dwell time, during which no motion takes place, that can be later used to accurately "tare" the measurements from the force/torque sensor. The next step is the preload phase in which the sample and substrate are brought into contact with each another. The amount of preload force applied between the two objects is dictated by the penetration depth into the fibrillar sample specified in this preload phase of the trajectory. Motions such as dragging can then be applied to the contact to study friction and/or adhesion, or a dwell time can be inserted into the trajectory. Finally, a typical trajectory pulls the sample away from the substrate until both objects are no longer in physical contact — the pulloff phase. In most cases, trajectories consist of a preload phase followed immediately by a pulloff phase.

Within this general framework many different parameters can be varied to study the adhesive samples. In particular, both the approach path during the preload phase and exit path during the pulloff phase were varied. In one-dimensional tests of synthetic adhesives, both the approach and exit paths are fixed along the contact normal. The speed of the trajectory was also varied.
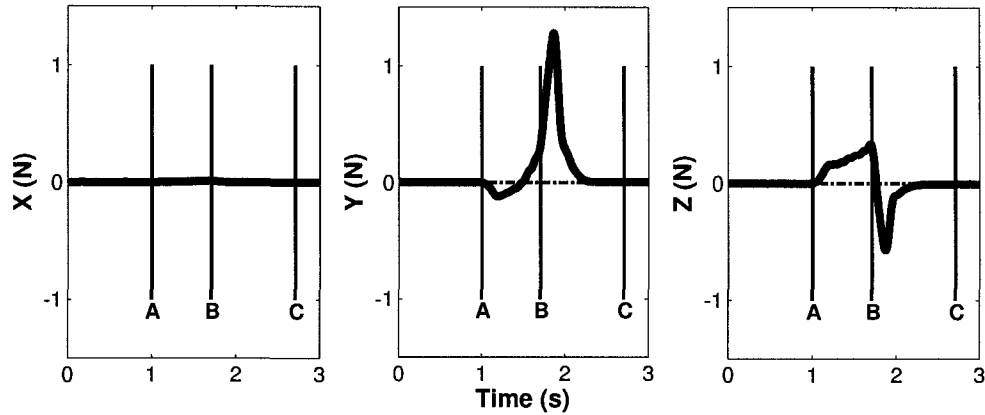
Figure 3.9: Typical force profile for a contact experiment. Contact experiment consists of preload phase (A-B) followed by a pulloff phase (B-C). Forces recorded are for the X, Y, and Z axes and have been filtered using a 3rd-order Butterworth filter with a cutoff frequency of 10Hz.

The primary goal of these experiments is to determine the contact failure point between the adhesive sample and substrate. Contact failure is here defined as the point at which the adhesive and substrate either separate from each other or slide against each other. The forces at these points can be used to construct an experimental limit surface similar to the ones described in Chapter 2. Determination of contact failure is done by analyzing the acquired data in Matlab.

3.3.3 Discussion of Raw Data

For each trajectory executed, the LabView software records a log file containing all the desired and actual position data for the motion stage and all the forces and torques sampled from the force/torque sensor as a function of time. This raw data is post-processed in Matlab to extract useful information about the contact experiment. Raw force/torque data is first tared using averaged data from the initial dwell time in a trajectory. Force and torque data is filtered using a 3rd-order Butterworth filter with a cutoff frequency of 10Hz. Throughout all experiments, moments were negligible since only linear motions were applied and the alignment procedure was fairly robust.

A typical filtered force profile for a contact experiment is shown in Figure 3.9. The

original trajectory is used to determine which sections of the force profiles correspond to particular phases of the trajectory. While the force profile contains a rich amount of information, problems arise when trying to extract specific quantities such as the maximum preload force or the maximum pulloff force. The maximum pulloff force is essentially an attempt to determine how much force can be applied to the contact before failure, and in this sense, is really a contact failure force. The contact failure can be somewhat complicated, but in general, it is characterized by a rise in the contact forces as stresses at the contact interface build up followed by a peak and rapid decline of the contact forces. However, specific failures may differ from this general behavior, and a precise definition for important specific quantities is not necessarily a straightforward matter.

In particular, consider the contact failure event. One choice for the failure event might be the time at which the normal force is maximally tensile between the two objects. But an alternative choice might simply be the time at which the magnitude of the net force vector is a maximum in the tensile half-plane of the contact. However, these definitions may be lacking when significant parallel forces are present along with normal forces. Recalling the discussion of limit surfaces and contact modeling (Section 2.1), it has been noted [44, 45] that in the case of Coulomb friction the instantaneous velocity at the contact is aligned with the instantaneous force at the contact (i.e. the friction force opposes the motion). This property has been termed the maximum power principle and can be used to define the failure point for simple friction and thereby the limit surface as well.

Because of the complex geometry of the DPS, the pulloff and/or sliding forces may not necessarily be aligned with the velocity of the sample. However, with a slight modification the underlying concept of the maximum power principle can still be applied. The contact failure event can be defined as the time at which the dot product between the relative velocity vector of the sample and substrate and the force vector at the contact interface is a minimum (negative because work is being done by the motion stage). Mathematically, the maximum adhesion method, the maximum magnitude method, and the maximum power method are given by:
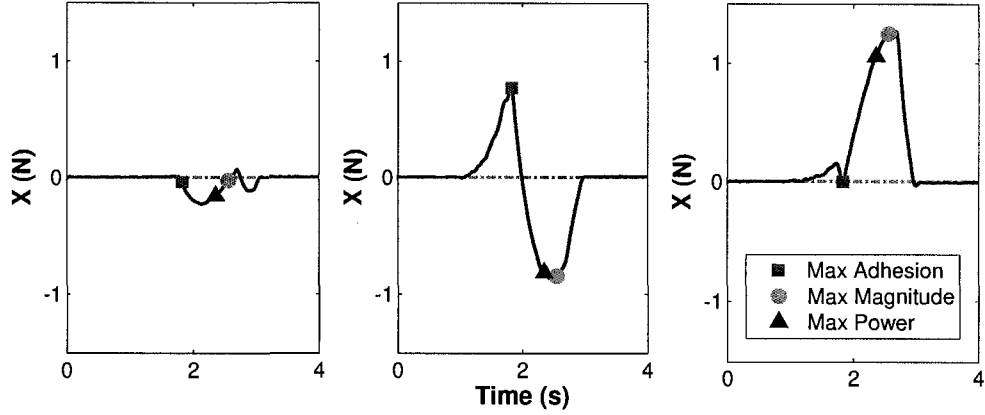
Figure 3.10: Parsing of a force profile from a contact experiment. Force profile is analyzed to extract important data points. In this example, three methods for extracting the contact failure force are compared. In the case of "Max Adhesion", the contact failure is defined as the time at which maximum adhesion is reached. For "Max Magnitude", the contact failure is defined as the time at which the force vector is a maximum in the tensile half-plane of the contact. Finally, "Max Power" corresponds to when the dot product between the force vector and the velocity vector is a minimum.

$$F_Z(t_{fail}) \leq F_Z(t), \forall t, \tag{3.1}$$

$$||\mathbf{F}(t_{fail})|| \, \mathrm{sgn}(F_Z(t_{fail})) \leq ||\mathbf{F}(t)|| \, \mathrm{sgn}(F_Z(t)), \forall t, \text{and} \tag{3.2}$$

$$\mathbf{F}(t_{fail}) \bullet \mathbf{v}(t_{fail}) \leq \mathbf{F}(t) \bullet \mathbf{v}(t), \forall t, \tag{3.3}$$

respectively, where t is time, t_{fail} is the contact failure time, $\mathbf{F}$ is the force vector, F_Z is the normal component of the force vector, and $\mathbf{v}$ is the relative velocity vector of the sample and substrate. An example of using these three different methods on actual data from a contact experiment is given in Figure 3.10.

The maximum power method tends to produce the best results over all of the different types of trajectories used. The maximum adhesion method fails when contact failure is primarily the result of sliding because in these cases there may be no adhesion

Directional Polymer Stalks
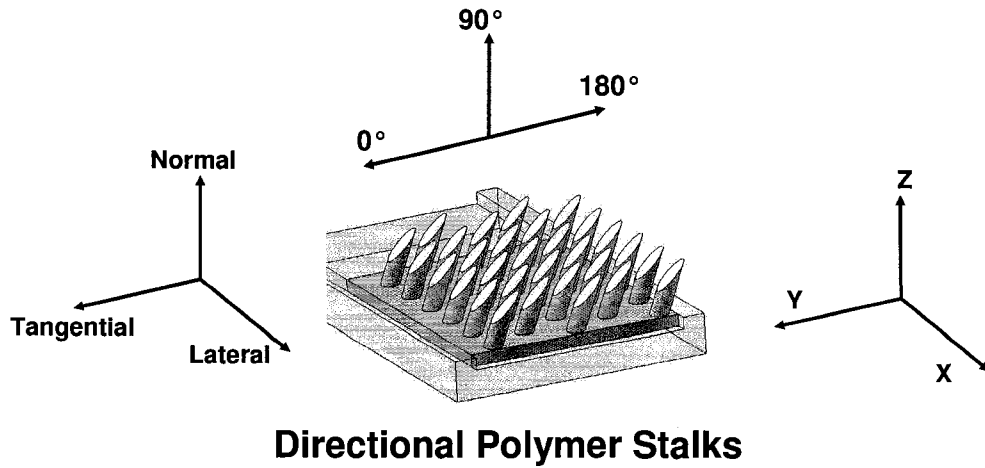
Figure 3.11: Coordinate frame naming convention for the DPS. Angles are used when discussing motions constrained to the YZ-plane.

present at the time of contact failure. The maximum magnitude method does not perform well when complicated failure events are involved. In these cases, the contact may have actually already failed but this method will select a later point in time when the stalks are buckling. The maximum power method produces good results because it takes into account the direction that the sample is being pulled in. It also inherently captures both sliding and pulloff failures using only one method. In general, the maximum power method was used to determine the contact failure event and the maximum pulloff forces; however, the results produced by both the maximum power and maximum adhesion methods will be discussed throughout the presentation of experimental results.

3.4   Adhesion Results

The primary goal of the experiments performed on the DPS patches was to determine their adhesive characteristics. Experiments were designed to study how different motion trajectories would affect the magnitude and direction of forces transmitted at the contact interface. Throughout the following discussion of various tests performed a standard coordinate frame will be used. Figure 3.11 shows the coordinate frame
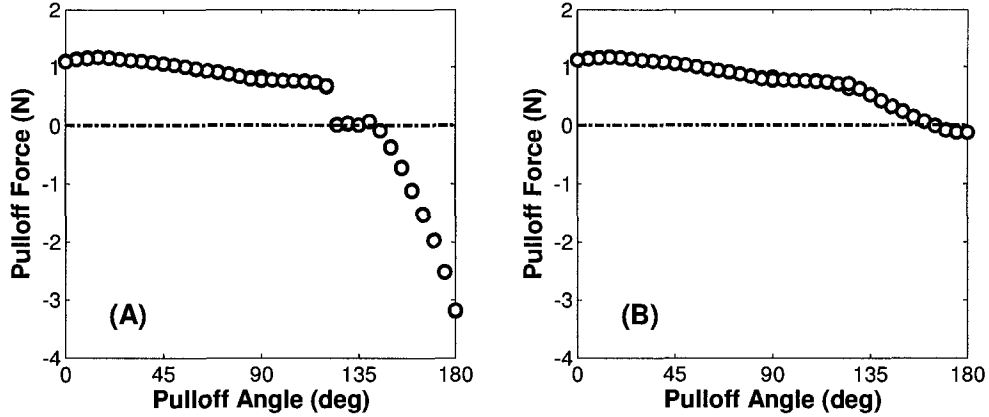
Figure 3.12: Normal pulloff force as a function of the pulloff angle. (A) Pulloff force determined by using the maximum power method. (B) Pulloff force determined by using the maximum adhesion method. Three trials were performed at each pulloff angle. Preload depth was constant across all trials at 500μm. Maximum adhesion is achieved at an exit angle of $0°$ with a steady drop in adhesion as the exit angle is increased toward $180°$.

in relation to the geometry of the DPS along with angles corresponding to angles of approach and retraction used in the preload and pulloff phases of some trajectories.

3.4.1 Adhesive Pulloff Forces

The first tests performed were simple motion trajectories that involved only motions in the YZ-plane. In these experiments the sample patch was brought into contact with the substrate along a $45°$ approach angle. This angle was chosen so the stalk faces of the DPS would make good contact with the substrate. The DPS were preloaded against the substrate along this approach angle to a controlled penetration depth between 0μm and 900μm. The patches were then pulled away from the substrate along a straight line path in the YZ-plane. The speed of the trajectory was held constant across all tests at 1mm/s. The exit angle was varied between $0°$ and $180°$ (Figure 3.11).

Figure 3.12 shows some results from these experiments. Two different methods for determining pulloff force are shown — the maximum power and maximum adhesion

method. Both methods show the same general trend. Adhesion is maximized at small pulloff angles and decreases steadily as the pulloff angle is increased toward 180°. The small pulloff angles correspond to when the DPS are pulled with the angle of their stalks (Figure 3.11). The existence of negative "pulloff" forces (corresponding to a compressive force at pulloff) requires some explanation. At very shallow angles (close to 0° or 180°) it may be possible for the DPS to begin sliding along the substrate before physical separation occurs. In these instances the stalk faces may break contact with the substrate with a primarily shear force and no adhesion may actually be present. The maximum power method picks the point of maximum shear as the pulloff event. The maximum adhesion method always picks the largest pulloff force over the entire pulloff phase of the trajectory, but this may still be a negative pulloff force corresponding to when no adhesion is exhibited at any point during the experiment.

The two different methods do produce slightly different results. In these and most experiments performed, the DPS are preloaded along a 45° approach that brings the angled stalk faces into good contact with the substrate. In this preloaded state the DPS are essentially bent to one side. As the pulloff angle increases the DPS will at some point buckle and the stalks will bend the other way, contacting the substrate along the cylinder side rather than the side with the angled face. As mentioned previously, this buckling event can become problematic when attempting to determine pulloff forces.

In Figure 3.12 the two methods for determining maximum pulloff force agree well for pulloff angles between 0° and 90°. This range of pulloff angles does not produce buckling of the stalks. Simply, the stalks are stretched along their centerline axes until they eventually separate from the substrate. The two methods produce different results when the stalks begin to buckle. Upon close inspection of the raw data, the maximum adhesion method tends to favor the time of the buckling event for the determination of pulloff force, and the maximum power method tends to favor a time *after* the buckling event that corresponds to physical separation or relative sliding. During the buckling event, the macroscopic behavior of the DPS can be considered static in nature because the stalks remain in contact with the substrate as their bending orientation flips.

Nevertheless, both methods clearly demonstrate how the adhesion force is strongly dependent on the pulloff angle. These experiments are the first evidence that the DPS do indeed exhibit directional adhesion. Using both methods, adhesion is a maximized at shallow pulloff angles when the DPS are pulled with their stalk angles. As pulloff angle increases (becoming a purely normal exit vector at 90°) adhesion steadily drops, and, while both methods differ in the details, at pulloff angles above 90° adhesion vanishes completely.

3.4.2   Effect of Preload Magnitude

As stated earlier, throughout all experiments the magnitude of the preload force was controlled indirectly by specifying the amount of preload penetration depth into the DPS. The results shown in Figure 3.12 were for a single preload penetration depth; however, the same experiments were performed for a large range of penetration depths. Figure 3.13 shows how pulloff forces are also dependent on the amount of preload in addition to the pulloff angle. The data in Figure 3.13 is for the pulloff forces as both a function of the applied penetration depth and the actual preload force. The preload forces were calculated by averaging the maximum preload recorded for each experiment at a given preload depth.

Both plots in Figure 3.13 exhibit the same general behavior. Pulloff force increases as preload force increases up until a saturation point is reached. Looking specifically at preload depth, at first the pulloff force increases only modestly with increasing preload depth. At a preload of about 400μm the pulloff force begins to increase more rapidly with each increase in preload depth. However, at a preload of about 700μm the pulloff force begins to saturate. Looking at preload force, a slightly simpler behavior exists. The pulloff force increases roughly linearly with the preload force up until a saturation point at around 1N.

The maximum pulloff forces in Figure 3.13 were determined using the maximum power method in all cases; however, the pulloff angle that produced the maximum pulloff force varied for each preload depth. The results shown are always for the pulloff angle that produced the maximum pulloff force. For small preloads the maximum
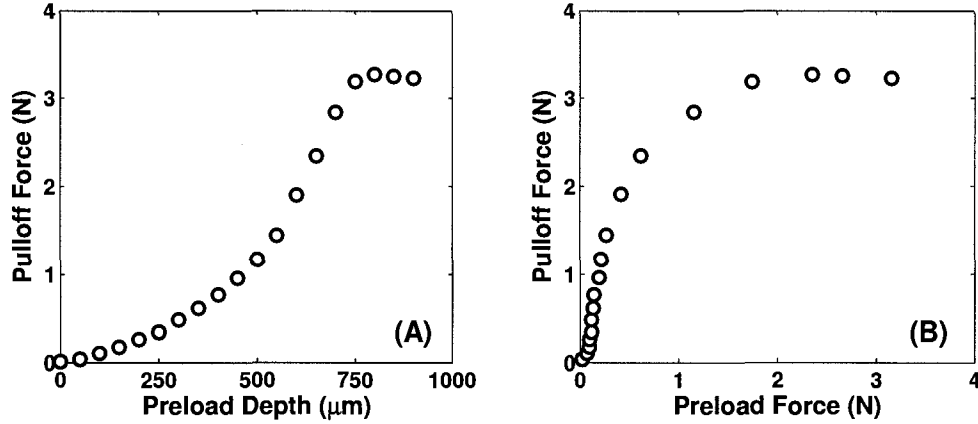
Figure 3.13: Normal pulloff force as a function of preload penetration depth. Preload depth was varied between 0μm and 900μm. Maximum pulloff force is determined using maximum power method over all pulloff angles. (A) Maximum pulloff force at different preload depths. (B) Maximum pulloff force at different preload forces.

pulloff force was produced with pulloff angles near $0°$, but for the larger preloads the best pulloff angles increased to as much as $45°$.

The difference between the two plots in Figure 3.13 is because there is a non-linear relationship between preload depth and preload force. The DPS do not exhibit a simple single-valued Modulus of Elasticity. The elastic modulus of the bulk material used to make the DPS is ≈ 300kPa but the effective stiffness of the DPS is much lower. The relationship between the preload depth in the normal direction (along a $45°$ trajectory) and the preload force in the normal direction is shown in Figure 3.14. At each preload depth, about 100 trials were performed (3 trials at each pulloff angle ranging from $0°$ to $180°$ in $5°$ increments) and the average preload force is given along with error bars corresponding to one standard deviation above and below the mean.

Figure 3.14 basically shows the force-displacement relationship for the DPS when loaded along a $45°$ angle. For an ideal elastic solid undergoing small displacements the force-displacement relationship is a straight line. The data shows two roughly linear regions, one at penetrations less than 500μm and one at penetrations greater than 500μm. Linear fits to these two sections result in a stiffness of 0.4N/m and 10.9N/m for the shallow and steep regions, respectively. The smaller stiffness corresponds
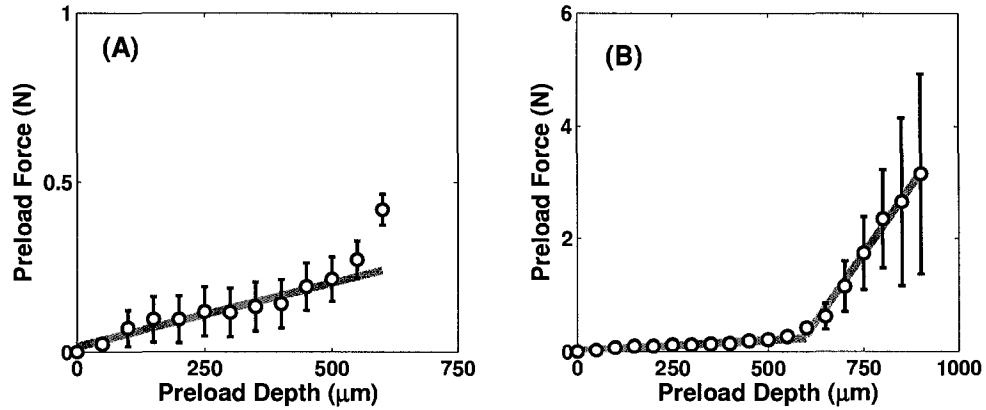
Figure 3.14: Relationship between preload depth along a 45° approach angle and average preload force. Preload depth was varied between 0μm and 900μm. Preload force was averaged over many trials and is shown with error bars corresponding to one standard deviation in either direction. (A) Subset of all data for preload depths from 0μm to 600μm. (B) Full data set with preload depths from 0μm to 900μm.

to when only the stalk tips are making contact with the substrate. As penetration depth increases, the entire stalk face makes contact and the entire stalk is in bending, resulting in a higher overall stiffness. The higher stiffness corresponds to an equivalent Modulus of Elasticity of about 27kPa. Due to the microstructured geometry of the DPS the effective stiffness is over an order of magnitude lower than that of the bulk polyurethane (E ≈ 300kPa).

3.4.3 Effect of Preload Trajectory

The previous section explored the effect of preload on the pulloff and adhesion characteristics of the DPS. Throughout those experiments the approach angle was held constant at 45°. This section will look at results obtained from varying the preload angle between 5° and 175° in 5° increments. The preload depth was varied between 400μm and 700μm, found earlier to provide reasonable amounts of adhesion and avoid saturation effects. The pulloff angle was held constant at 30°, also determined from previous experiments to produce good adhesion over the range of preloads tested.

Figure 3.15 shows the amount of normal preload force over the range of preload

Figure 3.15: Preload force in the normal axis as a function of preload angle. Data is shown for preload depths in the normal direction of 400μm and 600μm. Preload angle was varied from 5° to 175° in 5° increments. (A) Preload force determined using a maximum compressive force method. (B) Preload force determined using a maximum vector force method.

trajectories tested. Only two preload depths are shown (400μm and 600μm), although results are similar for the other preload depths tested. Results have been averaged over 3 trials for each combination of preload depth and trajectory.

Two plots are shown, each corresponding to a different method for determining the actual maximum preload force observed in the experiment. Similar to the determination of pulloff forces, preload forces are determined via either a maximum compressive force method or a maximum vector force method. Using the maximum compressive method the preload force is simply the maximum compressive force in the normal direction during the preload phase. Using the maximum vector method the preload force is the maximum force vector along the preload trajectory during the preload phase. The maximum vector method tends to produce better results than the maximum compressive method. In some instances the maximum compressive method determines that failure occurs at the earliest point during the preload phase even though the sample may only be barely touching the substrate. The maximum vector method is able to account for both normal and tangential (shear) preload effects, although only the normal preload component is shown in the figure.

The difference between the two methods occurs at very shallow angles (0° or

180°) particularly when approaching with the stalk angle. In these cases, the maximum compressive method determines that there is zero applied normal preload force, whereas the maximum vector method determines that there is a *negative* normal preload. Upon close inspection of the raw data, there is no measurable compressive force throughout the entire preload phase in these cases. The normal force starts at zero and decreases (negative normal force is adhesion) slowly and steadily during the preload phase and then decreases very rapidly and peaks during the pulloff phase. The maximum compressive method determines that the maximum preload force actually occurs at the *beginning* of the preload phase. Because of the DPS geometry, at shallow angles the stalk tips make initial contact and stick with negligible compressive force and then immediately switch to a tensile mode. As the preload phase continues, individual tips will break and remake contact (each time with a larger contact area as the depth increases), but the overall force remains adhesive in nature.

This effect is macroscopically similar to the gecko adhesive system although the specific details may differ. The gecko adhesive system requires very little attachment forces in order to stick. The DPS, under the proper circumstances, do not actually require a compressive attachment force to stick. In truth, some initial compressive force must be present but it is less than the resolution of the experimental setup used for these tests and is essentially negligible when compared to the adhesive forces generated.

Figure 3.16 shows the pulloff forces generated for the different preload trajectories tested. As before, preload depths between 400μm and 700μm were tested although only two depths are shown, and each data point is the average of 3 trials for a combination of preload trajectory and depth. All pulloff forces are determined by using the maximum power method described earlier (Section 3.3.3).

The data clearly show the difference that preload approach trajectory has on the maximum adhesive pulloff forces achieved. The same trend is seen across different preload depths, namely that pulloff force is maximized around a preload trajectory of about 45°. As preload trajectory increases above 45° pulloff force decreases steadily, becoming roughly zero above 135°. At angles between 45° and 135° the DPS approach the substrate along a close-to-normal path. While the DPS are slightly angled, this
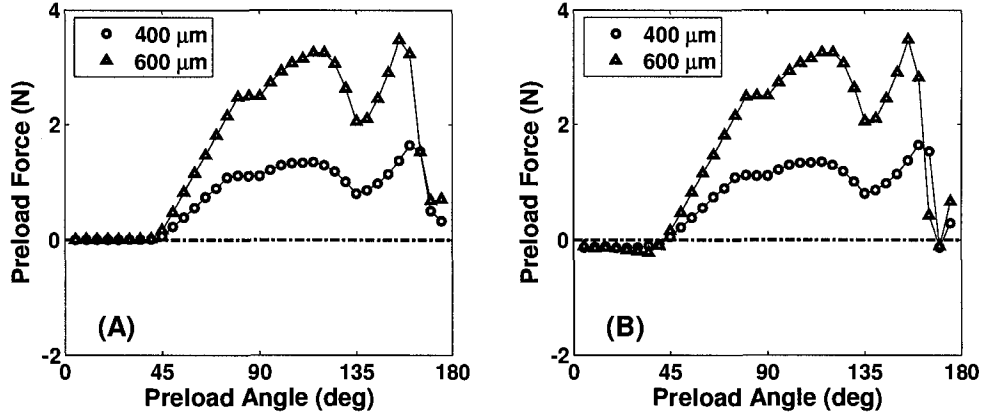
Figure 3.16: Pulloff force in the normal axis as a function of preload angle. Data is shown for preload depths in the normal direction of 400μm and 600μm. Preload trajectory was varied from 5° to 175° in 5° increments.

will still tend to cause stalk buckling, and stalk faces do not make good contact with the substrate. At even larger approach angles, the DPS actually bend against their stalk angle and contact the substrate with the backside of their stalks instead of with their stalk faces. When this happens very little real contact area is generated (line contact resulting from a cylinder on a flat), and hence very little adhesion is present.

Adhesion also drops as the approach angle decreases below 45°. This is related to the same behavior described above to explain negative preload forces at shallow approach angles. At these shallow angles individual stalks start to break and remake contact multiple times throughout the preload phase. Each time a stalk breaks and makes contact relieves some of the normal compressive preload force acting on that stalk. At the end of the preload phase some stalks may be in good contact but others

may either have just experienced or be about to experience a break-make event. While this does not eliminate the adhesive forces that can be sustained it does act to reduce them significantly from their maximum value at an approach angle of about 45°.

The results given in Figures 3.15 and 3.16 provide a good picture of the effects of approach trajectory. To minimize the normal preload force required, the approach angle should be less than about 45° according to the data shown in Figure 3.15. In this regime the preload forces will either be close to zero or actually negative (corresponding to adhesion during the preload phase). However, taking into account the data in Figure 3.16 further restricts the desired approach angle. The pulloff data clearly shows maximum pulloff forces are achieved at approach trajectories of about 45°. Taken together, the optimal approach preload trajectory for the DPS, in order to minimize preload force and maximize pulloff force, is approximately 45°.

3.4.4 Rate Dependence of Adhesion

Throughout the previous experiments and results presented, the speed of the DPS relative to the substrate was held constant at 1mm/s. In the Kendall peel model presented in Chapter 2, the adhesion energy (R) is dependent on the peeling rate of the thin film [63]. Other research has also explored the effects of pulloff rate on pulloff forces [31]. The rate dependence of adhesion may be the result of viscoelastic effects in the two contacting objects or other time-dependent aspects of intermolecular forces [64]. Adhesion forces tend to increase as the rate of separation increases although the exact details of this relationship are usually only obtained experimentally.

Experiments were thus performed to determine how different pulloff rates affect the adhesion characteristics of the DPS. The trajectory speed was varied from 0.01mm/s to 10mm/s but kept constant within a trajectory (i.e. the same for both preload and pulloff phases). The approach angle was fixed at 45° and the pulloff angle was fixed at 30° for all trajectories based on results from previous experiments. Preload depth was varied between 400μm and 700μm. Maximum pulloff forces were determined by using the maximum power method.

Figure 3.17 shows the results of these experiments. The data show that adhesive
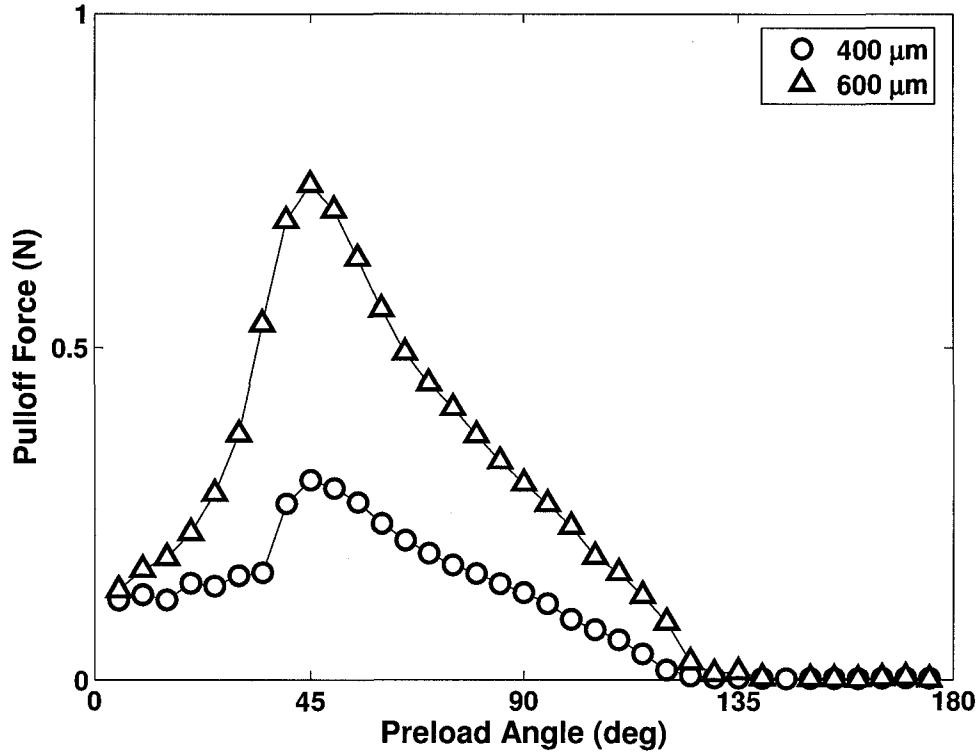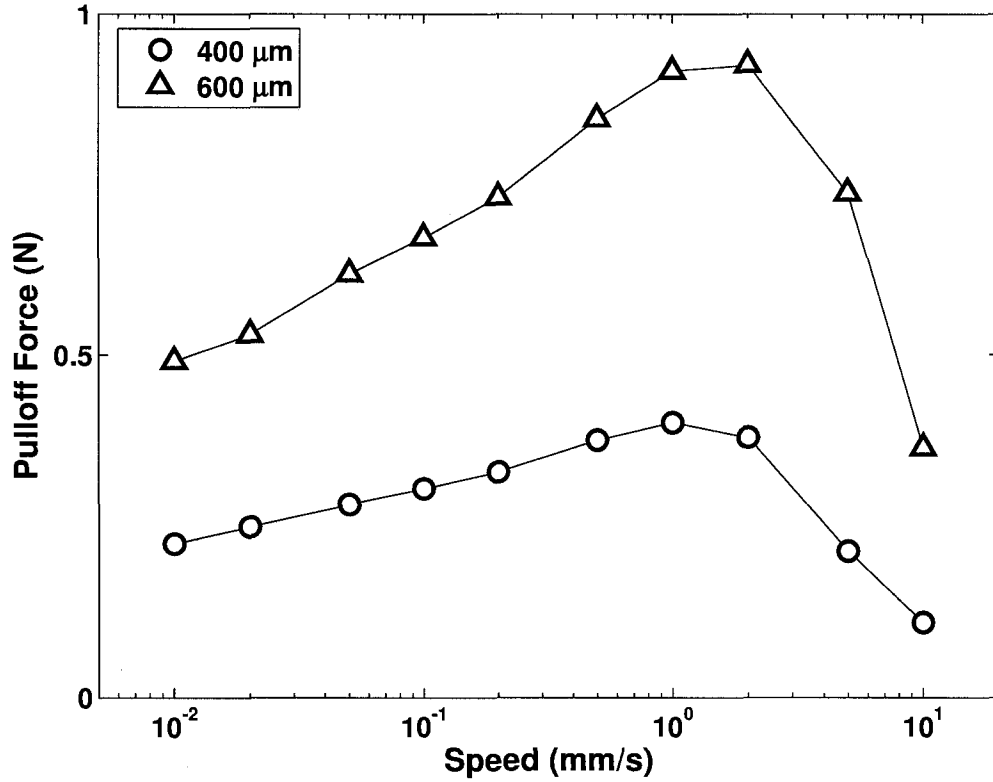
Figure 3.17: Pulloff force in the normal axis as a function of speed of separation. Data is shown for preload depths in the normal direction of 400μm and 600μm. Trajectory speed was varied between 0.01mm/s and 10mm/s. Speed is plotted on a logarithmic scale to show trends more clearly.

forces do indeed decrease as speed decreases from 1mm/s to 0.01mm/s and agree with previous work studying the effects of rate. It seems that pulloff forces will continue decreasing as speed decreases, tending toward zero as the speed also becomes zero; however, there may exist some finite (but small) minimum force required for detachment regardless of how small the separation rate is. If this minimum does exist then it essentially defines the maximum force that can be applied while maintaining indefinite adhesion. Any forces above this limit would cause the materials to eventually separate, however slowly.

While the results agree with previous theoretical and experimental analyses in the range of 0.01mm/s to 1mm/s, they show a very different trend for speeds greater

than 1mm/s. The pulloff force decreases as the speed is increased above 1mm/s instead of increasing as is expected. This is potentially the result of a limitation in the experimental setup and a parameter in the trajectories used for this experiment. The experimental setup has a maximum upper speed limit of about 5mm/s. Detailed inspection of raw data at speeds of 10mm/s reveals that the positioning stage cannot accurately track the desired position. This results in preloads less than those prescribed by the trajectory. Second, the speed of the pulloff phase was the same as the speed of the preload phase. Due to the viscoelastic nature of the DPS the preload phase may not provide sufficient settling time for the DPS to fully develop adhesive bonds to the substrate at high speeds. These two combined effects may lead to decreased adhesion as speed increases above 1mm/s. Both these aspects can be eliminated by modifications to the setup and procedure and are an area for future work.

3.4.5 Coefficient and Work of Adhesion

Two common parameters used for quantifying adhesives, after the maximum pulloff force, are the Coefficient of Adhesion (μ') and the Work of Adhesion (W_{adh}). These standard parameters allow comparison between different natural and synthetic adhesives. The Coefficient of Adhesion is the ratio of the maximum pulloff force in the normal direction to the maximum preload force in the normal direction [19]. This definition is fairly simple to apply when performing adhesion experiments in only the normal direction but becomes slightly more complicated when looking at adhesion in different directions.

Figure 3.18 shows the Coefficient of Adhesion for the DPS at different pulloff angles. In these experiments the approach angle was constant at 45°, speed was constant at $1mm/s°$, and preload depth was varied from 400μm to 700μm. Pulloff angles were varied from 0° to 180° in 5° increments. Each point is the average μ' for 3 trials at the same pulloff angle and preload depth. The pulloff force used to calculate μ' can be determined using different methods. Figure 3.18 shows results when using both the maximum power method and the maximum adhesion method.

Figure 3.18: Coefficient of Adhesion as a function of pulloff angle. Data is shown for preload depths in the normal direction of 400μm and 600μm. (A) Pulloff force determined using maximum power method. (B) Pulloff force determined using maximum adhesion method.

As in Section 3.4.1 both methods produce similar results at low pulloff angles. At high pulloff angles (greater than 90°) the results begin to differ. The maximum adhesion method produces higher values of μ' because it also produces higher values of pulloff force (Section 3.4.1). Because these tests are not simply testing adhesion in the normal direction the calculation of μ' becomes complicated. While the conventional definition of μ' calls for using the maximum adhesive force during pulloff, it is not necessarily clear what pulloff force should be used here. The maximum power method perhaps more accurately produces a pulloff force corresponding to contact failure. In either case the results are qualitatively similar and produce negative values for μ' caused by negative values for the pulloff force.

The data also show that preload depth has little affect on μ'. Looking back at Figure 3.13, for the range of preload depths used here the pulloff force increases roughly linearly with preload depth. As such the Coefficient of Adhesion should indeed be roughly constant across the preload depths shown.

Preload trajectory also affects the Coefficient of Adhesion. Figure 3.19 shows μ' as a function of the approach angle during the preload phase. Data was gathered from experiments outlined in Section 3.4.3 and is shown for preloads of 400μm and 600μm. Again, two different methods are used for calculating μ'. In this case, since

Figure 3.19: Coefficient of Adhesion as a function of preload angle. Data is shown for preload depths in the normal direction of 400μm and 600μm. (A) Maximum vector method used for determining preload force. (B) Maximum compressive method used for determining preload force.

pulloff angle was held constant at 30°, both the maximum power method and the maximum adhesion method produce the same pulloff forces. The difference between the plots shown in (A) and (B) stems from the determination of preload force.

As discussed in Section 3.4.3, the preload can also be determined via two different methods — the maximum compressive method or the maximum vector method. At very small approach angles (shallow angles aligned with the stalk angle), the preload phase of the trajectory produces negligible compressive preload forces. Because the angle is so shallow, as soon as the DPS tips touch the substrate they almost immediately begin to stretch and produce adhesive forces. The maximum compressive method chooses the beginning of the preload phase for the maximum preload because adhesion and not compression exists from the beginning of the preload phase onward. The maximum vector method chooses the end of the preload phase because the shear forces are highest; however, the normal forces end up adhesive rather than compressive using this method.

Thus, at small angles, Figure 3.19 (A) shows negative values for μ'. This is due to negative values for the preload force (i.e. adhesive preload). In Figure 3.19 (B) values for μ' are very large and noisy at small approach angles. When using the maximum compressive method, the preload force is a very small positive number dominated

by noise because the compressive forces are very small. Here, as opposed to Figure 3.18, negative values for μ' are caused by negative values for preload force instead of negative values for pulloff force. It is clear that negative values for μ' in Figure 3.19 (A) essentially correspond to very high positive values of μ' since the preload force is negligible in a compressive sense.

Using the maximum vector method to calculate preload force can produce ambiguous negative values for μ' since it is unclear whether it is the preload force that is adhesive or the pulloff force that is compressive. However, using the maximum compressive method is also problematic due to noise dominance when preload forces are small and/or adhesive throughout the preload phase. Both of these issues make interpretation of the Coefficient of Adhesion less straightforward than when testing in the purely normal direction. Nevertheless, μ' can be a useful metric when taken in the proper context and interpreted correctly. In the present case, the DPS show a very promising relationship between pulloff forces and preload forces at approach angles less than $45°$. At these approach angles pulloff forces can be quite large compared to the compressive preload force required.

The other common adhesive metric introduced earlier is the Work of Adhesion (W_{adh}) — the work loop performed from the initiation of physical contact to the final separation of the two objects in contact [31]. For a purely elastic contact with no adhesion (e.g. Hertzian contact) the work loop is zero. Work is done to press the two objects together, energy being stored in the strain of each object, and then work is recovered when the compressive force is eliminated and the strain energy is released. However, in reality there always exists some hysteresis in this cycle. If the objects lack adhesion, energy may be dissipated in the materials themselves because they are not ideally elastic. When adhesion is also present there will be energy lost in the process of making and breaking adhesive bonds. The Work of Adhesion can be calculated from the raw data by summing (i.e. integration in discrete time) the dot product between the force vector and the displacement vector at each point in the sampled data stream.

Figure 3.20 shows W_{adh} for different pulloff angles. Data was gathered from experiments described earlier for calculation of μ' for different pulloff angles. Like μ',
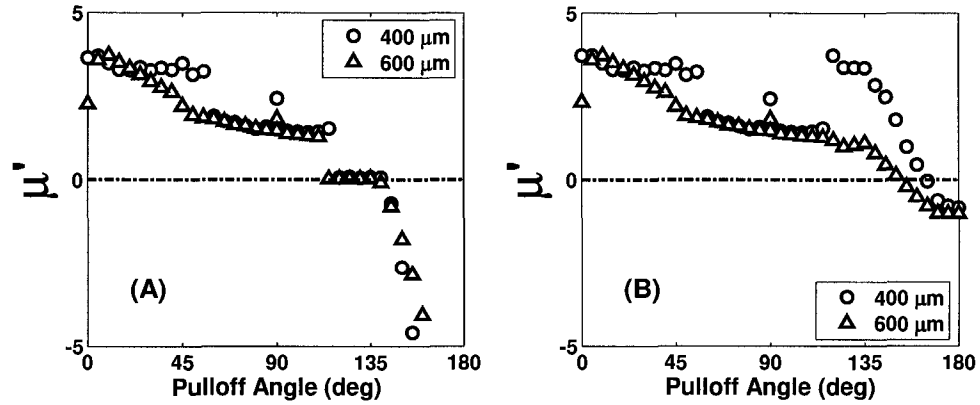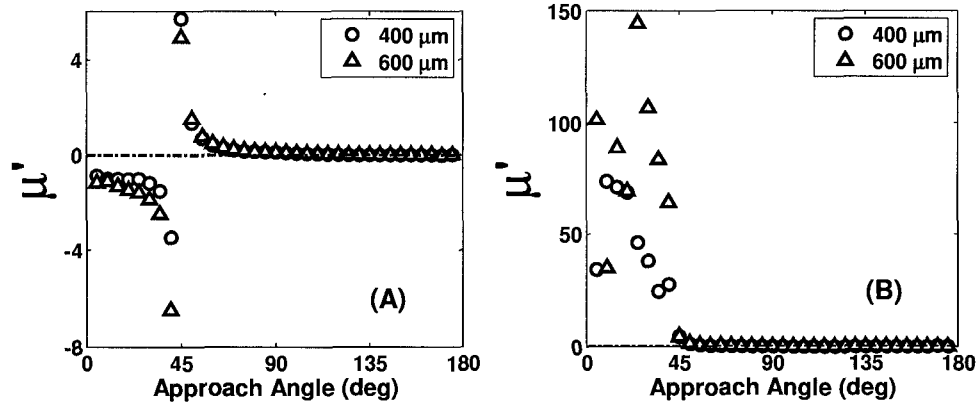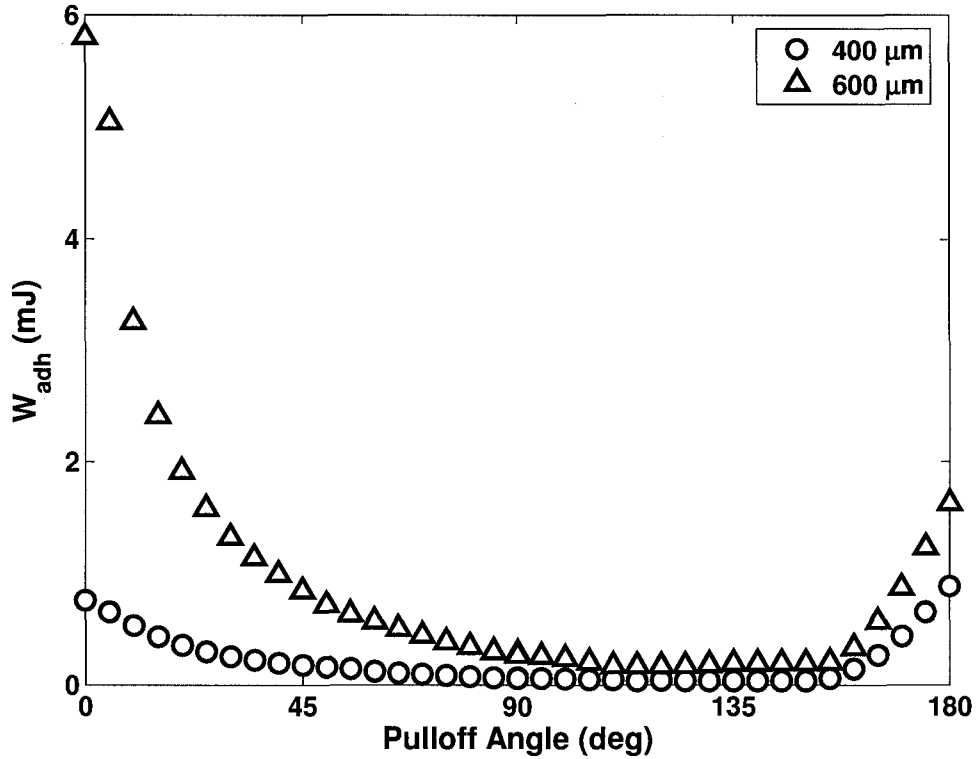
Figure 3.20: Work of Adhesion as a function of pulloff angle. Data is shown for preload depths in the normal direction of 400μm and 600μm.

W_{adh} is strongly dependent on the pulloff angle. Not surprisingly it is maximized when pulling the DPS at shallow angles in the adhesive direction. It is minimized at pulloff angles around 135° and then increases again at shallow angles in the opposite direction of the stalk and face angles of the DPS. This increase at pulloff angles approaching 180° is due to energy dissipated during buckling events and shear strains generated before sliding begins.

Of particular importance in Figure 3.20 is the difference between the maximum work achieved at around 0°, and the minimum work achieved at around 135°. For a preload depth of 600μm the maximum Work of Adhesion is approximately 6.7mJ, over 40 times larger than the minimum Work of Adhesion. In practical terms this means that the energy required to attach and detach the DPS is very controllable.

Figure 3.21 shows the effect of pulloff speed on W_{adh}. Data was gathered from
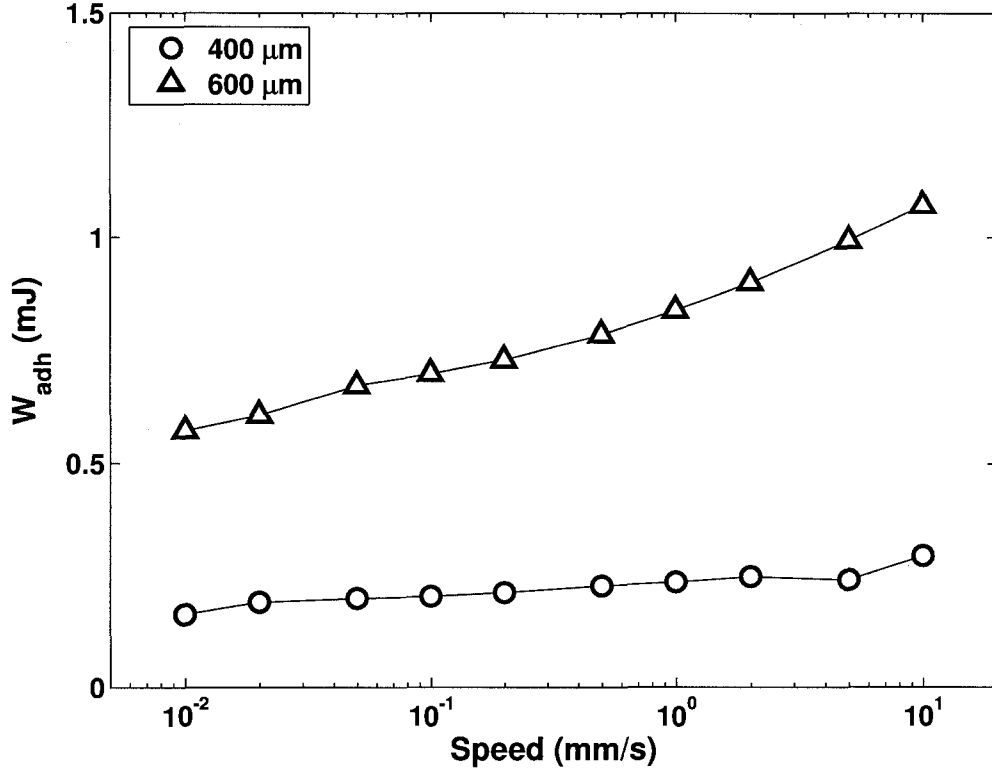
Figure 3.21: Work of Adhesion as a function of pulloff speed. Data is shown for preload depths in the normal direction of 400μm and 600μm.

experiments described earlier in Section 3.4.4. Throughout all experiments, approach angle was fixed at $45°$ and pulloff angle was fixed at $30°$. The energy required to detach the DPS increases monotonically with increasing speed. As the speed of pulloff increases, any losses due to viscous damping increase, and hence the overall Work of Adhesion increases.

The Work of Adhesion is a valuable metric for assessing the usefulness of an adhesive. It is a quantitative measure of the amount of energy required to perform one attach/detach cycle. For a climbing robot this information is necessary for calculating the energy and power needs for climbing at a given speed. The controllability of the DPS allows the Work of Adhesion to be minimized when easy detachment is desired and maximized when strong attachment is desired. This characteristic is essential for

climbing efficiently. Adhesives that have a constant-valued W_{adh} would place much larger energy requirements on a climbing robot. The DPS provide a way to reduce the energy requirements simply by applying the proper motion trajectories during detachment phases.

3.4.6 2D and 3D Directional Adhesion Limit Surface

The previous sections explored various relationships between pulloff forces and angles, preload forces and angles, and pulloff and preload speeds. The results shown provide direct correlations between such things as the amount of adhesion that can be generated and the motion trajectory applied to the DPS. Section 3.4.1 shows that the DPS are directional. Sections 3.4.1, 3.4.2, and 3.4.3 show how the motion trajectory and amount of preload applied to the DPS can control the adhesion. Rate also plays an important role in adhesion (Section 3.4.4) and Section 3.4.5 looks at some common metrics used when analyzing adhesives.

While the above information is crucial to understanding the adhesive characteristics of the DPS, and similarly any adhesive, one of the goals of experimental testing is to generate a description of the DPS similar to those given in Chapter 2 for various adhesive contact models. Essentially, it is desirable to look at the DPS from a limit surface perspective. This provides a concise description of the contact characteristics of the DPS and more importantly allows direct comparison of the DPS to the various adhesive contact models given in Chapter 2. To develop such a picture of the DPS it is necessary to look at the contact failure forces in force-space.

Figure 3.22 shows the contact forces at contact failure in both the tangential and normal directions. The data shown is generated from the experiments described in Section 3.4.1. Approach angle was held constant at 45° and speed was held constant at 1mm/s while preload depth and pulloff angle were varied. Failure forces were determined by using the maximum power method. Pulloff angles near 0° correspond to the adhesive data at the far right of the figure while pulloff angles near 180° correspond to the friction data at the far left. Two different preload depths show how the amount of preload determines the maximum amount of adhesion that can
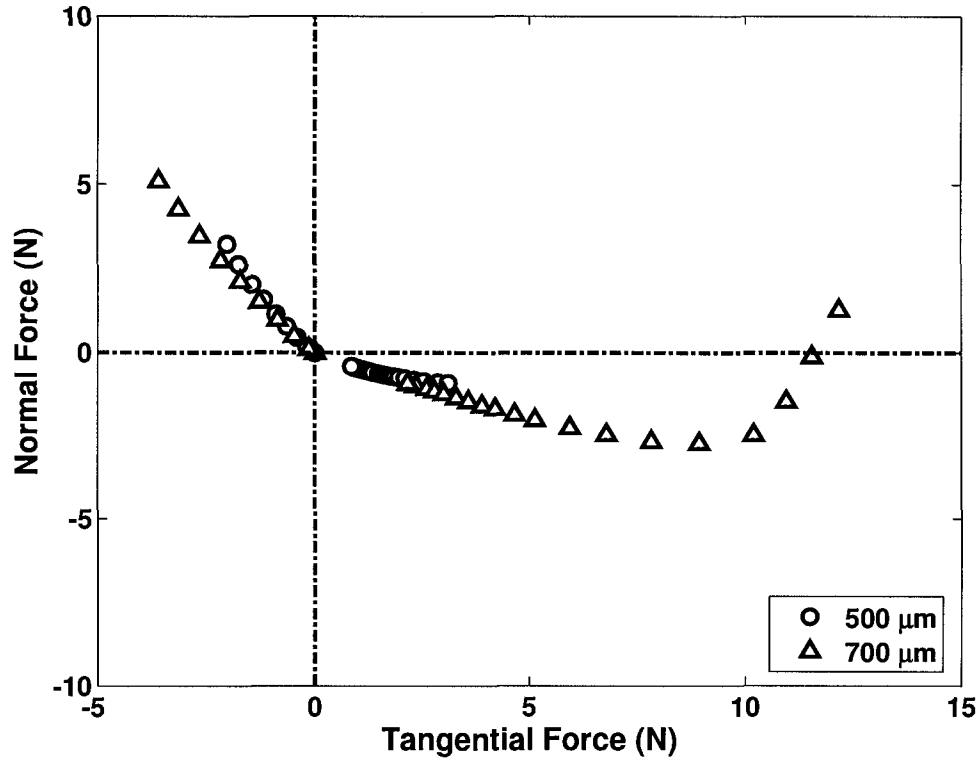
Figure 3.22: Contact failure forces of the DPS plotted in force-space in the YZ-plane. Data is shown for preload depths in the normal direction of 500μm and 700μm. Data was generated using pulloff angles between 0° and 90°. Each data point is an average of three trials.

be generated; however, within a given preload depth, the motion trajectory can be used to achieve the maximum adhesion or simply pull away from the substrate with negligible adhesive forces.

Figure 3.22 only shows a subset of the full range of pulloff angles tested. The DPS were also pulled "into" the surface at angles less than 0° and greater than 180°. While these pulloff angles do not necessarily cause pulloff of the DPS from the substrate they nevertheless cause contact failure, which can be determined via the maximum power method. When pulling parallel to the surface (0°), although the DPS are not technically pulled away from the surface, the failure point still exhibits an adhesive force caused by the angled geometry of the stalks. As the pulloff angle is further

Figure 3.23: Contact failure forces of the DPS plotted in force-space in the YZ-plane. Data is shown for preload depths in the normal direction of 500μm and 700μm. Data was generated using pulloff angles between $-30°$ and $120°$. Each data point is an average of three trials.

reduced and the DPS are pushed into the surface, the amount of adhesion at failure begins to decrease and eventually positive normal forces (compressive) are seen at failure. Figure 3.23 shows the full set of pulloff angles tested.

The data in Figures 3.22 and 3.23 provide an experimental limit surface for the DPS. The data represent the contact forces at the time of contact failure, precisely the definition of the limit surface given in Chapter 2. With this data the behavior of the DPS can be compared to the adhesive contact models described earlier. The three main adhesive contact models described in Chapter 2 are the JKR model, the Kendall peel model, and the Frictional Adhesion model for the gecko. The DPS clearly violate one of the main characteristics of the JKR model — symmetry. Only
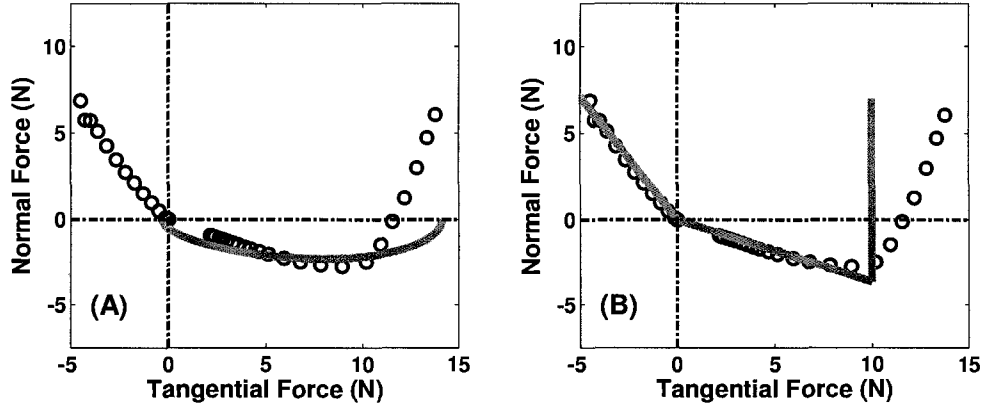
Figure 3.24: Comparison between two adhesive contact models and the experimental data gathered for the DPS. (A) Fit of the Kendall peel model to the DPS data. (B) Fit of the Frictional Adhesion model to the DPS data. DPS data represents contact failure forces for a preload depth of 700μm. Model parameters were tuned by hand to compare qualitatively how each model is able to capture the characteristics of the DPS.

the Kendall peel model and the Frictional Adhesion model exhibit directionality and might appropriately capture the DPS behavior.

For those two models parameters can be chosen to fit each model to the data gathered for the DPS. Figure 3.24 shows the contact failure data gathered at a preload depth of 700μm along with model fits for both the Kendall peel model and the Frictional Adhesion model. Both models capture the directionality of the DPS, exhibiting adhesion in only one direction along the tangential axis; however, neither model seems to capture all of the DPS characteristics.

The Kendall peel model is not well defined for positive normal forces (compression) and is therefore not able to capture the frictional behavior of the DPS in the non-adhesive direction. And while, like the DPS, adhesion first increases with increasing tangential force and then decreases with further increases in tangential force, the details of that relationship do not match well. The Kendall peel model describes a thin elastic tape being peeled from a substrate but the DPS patches are pulled away from the substrate uniformly as a bulk process. However, individual stalks may be peeling from the surface in a manner similar to that described by the Kendall peel

model. For this reason the Kendall peel model may be somewhat applicable and is able to describe some of the characteristics of the DPS. Indeed, at lower preload depths (500μm, 400μm, etc.) the data gathered from the DPS tend to match the Kendall peel model even more so than at 700μm.

The Frictional Adhesion model has the same frictional behavior as the DPS in the non-adhesive direction. In the adhesive direction, the DPS first exhibit increasing adhesion with increasing tangential force in a relationship that is roughly linear. Such a linear coupling between adhesion and shear is precisely given by the Frictional Adhesion model, and the agreement between this model and the data is clearly seen in Figure 3.24 (B). The Frictional Adhesion model imposes an upper limit on the tangential force sustainable before failure. At high tangential forces the DPS differ from the behavior predicted by the model. Rather than a sharp limit the adhesion of the DPS saturates and then decreases with increasing shear. Recall that the shear limit in the Frictional Adhesion model was chosen rather arbitrarily due to lack of data for the gecko adhesion system at these levels of shear force (Section 2.5). While the model and data differ, the model provides a conservative prediction of the forces that can be sustained.

It may be that the DPS patches behave somewhere in between the ideal Kendall peel model and the ideal Frictional Adhesion model; however, the data for the DPS tend to agree better with the predictions given by the Frictional Adhesion model. Given the fit between the Frictional Adhesion model and the data gathered for the DPS it is fair to say that the DPS capture the three characteristics of the gecko adhesive system important for climbing — directionality, high μ', and low detachment force. Directionality is clearly apparent from Figure 3.24 and previous figures. A high Coefficient of Adhesion is achieved by loading the DPS in the proper direction. Figure 3.19 shows that negligible preload forces can be achieved when the DPS are preloaded along the proper approach trajectory while still generating significant amounts of adhesion. Finally, low detachment forces are achieved because the experimental limit surface of the DPS roughly intersects the origin in force-space. This allows the DPS to detach with negligible forces, further demonstrated by the data in Figure 3.12 for pulloff angles above 135°.
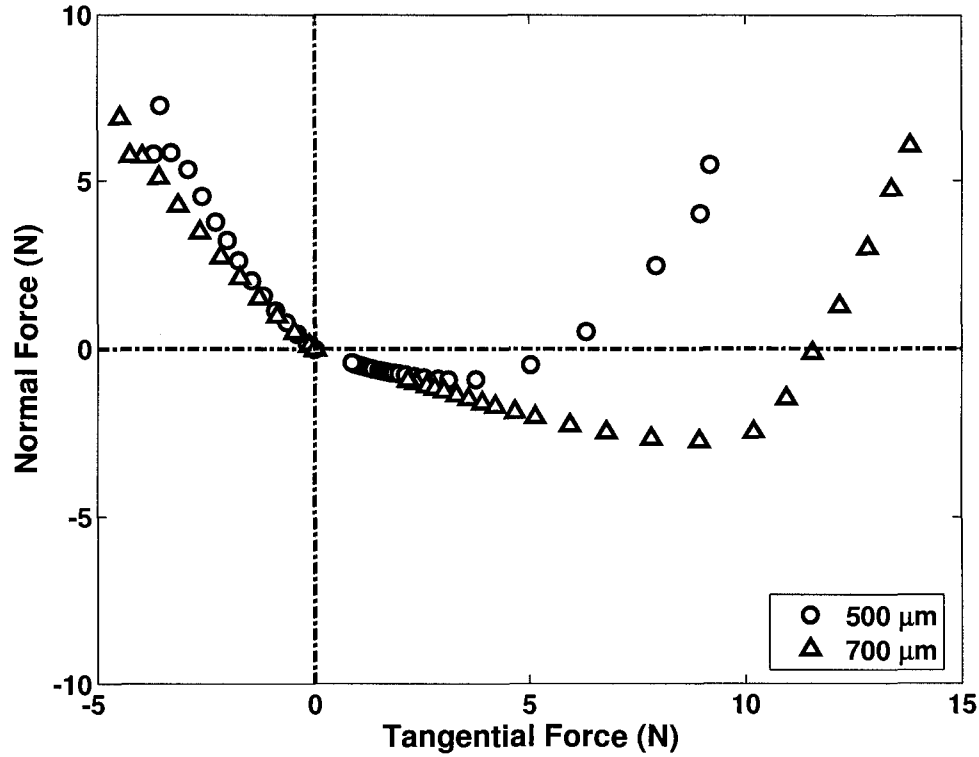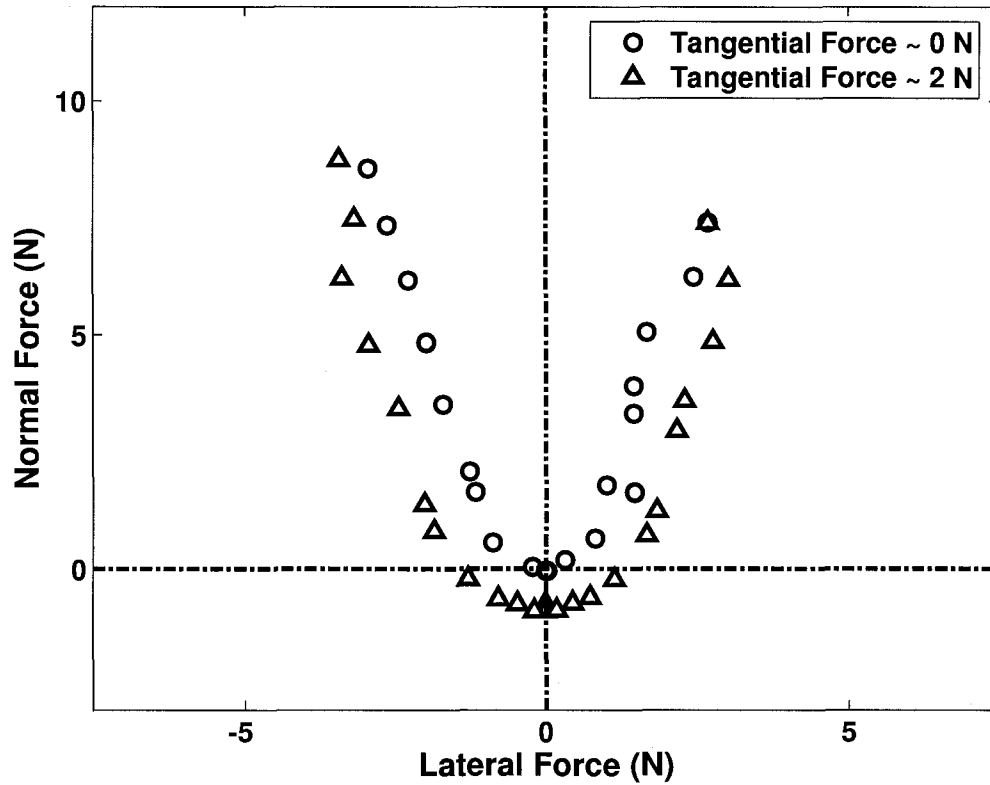
Figure 3.25: Contact failure forces of the DPS plotted in force-space in the XZ-plane. Data is shown for a preload depth in the normal direction of 700μm. Each data point is an average of three trials. Data is shown for contact failure forces that had a tangential component of about 0N and about 2N.

The DPS were also tested under lateral motions to characterize how forces in the lateral direction affect adhesion. While no data has been published for the gecko adhesive system under these conditions it is nevertheless important to characterize the DPS in three dimensions. This full understanding can allow three-dimensional analysis for purposes of design and control of climbing robots.

Figure 3.25 shows how lateral forces affect the adhesive performance of the DPS. The DPS were preloaded along a 45° approach angle to various preload depths in the normal direction ranging from 400μm to 700μm. The patches were then pulled away from the substrate along various straight-line paths formed from components in the normal, tangential, and *lateral* directions. This imparted lateral forces in addition to

tangential and normal forces to the contact interface. Speed was held constant across all experiments at 1mm/s.

Figure 3.25 shows data for two levels of tangential force. Essentially, these experiments can be thought of as first loading the DPS to a desired level of tangential force and then applying increasing lateral forces and measuring the contact failure. In truth, all three force components generally increase simultaneously up to the contact failure point. In either case the data in Figure 3.25 shows how the normal and lateral forces are related.

When no adhesion is present the DPS behave similarly to Coulomb friction. The larger the normal force the higher the lateral loads sustainable before sliding. When adhesion is present, increasing lateral loads decrease the adhesion. This behavior is quite similar to the Embedded Cone model or the JKR model discussed in Section 2.2. Not surprisingly the data is symmetric about the normal axis because the DPS themselves are symmetric about the YZ-plane. The JKR model (or any of the variations of that general class of model) captures the qualitative behavior of the DPS in the XZ-plane quite well.

Until now the behavior of the DPS in force-space has been explored from a strictly two-dimensional perspective. The limit surface concept was introduced in Section 2.1 and examples of two-dimensional limit curves were shown, similar to the data shown in the previous figures. However, it was also noted that pictures such as the friction cone example in Figure 2.3 were incomplete. In reality, the friction cone is a three-dimensional limit surface formed by rotating Figure 2.3 about the normal axis. The data shown here in Figures 3.23 and 3.25 are basically "slices" of a three-dimensional picture of the DPS in force-space.

Figures 3.26 and 3.27 show the three-dimensional experimental limit surface constructed using contact failure data gathered for the DPS. Data to construct the limit surfaces was gathered from experiments described above. The DPS patches were preloaded along a 45° approach trajectory to a preload depth in the normal direction between 400μm and 700μm. They were then pulled away from the substrate along straight-line paths formed from components in the normal, tangential, and lateral directions. The pulloff trajectories can be visualized as rays extending from an origin
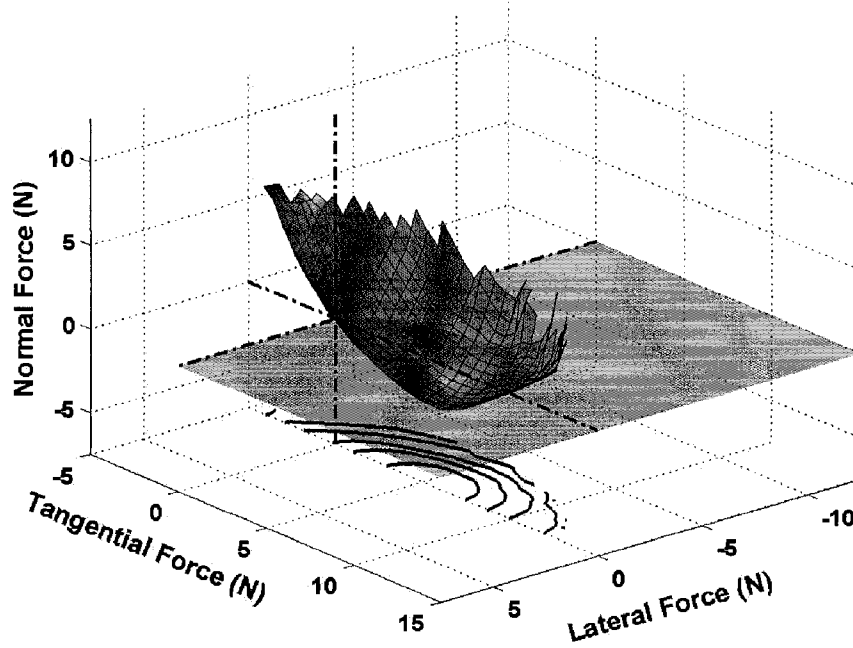
Figure 3.26: Three-dimensional experimental limit surface of the DPS. Surface is constructed via linear interpolation of actual experimental data. Only one half of data is used for sake of clarity because experimental data is roughly symmetric about XZ-plane. Data for construction of surface shown was gathered from experiments using a preload depth of 600μm.

to the surface of a hemisphere. Three trials were performed at each combination of preload depth and pulloff path. Pulloff forces were determined by using the maximum power method in all cases, and the limit surfaces are constructed by linear interpolation of the experimental data.

Both figures actually show only one half of the limit surface for the sake of clarity since the experimental data was roughly symmetric about the YZ-plane (Figure 3.25). Figure 3.26 shows the constructed limit surface along with projected contour lines and a plane dividing the positive and negative directions of the normal axis, highlighting the adhesive parts of the limit surface (parts of the surface below the plane). Figure 3.27 shows the same limit surface rotated through different viewing angles to aid in
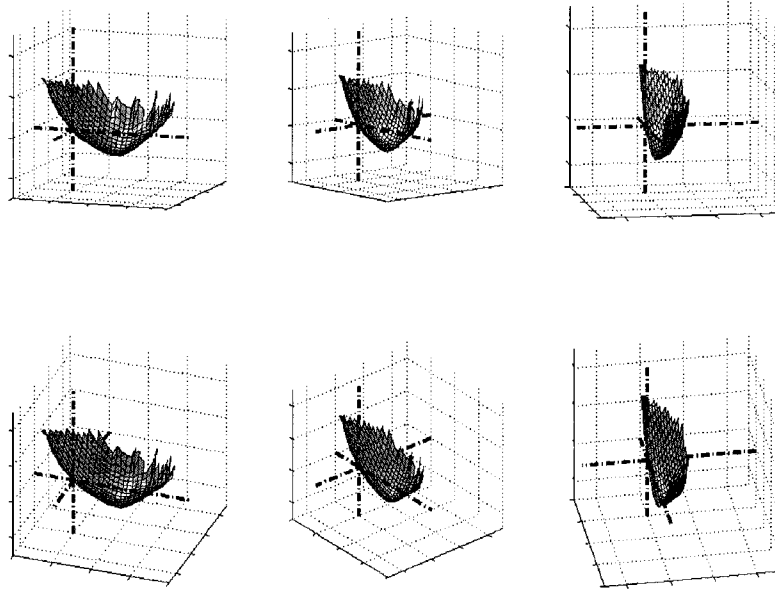
Figure 3.27: Different views of the experimental limit surface of the DPS. The surface shown is the same as that shown in Figure 3.26 without added axes details for sake of clarity.

visualization of its three dimensional aspects.

The DPS limit surface is bowl-shaped and clearly directional. The surface first dips into the adhesive regime as tangential forces increase. Further increases in tangential force cause the surface to rise out of the adhesive regime into the positive normal half-space Increasing lateral loads in either direction cause a decrease in the adhesive forces as the surface rises into the positive normal half-space to either side of the YZ-plane.

The experimental limit surface can be directly used to determine whether various combinations of normal, tangential, and lateral forces will cause failure of the DPS. If the forces in question lie inside the surface then they will not cause failure but if they lie outside the surface then the DPS will either begin sliding or pulloff from the

substrate. The experimental limit surface can also be used to analyze and develop various designs and control strategies for climbing robots and to gain insight into the climbing behavior of geckos, both of which will be explored in Chapter 4.

3.4.7 Combining Limit Surfaces from Different Contacts

In practice, one DPS patch may be insufficient to achieve the desired level of adhesion for a given application. As mentioned earlier, the DPS patches are used on the toes of an experimental climbing platform [70]. For this particular application, four patches are required at each foot to enable the robot to successfully climb vertical surfaces. To simplify the analysis and control of such platforms the limit surface concept can be extended to include combinations of individual contact limit surfaces. This is readily achieved using Minkowski sum techniques [52, 107] and results in a new effective limit surface for the contact.

A Minkowski sum is a way to add different polygons in n-dimensional space to one another. When the polygons are convex and contain the origin there are some simple ways to perform Minkowski addition. The boundary of a convex polygon can be described by a set of vectors pointing from the origin to every point on the polygon's boundary. The Minkowski sum is then the sum of every boundary vector from one polygon to every boundary vector from the second polygon. The new polygon is given by the largest bounding vectors in every direction returned from the sum. Mathematically, if each polygon is described as a set of vectors A and B, then the Minkowski sum is given by

$$A + B = \{a + b | a \in A, b \in B\}. \tag{3.4}$$

The Minkowski addition technique can be applied to either experimental data as shown in Figures 3.22 through 3.27 or to theoretical models such as those given in Figures 2.4 and 2.13. When performing the addition experimentally, every data point from one limit surface is added to every data point in the other limit surface. The new experimental limit surface is then given by the bounding points in the new data set (i.e. the points furthest from the origin in any given direction). When
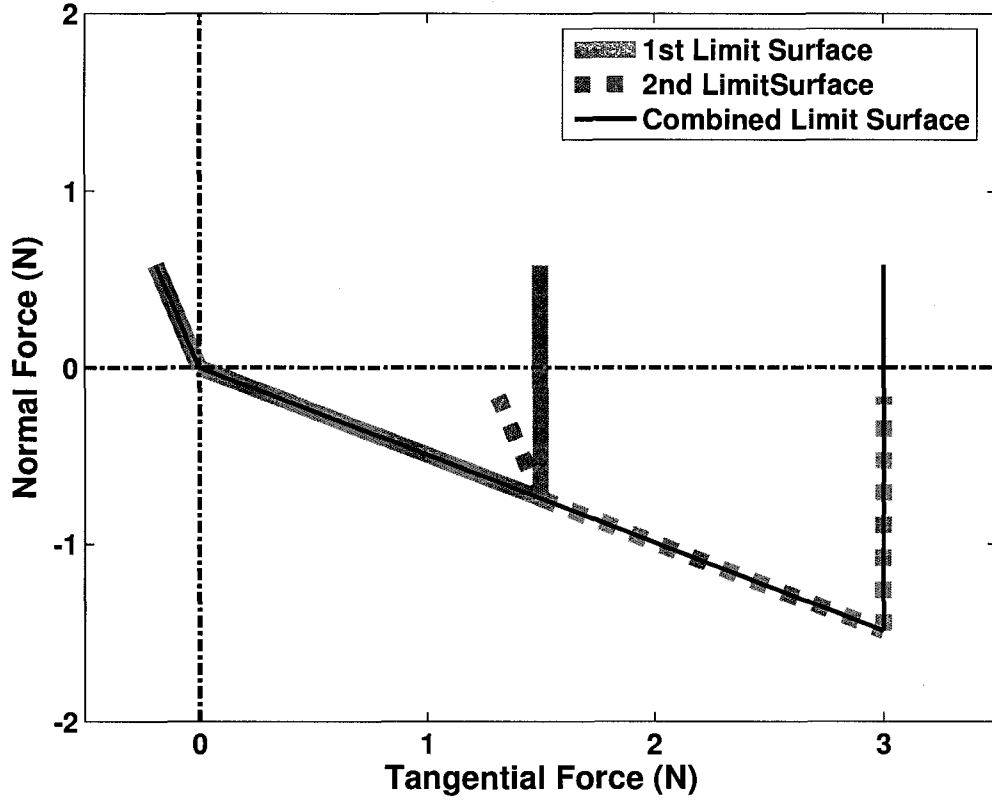
Figure 3.28: Example of the addition of two frictional adhesion limit surfaces using Minkowski sum techniques. The second frictional adhesion limit surface is superimposed along the surface of the first and the outermost boundary is taken as the new resultant limit surface.

adding theoretical limit surfaces, the solution can be arrived at quickly by simply superimposing the origin of one limit surface at each point along the boundary of the other limit surface. The outermost boundary is the new effective limit surface.

These techniques can be used to estimate the overall limit surface for a contact that uses multiple patches of the DPS. Figure 3.28 shows a simple example of this using the two-dimensional frictional adhesion contact model. Such a case might describe the net effect of two toes of a gecko that are side by side. When the contacts are oriented at different angles to each other in the case of three-dimensional limit surfaces, the sum must be taken in a common reference frame. These methods do not take into

account moment effects and only provide an approximation for the actual contact behavior since there may be complex interactions between multiple close contacts; however, they allow a simple method for handling multiple contacts that enables more complex analysis and control.

3.5 Summary

A directional adhesive termed Directional Polymer Stalks (DPS) was manufactured using conventional machining and molding techniques. The DPS are comprised of angled, microstructured stalks, 380μm in diameter, made out of a soft polyurethane ($E \approx 300$kPa). The angled nature of the stalks ($20°$) and the stalk faces ($45°$) imparts a directional nature to the adhesive characteristics of the DPS. The fibrillar nature of the DPS creates an effective stiffness much less than the bulk stiffness of the material from which they are manufactured.

The DPS were tested to determine their adhesive capabilities and verify their directional nature. Previous experimental investigations of synthetic adhesives have been limited to testing the adhesive in only the normal direction resulting in a one-dimensional characterization of adhesion. A directional adhesive necessitates a two-dimensional characterization at a minimum in order to demonstrate the directionality of the adhesive. A full three-dimensional characterization is even more useful for providing a complete picture of what forces can be transmitted at the contact between the adhesive and the substrate. In order to explore the three-dimensional behavior of the DPS a custom experimental setup was constructed and described. This setup allows motion trajectories in three dimensions to be applied to the DPS relative to a flat substrate.

Experimental procedures were developed to explore the behavior of the DPS. The DPS were first thoroughly cleaned with soap and water and then dried with compressed air. After mounting to the experimental setup, the DPS were aligned to a flat glass substrate using a manual 2-axis tilt stage. Various motion trajectories were applied, bringing patches of the DPS into and out of contact with the substrate. The forces transmitted at the contact interface were measured with a force/torque

transducer and recorded. Force and motion profiles were analyzed to extract useful information in order to characterize the adhesive qualities of the DPS patches.

Various adhesive aspects of the DPS were shown. The DPS exhibited a pulloff force that is highly dependent on the pulloff angle ($\approx$ 1N at 45° and $\approx$ 0N at 135°), clearly demonstrating their directional nature. The effects of both preload magnitude and preload trajectory were explored. Increasing preload magnitude increased the maximum adhesive forces up to a saturation point at a preload depth of about 700μm. Optimal preload approach trajectories of about 45° were found for minimizing the preload force while maximizing the pulloff force. These experiments also verified that the DPS had an effective stiffness ($\approx$ 30kPa) much lower than the bulk stiffness of the polyurethane from which they were manufactured. Pulloff forces generally increased with increasing pulloff speed.

The Coefficient of Adhesion and Work of Adhesion, two common adhesive metrics, were shown as a function of various experimental conditions. The Coefficient of Adhesion was highly dependent on the pulloff angle and preload approach trajectory and had a maximum of about 5 at a pulloff angle of 30° and a preload approach of 45°. Limitations of the Coefficient of Adhesion as an adhesive metric were also discussed with respect to the DPS, which exhibited negligible preload forces at some approach trajectories resulting in noisy and/or meaningless values for the Coefficient of Adhesion. The Work of Adhesion was shown to vary by a factor of as much as 40 over the different pulloff angles tested.

Finally, the contact forces at contact failure of the DPS were analyzed in force-space. This allowed comparison between the experimental results from the DPS and earlier discussion of adhesive contact models. The DPS were shown to exhibit similar characteristics to both the Kendall peel model and the Frictional Adhesion model when looked at in the YZ-plane. These results verify that the DPS indeed exhibit qualities similar to the gecko adhesive system. In the XZ-plane, the DPS more closely resembled the JKR model or the Embedded Cone model. The full three-dimensional limit surface of the DPS was constructed and discussed along with methods for handling multiple contacts. This experimental limit surface provides a concise description of the adhesive behavior of the DPS and can be used for a variety

of purposes including analysis, design, and control.

Chapter 4

Climbing Analysis of a Robot or Gecko Using Directional Adhesion

The analysis of simplified models can be used to better understand climbing. When studying climbing, one of the first questions that is invariably asked deals with stability — will the robot/animal be able to stay on the wall? This chapter will develop and use some analytical methods to study models representing either climbing robots or animals. A formulation is presented that explores the clinging ability of two- and three-dimensional multi-limbed bodies on flat inclined planes. In general, clinging ability may depend on the geometric configuration of the model and/or the assumptions about the forces and moments that can be transmitted at the contacts.

This chapter will primarily focus on the stability and internal forces of gecko-like climbers at different angles of inclination (e.g. horizontal, sloped, vertical, overhanging) and using different contact models for the foot-substrate interactions. The contact models used in this chapter are presented in Chapters 2 and 3. Important climbing principles resulting from this analysis are then explained. In particular, different contact models lead to drastically different strategies for distributing forces to the contact points. Important differences between isotropic and anisotropic contact models are highlighted. Orientation of the foot contact and how it plays a role in determining clinging ability is discussed. Finally, methods to efficiently represent and control the internal forces of a climbing robot are touched upon.

4.1 Two-Dimensional Force Analysis

This section sets up and analyzes a simple two-dimensional model representing either a climbing robot or animal. While a two-dimensional model is much simpler than anything existing in reality, such models have previously proved useful for the analysis of running and walking robots [93, 92]. This analysis focuses on static equilibrium requirements and internal forces and is adapted from a previous analysis of grasping and dexterous manipulation [65]. Similar analyses have been formulated by others [26, 74] that also explore internal forces and grasping but differ in solution methods. The analysis is performed using different contact models, thus exploring how the foot-substrate interactions affect overall clinging ability. Results using these different contact models are compared to one another and to existing data for geckos.

4.1.1 Model and Analysis Description

Figure 4.1 shows a schematic representation of the two-dimensional model. It is a simplified representation of an animal or robot viewed in the sagittal plane. The center of mass is supported by a front foot and a rear foot that rest on a flat inclined plane. The model is fully described by the following parameters: gravity (g), the mass (m), the coordinates of the front and rear feet with respect to the center of mass (y_1, z_1, y_2, z_2), and the angle of the inclined plane (θ). Note that for a flat plane, both z-coordinates of the feet are equal and equivalent to the height of the center of mass from the surface. Each foot is treated as a point contact able to transmit forces but not moments. Reaction forces exist at each foot, labeled F_{1T}, F_{1N}, F_{2T}, and F_{2N} for the front foot tangential force, the front foot normal force, the rear foot tangential force, and the rear foot normal force, respectively. A coordinate frame aligned with the inclination angle is also shown, and foot coordinates and forces are given with respect to this frame.

The planar system in Figure 4.1 has three requirements for static equilibrium. The forces in the Y and Z directions must sum to zero and the moments about the X direction (not shown) must sum to zero. The forces acting on the system consist of the force due to gravity and the contact forces at each of the foot contacts. The
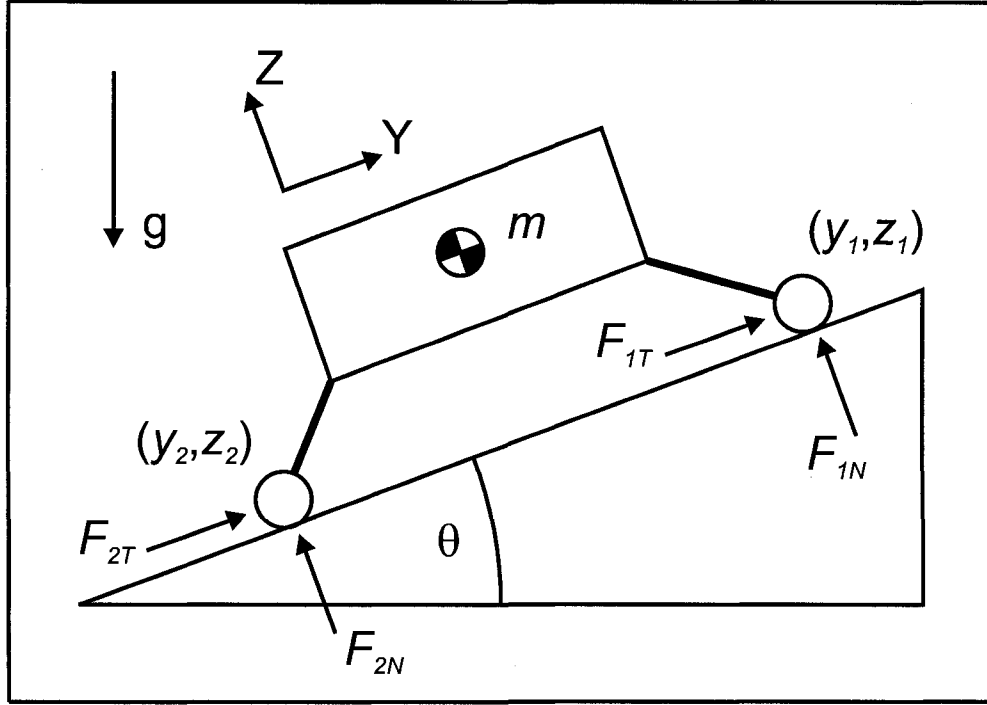
Figure 4.1: Two-dimensional model representing either a climbing robot or climbing animal. The center of mass is supported by two point contacts capable of transmitting forces but not moments. The angle of the inclined plane can be varied to explore clinging ability on sloped, vertical, and even overhanging surfaces.

static equilibrium requirements can be written mathematically as

$$\begin{aligned}
\sum F_Y &= & F_{1T} + F_{2T} & &=& \quad mg\sin(\theta) \\
\sum F_Z &= & F_{1N} + F_{2N} & &=& \quad mg\cos(\theta) \\
\sum M_X &= & y_1 F_{1N} - z_1 F_{1T} + y_2 F_{2N} - z_2 F_{2T} & &=& \quad 0.
\end{aligned} \tag{4.1}$$

Equation 4.1 can also be written compactly in matrix form as

$$\mathbf{WC} + \mathbf{F} = \mathbf{0} \tag{4.2}$$

where

$$\mathbf{W} = \begin{bmatrix} 1 & 0 & 1 & 0 \\ 0 & 1 & 0 & 1 \\ -z_1 & y_1 & -z_2 & y_2 \end{bmatrix}, \tag{4.3}$$

$$\mathbf{C} = \begin{bmatrix} F_{1T} \\ F_{1N} \\ F_{2T} \\ F_{2N} \end{bmatrix}, \tag{4.4}$$

and

$$\mathbf{F} = \begin{bmatrix} -mg\sin(\theta) \\ -mg\cos(\theta) \\ 0 \end{bmatrix}. \tag{4.5}$$

The system in Equation 4.2 contains four unknowns, the contact forces at the feet, and three equations. To achieve static equilibrium, a set of forces that satisfies Equation 4.2 must be found. Because the system is under-constrained (there are more unknowns than equations), an infinite number of solutions exists. Specifically, the system described in Figure 4.1 has one degree-of-freedom corresponding to the null space of $\mathbf{W}$. That degree-of-freedom can be written as

$$\lambda = F_{1T} - F_{2T}, \tag{4.6}$$

where λ is an internal force that does not affect static equilibrium. When λ is positive there is an internal "squeezing" or "pinching" force between the two feet and when λ is negative there is an internal "spreading" force between the two feet. In other words, λ describes how the system distributes the total shear load to the two contact points.

The infinite solution space of Equation 4.2 prematurely and incorrectly implies that a stable solution always exists; however, the stability requirements of the contacts have yet to be incorporated. These requirements depend on the details of the foot-substrate interaction and consist of inequalities governing the forces that can be

transmitted at the contact without failure by either sliding or separation. Examples of contact force requirements are presented in Sections 2.1 and 2.2 where the limit surface description is essentially a concise graphical representation of the contact force requirements. The only restriction imposed on these requirements for the present analysis is that they be linear in the contact forces.

For the purpose of presenting the general analysis of the model, the foot contact is assumed to follow the Coulomb friction law. The restrictions on the forces at the contacts are then

$$
\begin{aligned}
|F_{1T}| &\leq \mu_1 F_{1N} \\
|F_{2T}| &\leq \mu_2 F_{2N},
\end{aligned}
\tag{4.7}
$$

where μ_1 and μ_2 are the coefficients of static friction at each foot. Because of the linear restriction, these inequalities can be written compactly in matrix form as

$$
\mathbf{AC} \geq \mathbf{P},
\tag{4.8}
$$

where

$$
\mathbf{A} =
\begin{bmatrix}
1 & \mu_1 & 0 & 0 \\
-1 & \mu_1 & 0 & 0 \\
0 & 0 & 1 & \mu_2 \\
0 & 0 & -1 & \mu_2
\end{bmatrix},
\tag{4.9}
$$

$$
\mathbf{P} =
\begin{bmatrix}
0 \\
0 \\
0 \\
0
\end{bmatrix},
\tag{4.10}
$$

and $\mathbf{C}$ is given in Equation 4.4.

The inequality in Equation 4.8 now places restrictions on the infinite solution space of Equation 4.2 and there may or may not be solutions that satisfy both equations. To determine the potential range of feasible solutions, $\mathbf{C}$, the solution vector, can be

split into its particular and homogeneous parts as

$$\mathbf{C} = \mathbf{C_p} + \mathbf{C_h}. \tag{4.11}$$

The particular solution is given by

$$\mathbf{C_p} = -\mathbf{W}^\dagger \mathbf{F}, \tag{4.12}$$

where $\mathbf{W}^\dagger$ is the pseudo-inverse of $\mathbf{W}$ and produces the least-norm solution to Equation 4.2. The homogeneous solution is given by

$$\mathbf{C_h} = \mathbf{N}\lambda, \tag{4.13}$$

where $\mathbf{N}$ is the nullspace of $\mathbf{W}$, and, for the present case, is given by

$$\mathbf{N} = \begin{bmatrix} \frac{1}{\sqrt{2}} \\ 0 \\ -\frac{1}{\sqrt{2}} \\ 0 \end{bmatrix}, \tag{4.14}$$

which represents combinations of forces that have no affect on the static equilibrium requirements in Equation 4.1.

Equations 4.8, 4.11, 4.12, and 4.13 can be combined to form

$$\mathbf{AN}\lambda \geq \mathbf{P} + \mathbf{AW}^\dagger \mathbf{F}, \tag{4.15}$$

which is now an inequality only in λ, the independent degree-of-freedom, and not in the four contact forces. Equation 4.15 imposes certain restrictions on the internal force in order to satisfy the inequality constraints given by the contact model. Each row of the matrix inequality in Equation 4.15 represents a contact model constraint given in Equation 4.7. If there exists a λ for which Equation 4.15 is satisfied then there is a set of forces that achieves stability for the model shown in Figure 4.1; otherwise, there is no set of forces that will both solve Equation 4.2 and satisfy Equation 4.8.

One method for finding a solution to Equation 4.15 is to reformulate it into an

optimization problem and use linear programming. An optimal λ^* can be defined as the λ that maximizes the distance from violating any of the constraints in Equation 4.15. The distance from violating each constraint can be written as

$$[\mathbf{AN}]_i \lambda - d \geq [\mathbf{P} + \mathbf{AW}^\dagger \mathbf{F}]_i, \tag{4.16}$$

where the i subscript denotes the ith row and d is the distance from violating the constraint. If d is positive then the original constraint was satisfied; furthermore, the larger the value of d, the better λ is at satisfying the constraint. The distance to all of the constraints must be simultaneously considered, which results in

$$\begin{bmatrix} \mathbf{AN} & | & -\mathbf{1} \end{bmatrix} \begin{bmatrix} \lambda \\ d \end{bmatrix} \geq \mathbf{P} + \mathbf{AW}^\dagger \mathbf{F} \tag{4.17}$$

where $\mathbf{AN}$ has been concatenated on the right by a vector of negative ones and λ has been appended on the bottom by d. Equation 4.17 represents a standard linear programming problem where d is the objective function to be maximized, and it can be readily solved by various mathematical analysis tools including Matlab. If d is a positive number then there exists a solution that satisfies Equations 4.2 and 4.8 and the final contact forces can be constructed by using the particular solution given in Equation 4.12 and by using the optimal λ to construct the homogeneous solution.

When formulating the problem this way, the structure of $\mathbf{A}$ can have ramifications on the final solution and on the interpretation of d. Introduction of d by concatenation can inadvertently weight each of the constraints differently. In order for all of the constraints to be weighted equally, each row of the constraint matrix, $\mathbf{A}$, must have equal magnitude. Alternatively, each row of $\mathbf{AN}$ can be concatenated by an appropriate scalar related to the magnitude of the row in question. If each row of $\mathbf{A}$ does have equal magnitude, then there is a simple way to weight each constraint with respect to the other constraints. For example, introducing a -2 instead of a -1 doubles the importance of that constraint. Furthermore, if each row of $\mathbf{A}$ has unit magnitude then d has a direct physical interpretation. Under these circumstances, d represents the stability margin of the solution and becomes the distance in Newtons
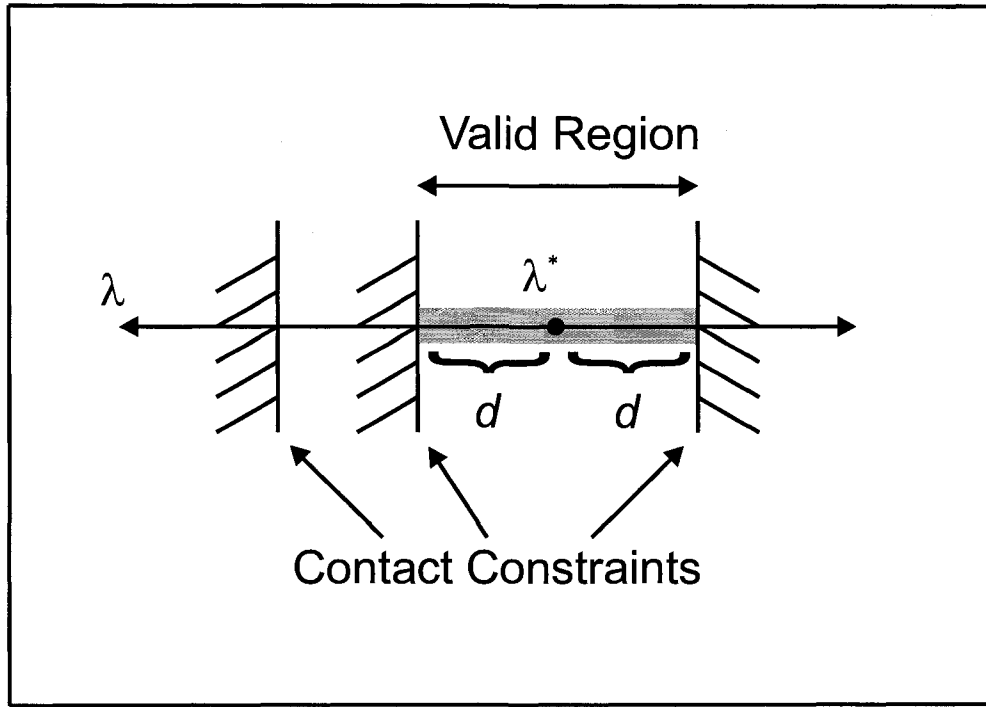
Figure 4.2: Schematic representation of the optimal solution to the two-dimensional model in Figure 4.1 using linear programming. The horizontal line represents the unbounded solution space of different values for λ. The vertical lines represent the inequality constraints imposed by the contact model requirements. The optimal λ, λ^*, is that which is furthest away from all of the constraints simultaneously, and the distance, d, returned by the optimization is the distance from λ^* to the constraints.

from a constraint. It directly corresponds to the maximum force that can be applied to any of the feet without violating the contact inequalities.

Throughout the rest of this discussion, while the contact inequalities and $\mathbf{A}$ may be presented in an un-normalized state, when solving the optimization problem, each constraint is first normalized such that each row of $\mathbf{A}$ has unit magnitude. Thus, each contact constraint is always weighted equally and d represents the stability margin of the system in Newtons.

This formulation can also be described visually. The model in Figure 4.1 is a system of four unknowns and three equations. An under-constrained system has an infinity of solutions in an n-dimensional space that all satisfy Equation 4.2. For

the specific model here, there is one degree-of-freedom and the solution space is a line extending from negative to positive infinity. However, the solution set is then constrained by the conditions required for the foot contacts to be stable. These inequalities are bounding hyper-planes in the solution space and valid solutions must lie on the appropriate sides of the hyper-planes in order to satisfy the inequality constraints. An optimal solution can be found by choosing a solution point in the bounded solution space that is furthest away from any of the bounding hyper-planes. For the one degree-of-freedom case, the bounding planes are merely points on a line, to which valid solutions must lie to the left or right.

Figure 4.2 shows graphically how the optimization finds a solution. The horizontal line represents the values λ can take and the vertical lines represent the constraints on λ given by the contact model. The hash marks on the vertical lines signify to which side of the constraint the valid solution must lie. The constrained space becomes the intersection of half-spaces formed from each constraint. The optimal solution, λ^*, is maximally distant from the boundaries forming the constrained space.

The formulation produces an optimal λ that directly correlates to optimal solutions for the contact forces at each foot. The contact forces are also optimal because they too are furthest from violating any of the stability requirements of the contact model. This can also be interpreted visually with the aid of the limit surface (Chapter 2). The contact forces at each foot form a point in force-space. The optimal solution for λ produces contact forces that are furthest from their respective contact model limit surface. Figure 4.3 shows a graphical example of this using the Coulomb friction limit surface. Maximizing the distance to each limit surface is done for all of the foot contacts simultaneously when λ is optimized.

4.1.2 Example Analysis Using Coulomb Friction

The above formulation can be used to ask simple questions about the model in Figure 4.1. Stability can be explored as a function of different geometric parameters (e.g. foot positions) or different contact model parameters (e.g. coefficient of static friction). This work is primarily focused on how different contact models affect the clinging
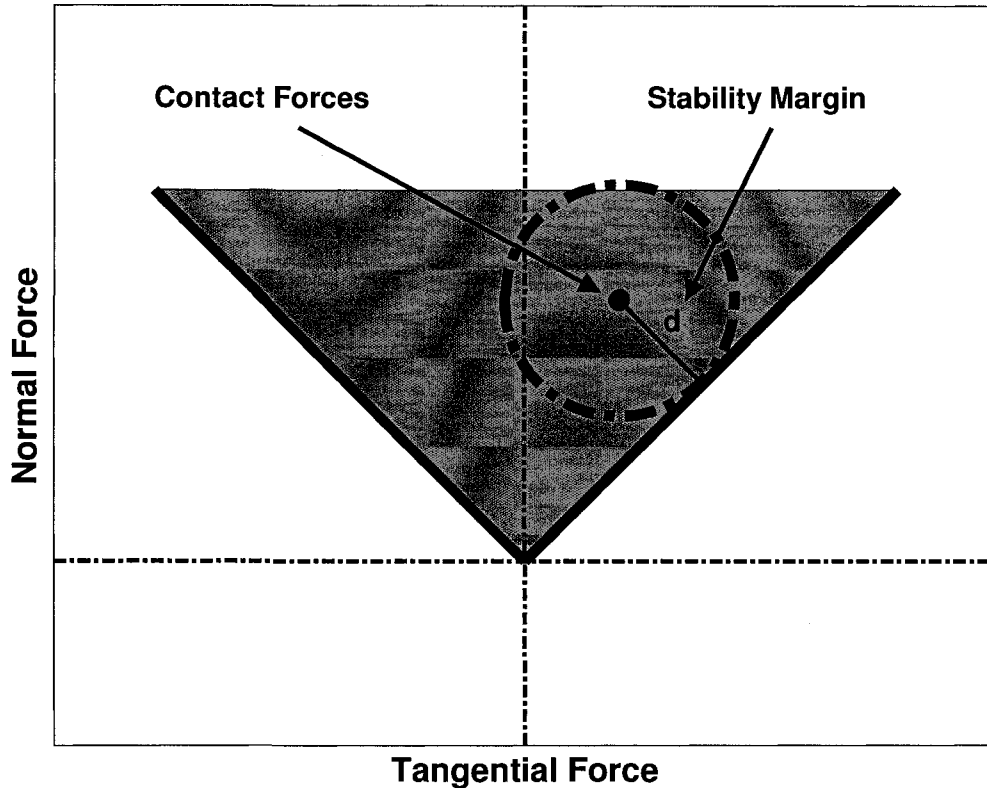
Figure 4.3: Schematic representation of the stability margin, d, given by the linear programming optimization. The stability margin is the distance from the contact forces to the closest point on the limit surface. This distance is maximized over all of the foot contacts simultaneously, and the final value of d is the minimum over all foot contacts.

ability of the model in Figure 4.1 on different inclines. This study will begin with an example exploring the stability and optimal contact forces of the system when Coulomb friction governs the foot-substrate interaction. Table 4.1 lists the model parameters used for this analysis, which were chosen to match typical characteristics of the Tokay gecko (*Gekko gecko*) [11]. Since the gecko adhesion system does not follow the Coulomb friction model, a relatively high friction coefficient was chosen based on the assumption that a "good" synthetic friction material could be used in the case of a climbing robot.

Figure 4.4 shows results from the analysis — internal force and the stability margin

Parameter	Value
Model Parameters	
g	$9.8\mathrm{m/s^2}$
m	50g
y_1	5cm
z_1	-2cm
y_2	-5cm
z_2	-2cm
θ	$0° : 180°$
Coulomb Friction Parameters	
μ_1	1.0
μ_2	1.0

Table 4.1: Model and contact parameters for internal force analysis using Coulomb friction to describe the foot-substrate interaction.

as a function of the angle of inclination. The internal force is zero when resting on a horizontal plane and negative for all angles between 0° and 180°. On a horizontal plane it is best for the two foot contacts to add no extra tangential force in either direction as this would bring the feet closer to slipping. As the inclination angle increases, the rear foot will see an increase in normal force and the front foot will see a corresponding decrease in normal force. The rear foot can bear more of the shear load compared to the front foot since it has a higher normal force component. This balance is optimized by the analysis and results in negative internal forces corresponding to the rear foot supporting more of the tangential load than the front foot.

The use of the internal force to maximize stability as the inclination angle increases can be viewed visually. The analysis can be thought of as first calculating the particular solution (least-norm solution to Equation 4.2). This produces a starting point in force-space for each foot. The internal force can then be used to move one contact point to the right while moving the other an equal amount to the left or vice versa. Figure 4.5 shows the forces at each foot in the horizontal configuration. In this configuration, the particular solution is already optimal since any positive or negative internal force would move the contact points closer to their limit surfaces. At higher inclination angles, such as 30°, the particular solution produces higher normal force
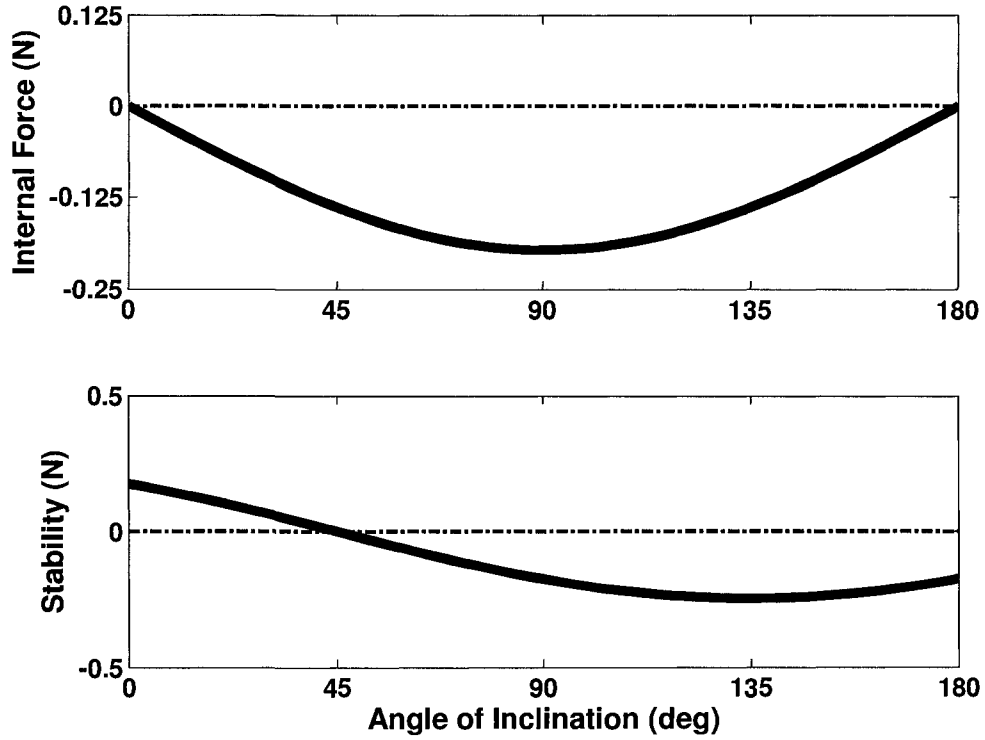
Figure 4.4: Internal force and stability margin of the two-dimensional model with Coulomb friction acting at the contact points. Angle of inclination is varied from 0° to 180°, 90° being vertical. Positive internal force corresponds to higher tangential forces at the front foot and negative internal force corresponds to higher tangential forces at the rear foot. A negative stability margin means that no solution exists that satisfies the equality constraints and the inequalities resulting from the contact model.

at the rear foot and lower normal force at the front foot (Figure 4.5) and equal tangential forces at each foot. In this case, the internal force can be used to adjust the tangential forces so that the distance from the limit surface is increased. Technically, the distance is increased at one foot and decreased at the other foot but the net result is an overall increase over both feet. This is shown with arrows in Figure 4.5.

The stability margin has a finite value of 0.173N at 0°. This value represents the maximum perturbation force that could be applied at any of the feet without causing contact failure. As the inclination angle increases this value decreases, eventually
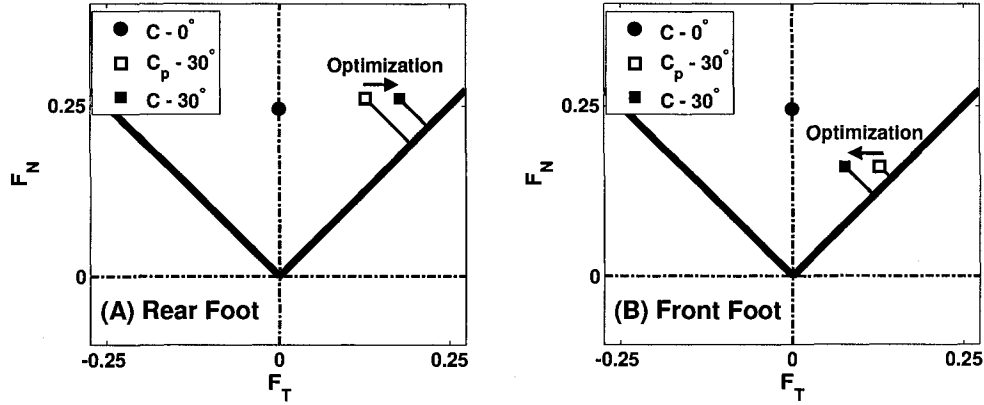
Figure 4.5: Graphical explanation of the role of the internal force in optimizing the stability. On a horizontal plane, any non-zero internal force only serves to move the contact points closer to the limit surface. At higher inclines, negative internal forces can move the particular solution of the system such that the net distance to the limit surface over both contacts is increased.

crossing zero at an inclination angle of 45°. That the analysis does not achieve stability at high angles of inclination is not surprising since Coulomb friction was assumed. As inclination angle increases there will reach a point when the front foot requires adhesion to resist pitch-back moments. The Coulomb friction model does not include any adhesion and hence will never produce solutions that are stable at high inclination angles. The next section will explore cases where contact models with adhesion are used to describe the foot-substrate interaction.

4.1.3 Comparison of Isotropic and Anisotropic Contact

As mentioned earlier, this analysis can use any set of linear inequality constraints to describe the contact model. An example was shown using Coulomb friction for the contact model, but this model lacks any adhesive characteristics and is therefore not very useful for studying climbing. This section will explore the results of using the above analysis with two different adhesive contact models — the Embedded Cone model and the Frictional Adhesion model. The Embedded Cone model provides a symmetric, isotropic contact model to contrast the directional, anisotropic Frictional

Parameter	Value
Embedded Cone Parameters	
μ	1.0
α	75% mg
Frictional Adhesion Parameters	
μ	1.0
α^*	30°
F_{max}	75% $\frac{mg}{\tan(\alpha^*)}$

Table 4.2: Contact parameters for internal force analysis using the Embedded Cone and Frictional Adhesion contact models.

Adhesion model. The Embedded Cone model also serves as a reasonable approximation to the JKR model and other similar models covered in Chapter 2. The Frictional Adhesion model provides an empirical model describing the gecko adhesion system and allows comparison of results to data for climbing geckos.

Geometric parameters are again chosen to roughly match the characteristics of a Tokay gecko and are given in Table 4.1. Table 4.2 lists the contact model parameters. The critical detachment angle (α^*) in the Frictional Adhesion model is chosen to match data obtained for geckos (Section 2.5). The adhesion coefficient in the Embedded Cone model and the shear limit in the Frictional Adhesion model are chosen to provide a maximum adhesive force of 75% of the body weight of the model. The same parameters are used for both front and rear foot contacts.

When using a different contact model only the **A** and **P** matrices change. The Embedded Cone model is described by the following inequalities:

$$|F_{1T}| \le \mu_1 \left(F_{1N} + \alpha_1\right)$$
$$|F_{2T}| \le \mu_2 \left(F_{2N} + \alpha_2\right).$$

(4.18)

These inequalities result in

$$\mathbf{A} = \begin{bmatrix} 1 & \mu_1 & 0 & 0 \\ -1 & \mu_1 & 0 & 0 \\ 0 & 0 & 1 & \mu_2 \\ 0 & 0 & -1 & \mu_2 \end{bmatrix}, \tag{4.19}$$

and

$$\mathbf{P} = \begin{bmatrix} -\mu_1 \alpha_1 \\ -\mu_1 \alpha_1 \\ -\mu_2 \alpha_2 \\ -\mu_2 \alpha_2 \end{bmatrix}. \tag{4.20}$$

One added degree of complexity is introduced when using the Frictional Adhesion contact model because of its directional property. In addition to the contact model parameters, the orientation of the contact must also be specified. It is necessary to know how the foot is pointed. For the model in Figure 4.1, the adhesive direction of the Frictional Adhesion model can be lined up with either the positive Y axis (aligned) or the negative Y axis (reversed). This creates up to four different cases: Case 1) front and rear foot aligned, Case 2) front foot aligned and rear foot reversed, Case 3) front foot reversed and rear foot aligned, and Case 4) front and rear foot reversed.

Simple inspection reveals that only two cases need be considered. Without going into detailed analysis, Case 4 will clearly lead to unstable results. In this configuration, gravity will load both contacts *against* their adhesive directions when the model is on a vertical surface. No internal force will produce contact forces that satisfy Equations 4.2 and 4.8. Another case can be eliminated based on symmetry. Cases 2 and 3 are opposite and will produce internal and tangential forces equal and opposite but an identical stability margin. While both cases are equally "good", Nature has evolved animal morphologies that are more conducive to Case 2 whereas Case 3 is seldom observed. Thus, only Cases 1 and 2 need be considered when using the Frictional Adhesion model or any other similar directional contact model.

The Frictional Adhesion model in the aligned configuration is described by the

following inequality constraints:

$$-F_T \leq \mu F_N$$
$$F_N \geq -F_T \tan(\alpha^*) \tag{4.21}$$
$$F_T \leq F_{max}.$$

These inequalities lead to

$$\mathbf{A} = \begin{bmatrix} 1 & \mu_1 & 0 & 0 \\ \tan(\alpha_1^*) & 1 & 0 & 0 \\ -1 & 0 & 0 & 0 \\ 0 & 0 & 1 & \mu_2 \\ 0 & 0 & \tan(\alpha_2^*) & 1 \\ 0 & 0 & -1 & 0 \end{bmatrix}, \tag{4.22}$$

and

$$\mathbf{P} = \begin{bmatrix} 0 \\ 0 \\ -F_{1max} \\ 0 \\ 0 \\ -F_{2max} \end{bmatrix}. \tag{4.23}$$

When the Frictional Adhesion contact model is reversed, the tangential force coefficients in A are simply negated.

Figure 4.6 shows the analysis results for just the Frictional Adhesion model using both Case 1 (both feet aligned) and Case 2 (rear foot reversed) configurations. They produce different results for both the optimal internal force and the stability margin. In particular, there are inclination angles when it is better to reverse the rear foot contact in order to achieve higher stability. On a horizontal surface, reversing the rear foot allows both feet to pull inward and increase the tangential force at each
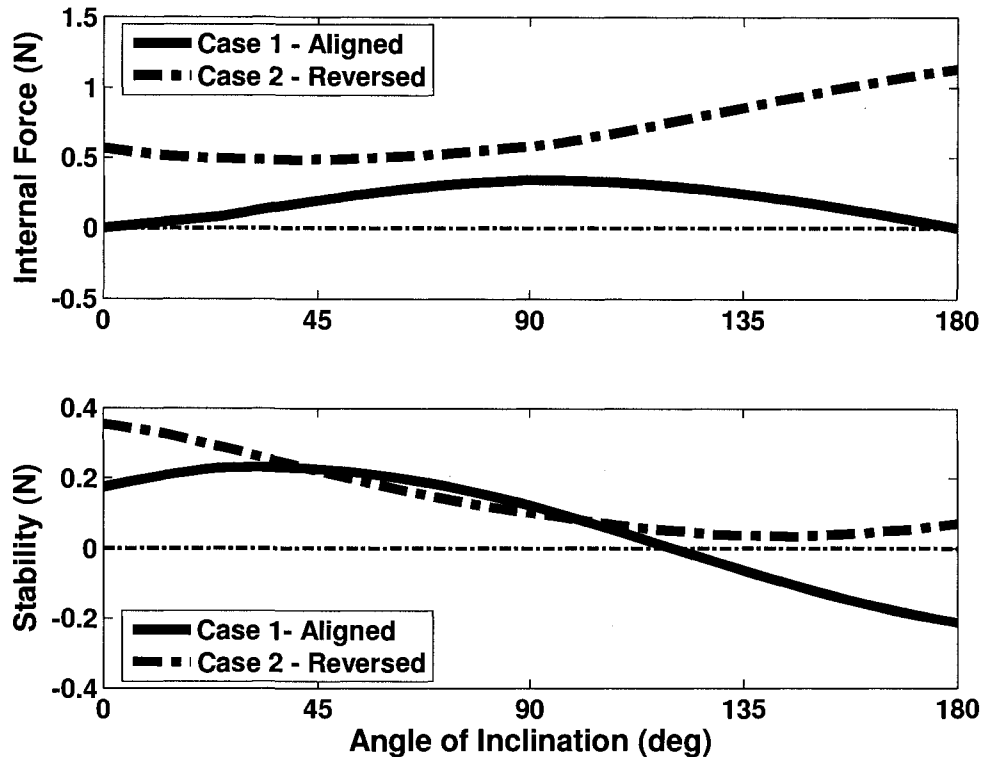
Figure 4.6: Internal force and stability margin of the two-dimensional model with Frictional Adhesion acting at the contact points. Case 1 (aligned) corresponds to the front and rear foot Frictional Adhesion models lined up with the positive Y axis of the model in Figure 4.1. Case 2 (reversed) corresponds to reversing the rear foot Frictional Adhesion model orientation so that the adhesive direction lines up with the negative Y axis.

contact. This in turn generates higher maximum adhesion in the Frictional Adhesion model. While stability on a horizontal surface is not necessarily critical, this rear foot reversal strategy does increase the system's resistance to perturbation forces. As the inclination angle increases it becomes better to have both foot contacts aligned and passively use gravity to load both contacts in the adhesive direction. However, as the inclination angle increases toward 180°, maintaining stability requires reversing the rear foot. On an inverted surface, no shear forces are present without an internal squeezing force. Reversing the rear foot allows the model to squeeze inward with both feet, generating tangential forces at each contact and thereby generating adhesion.
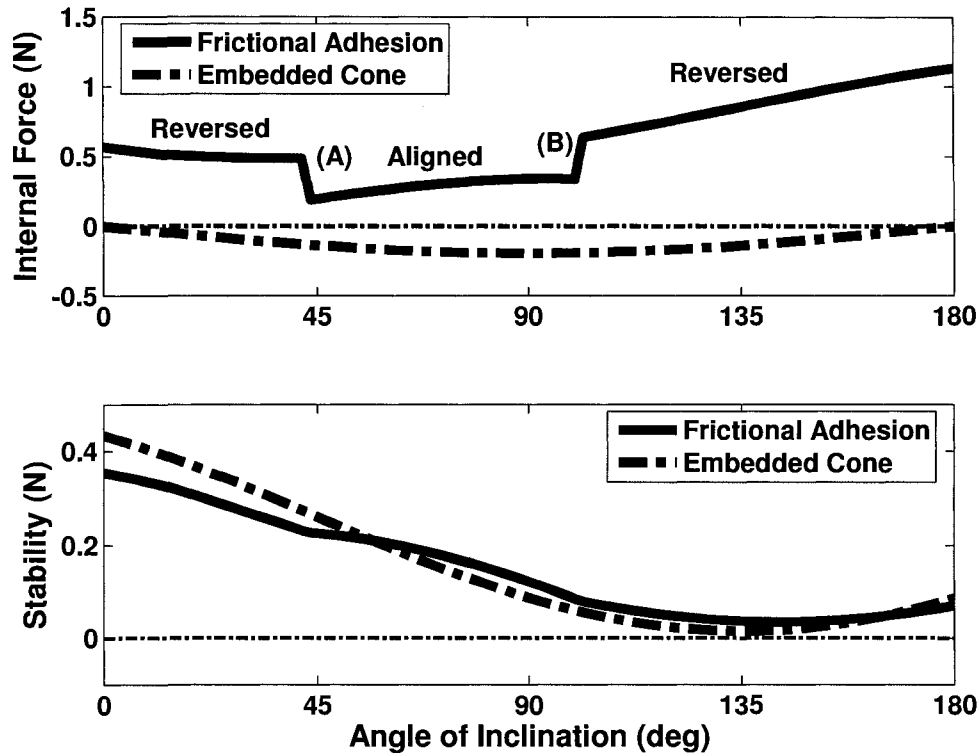
Figure 4.7: Comparison between the internal forces and stability margins of the two-dimensional model using the Embedded Cone and the Frictional Adhesion models. Both contact models produce results with similar stability margins but opposite internal forces. In the case of Frictional Adhesion, stability margin and internal force are shown for the foot orientation that produces higher stability margin. (A) and (B) point out transitions in rear foot orientation to achieve higher stability (Figure 4.6).

Because there are two (or more) cases to examine when using an anisotropic contact model, a few extra steps are required to find the optimal solution. Each case must be tested and the case that produces the highest stability margin is chosen for the final solution. Using this procedure, the results obtained with the Frictional Adhesion model can be compared to those obtained using the Embedded Cone model. This comparison is shown in Figure 4.7.

Due to choice of model parameters, both models provide stability over all inclination angles. However, the optimal internal forces are opposite. The Frictional

Adhesion model produces positive internal forces over all angles while the Embedded Cone model produces negative internal forces. In the Embedded Cone model, increasing the tangential force decreases the amount of adhesion available. As the angle increases, the front foot normal force is reduced and the rear foot normal force is increased. It is thus desirable for the rear foot to bear more of the total shear load because it has a higher normal force to work with. The opposite is true in the Frictional Adhesion model. It is better for the front foot to bear more of the total shear load because this will cause higher adhesion at the front foot where higher adhesion is necessary. In summary, Frictional Adhesion contacts result in a model that "pulls" itself up a wall with its front foot and Embedded Cone contacts result in a model that "pushes" itself up a wall with its rear foot.

The results using the Frictional Adhesion model qualitatively match experimental data obtained for geckos climbing up vertical surfaces. In studies of the reaction forces at each foot of a climbing gecko, the front feet exert higher shear loads than the rear feet [13]. This analysis helps to explain why geckos may distribute forces this way.

Frictional Adhesion has a number of advantages over isotropic adhesion (Embedded Cone model, JKR model) for the purposes of climbing. As discussed in Section 2.5, it allows adhesion to be *controllable*. This leads to low attachment and detachment forces and a high Coefficient of Adhesion. However, its directional nature requires that consideration be given to force control strategies. To climb successfully, contact forces must be properly distributed among the different feet. Directionality also causes contact orientation to become a non-trivial matter, which will be further explored in the next section.

Such issues can be illustrated by this analysis. The added implications for using directional adhesion can then be included in designing robots and controllers so they exploit the directionality of the adhesive. Furthermore, such analyses can aid in understanding why certain animals climb the way they do. In the gecko's case, the analysis explains why geckos put more shear load on their front feet than on their rear feet. For these and other reasons, it is important to understand how the foot-substrate interaction affects clinging ability.

4.2   Three-Dimensional Force Analysis

The previous section gained useful insights into climbing behavior and strategies using a simple two-dimensional model. The real world is a three-dimensional space and further insights can be gained by exploring the clinging ability of a three-dimensional model. In particular, Section 4.1 showed that contact orientation becomes very important when directional adhesion is involved. Many animals can control foot orientation to a greater or lesser degree and may use this ability to increase climbing performance. This section focuses on how contact orientation affects the clinging stability of a four-legged, three-dimensional model.

4.2.1   Model and Analysis Description

Figure 4.8 shows a schematic representation of the model. It consists of a center of mass supported by four point contacts on an inclined plane. The following parameters are introduced to describe the model: gravity (g), the mass (m), the coordinates of each foot with respect to the center of mass ($[x_n, y_n, z_n]^T$, $n = 1, 2, 3, 4$), the orientation of each foot about the normal axis of the inclined plane (ϕ_n, $n = 1, 2, 3, 4$), and the angle of the inclined plane (θ). Again, because the surface is a flat plane, all the z-coordinates of the feet are equal and equivalent to the height of the center of mass from the surface. Each foot contact has three associated reaction forces, F_{nL}, F_{nT}, and F_{nN} ($n = 1, 2, 3, 4$) for the lateral (X), tangential (Y), and normal (Z) directions.

Unlike the two-dimensional model, this system has six requirements for static equilibrium. Each of the forces and moments in the X, Y, and Z directions must sum to zero. The static equilibrium requirements are given by
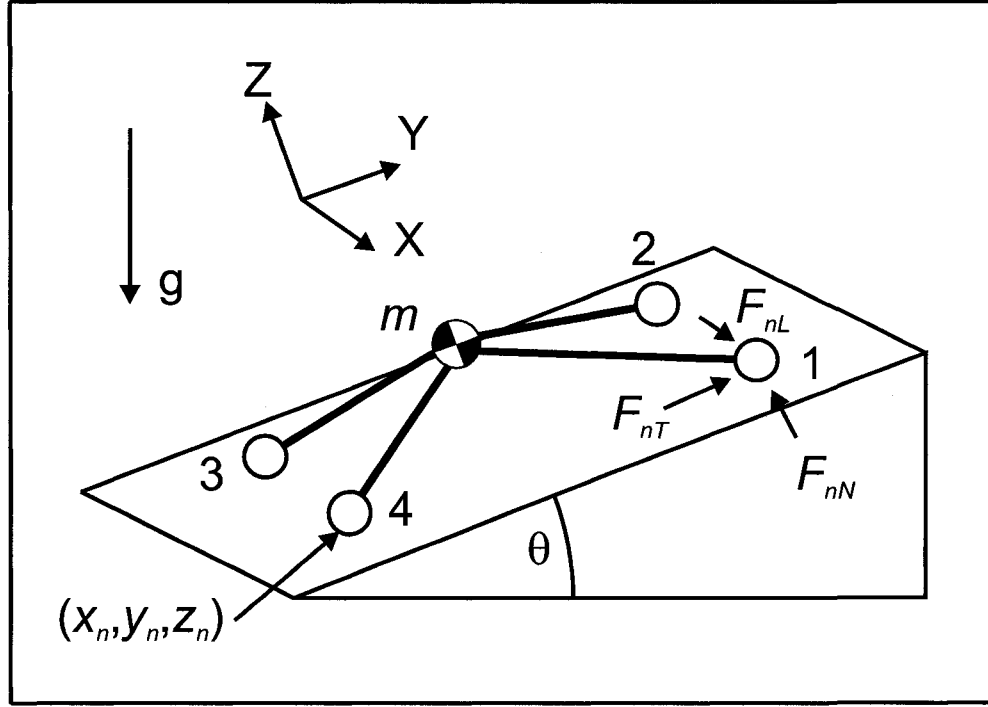
Figure 4.8: Three-dimensional model representing either a climbing robot or animal. The center of mass is supported by four point contacts capable of transmitting forces but not moments. Each contact has an associated orientation angle (not shown) which is the rotation of the contact frame about the Z axis.

$$
\begin{aligned}
\sum F_X &= F_{1L} + F_{2L} + F_{3L} + F_{4L} &= 0 \\
\sum F_Y &= F_{1T} + F_{2T} + F_{3T} + F_{4T} &= mg\sin(\theta) \\
\sum F_Z &= F_{1N} + F_{2N} + F_{3N} + F_{4N} &= mg\cos(\theta) \\
\sum M_X &= \sum_{n=1}^{4} \left(y_n F_{nN} - z_n F_{nT} \right) &= 0 \\
\sum M_Y &= \sum_{n=1}^{4} \left(z_n F_{nL} - x_n F_{nN} \right) &= 0 \\
\sum M_Z &= \sum_{n=1}^{4} \left(x_n F_{nT} - y_n F_{nL} \right) &= 0.
\end{aligned}
\tag{4.24}
$$

Equation 4.24 can be written compactly in matrix form as

$$
\mathbf{WC} + \mathbf{F} = \mathbf{0} \tag{4.25}
$$

where

$$W = \begin{bmatrix} I_3 & I_3 & I_3 & I_3 \\ \hat{R}_1 & \hat{R}_2 & \hat{R}_3 & \hat{R}_4 \end{bmatrix}, \tag{4.26}$$

I_3 is the 3×3 identity matrix, $\hat{R}_n$ is the cross-product operator given by

$$\hat{R}_n = \begin{bmatrix} 0 & -z_n & y_n \\ z_n & 0 & -x_n \\ -y_n & x_n & 0 \end{bmatrix}, \tag{4.27}$$

$$C = \begin{bmatrix} C_1 \\ C_2 \\ C_3 \\ C_4 \end{bmatrix}, \tag{4.28}$$

$C_n = [F_{nL}, F_{nT}, F_{nN}]^T$, and

$$F = \begin{bmatrix} 0 \\ -mg\sin(\theta) \\ -mg\cos(\theta) \\ 0 \\ 0 \\ 0 \end{bmatrix}. \tag{4.29}$$

For the three-dimensional model, Equation 4.25 contains twelve unknowns, three contact forces at each of four feet, and six equations. This leaves six degrees-of-freedom corresponding to different internal forces the feet can generate. Just as in the two-dimensional model, the stability requirements of the contacts can be introduced and an optimal solution found that maximizes the distance from violating any of the contact constraints. Again, the only stipulation on the contact constraints is that they be linear in the contact forces.

For this analysis, the contact constraints are formed by constructing a linear approximation to the experimental limit surface found for the synthetic directional adhesive in Chapter 3. The Frictional Adhesion model provides a starting point, and
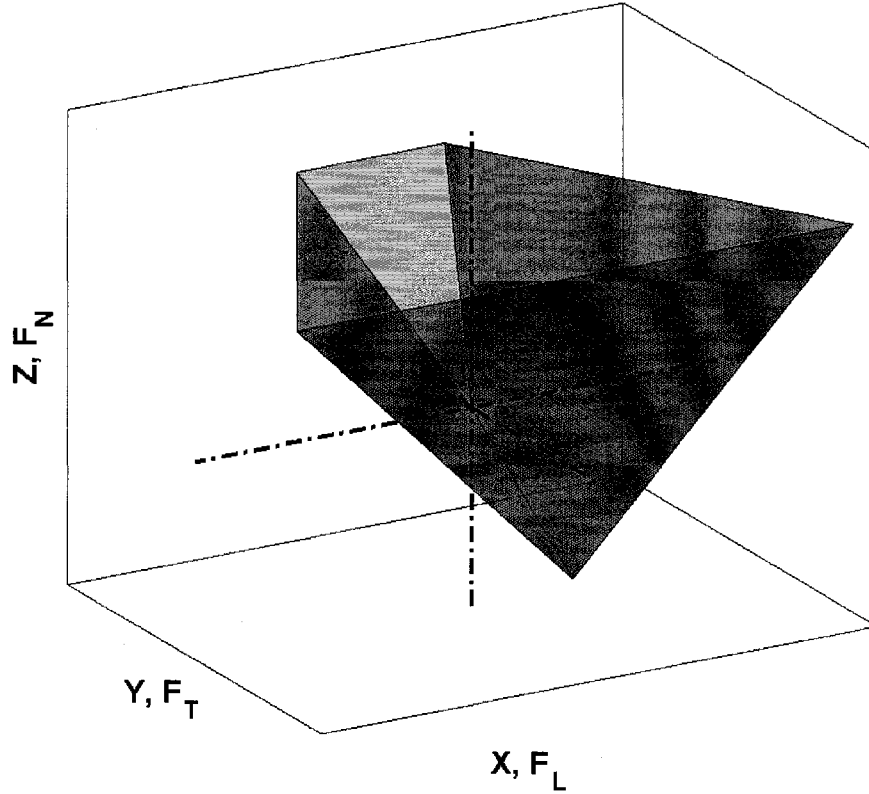
Figure 4.9: Three-dimensional limit surface based on results for a synthetic directional adhesive presented in Chapter 3. Lateral forces reduce the amount of adhesion in a linear relationship. Limit surface is identical to 2D Frictional Adhesion model in the YZ-plane ($F_T F_N$-plane) and identical to 2D Embedded Cone model in XZ-plane ($F_L F_N$-plane).

the trends shown in Section 3.4.6 allow the Frictional Adhesion model to be expanded into the lateral dimension. Increasing the lateral force decreases the adhesion limit in a linear relationship. Essentially, this produces a model that is similar to the Frictional Adhesion model in the YZ-plane ($F_T F_N$-plane) and similar to the Embedded Cone model in the XZ-plane ($F_L F_N$-plane).

The set of linear inequalities that mathematically describe the 3D directional adhesion contact model are

$$-F_T \leq \mu F_N$$

$$F_N \geq -F_T \tan(\alpha^*) + \frac{1}{\mu} |F_L| \qquad (4.30)$$

$$F_T \leq F_{max}.$$

The friction and maximum shear limits remain unchanged from Equation 4.21 but a penalty is added to the adhesion limit that is proportional to the lateral force. These inequalities are shown graphically in Figure 4.9, which is a linear approximation to the experimental limit surface shown in Figures 3.26 and 3.27. Each plane represents one of the contact constraints in Equation 4.30. Combinations of forces inside the limit surface produce stable contacts but forces outside the surface will fail by either sliding along or separation from the substrate.

In the three-dimensional analysis, each foot contact has an associated orientation. The limit surface and contact constraints describe the stable forces in terms of a contact frame. The lateral, tangential, and normal forces in the contact frame are not necessarily aligned with the lateral, tangential, and normal forces in the body frame of the model. In the two-dimensional analysis the isotropic contact models (Coulomb friction, Embedded Cone) do not need an orientation, and the anisotropic model (Frictional Adhesion) only has two choices for orientation. This allows the inequality constraint matrix, Equation 4.8, to be written directly in terms of the contact forces in the body frame. In contrast, the inequality constraints are given here in terms of the contact frame, which has an arbitrary orientation with respect to the body frame.

The contact inequality constraints can be written as

$$\mathbf{AC'} \geq \mathbf{P}, \qquad (4.31)$$

where $\mathbf{A}$, for the 3D directional adhesion model, is given by

$$\mathbf{A} = \begin{bmatrix} 0 & 1 & \mu_1 & & 0 & 0 & 0 \\ \frac{1}{\mu_1} & \tan(\alpha_1^*) & 1 & \cdots & 0 & 0 & 0 \\ -\frac{1}{\mu_1} & \tan(\alpha_1^*) & 1 & & 0 & 0 & 0 \\ 0 & -1 & 0 & & 0 & 0 & 0 \\ & \vdots & & \ddots & & \vdots & \\ 0 & 0 & 0 & & 0 & 1 & \mu_4 \\ 0 & 0 & 0 & \cdots & \frac{1}{\mu_4} & \tan(\alpha_4^*) & 1 \\ 0 & 0 & 0 & & -\frac{1}{\mu_4} & \tan(\alpha_4^*) & 1 \\ 0 & 0 & 0 & & 0 & -1 & 0 \end{bmatrix}, \qquad (4.32)$$

$$\mathbf{P} = \begin{bmatrix} 0 \\ 0 \\ 0 \\ -F_{1max} \\ \vdots \\ 0 \\ 0 \\ 0 \\ -F_{4max} \end{bmatrix}, \qquad (4.33)$$

and $\mathbf{C}'$ is the vector of contact forces in the individual contact frames,

$$\mathbf{C}' = \begin{bmatrix} F'_{1L} \\ F'_{1T} \\ F'_{1N} \\ \vdots \\ F'_{4L} \\ F'_{4T} \\ F'_{4N} \end{bmatrix}. \qquad (4.34)$$

Each set of contact forces in the contact frame can be transformed into contact forces in the body frame by a rotation matrix,

$$\mathbf{R_n} = \begin{bmatrix} \cos(\phi_n) & -\sin(\phi_n) & 0 \\ \sin(\phi_n) & \cos(\phi_n) & 0 \\ 0 & 0 & 1 \end{bmatrix}. \tag{4.35}$$

where

$$\mathbf{C_n} = \mathbf{R_n} \mathbf{C'_n}, \tag{4.36}$$

The full transformation is

$$\mathbf{C} = \mathbf{R} \mathbf{C'}, \tag{4.37}$$

where

$$\mathbf{R} = \begin{bmatrix} \mathbf{R_1} & 0 & 0 & 0 \\ 0 & \mathbf{R_2} & 0 & 0 \\ 0 & 0 & \mathbf{R_3} & 0 \\ 0 & 0 & 0 & \mathbf{R_4} \end{bmatrix}. \tag{4.38}$$

The solution to Equation 4.25 is again split into a particular and homogeneous solution. The two components can be transformed into the contact frames and become

$$\mathbf{C'_p} = -\mathbf{R^T} \mathbf{W^\dagger} \mathbf{F} \tag{4.39}$$

and

$$\mathbf{C'_h} = \mathbf{R^T} \mathbf{N} \lambda, \tag{4.40}$$

where λ is now a vector instead of a scalar as in the two-dimensional analysis. Equation 4.31 can now be written as

$$\mathbf{A} \mathbf{R^T} \mathbf{N} \lambda \geq \mathbf{P} + \mathbf{A} \mathbf{R^T} \mathbf{W^\dagger} \mathbf{F}, \tag{4.41}$$

which is a set of inequalities only in λ.

A solution is again found by reformulating Equation 4.41 into an optimization
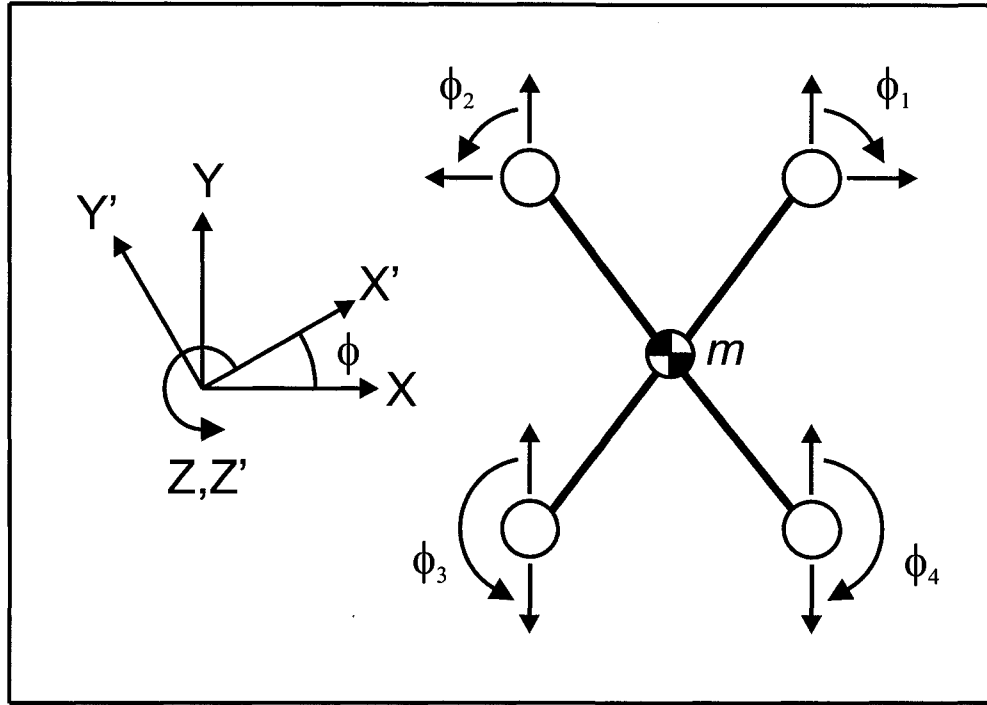
Figure 4.10: Foot orientation ranges used in the three-dimensional analysis. Right and left foot orientation angles are equal and opposite. Arrows indicate alignment of the positive tangential axis in the 3D directional adhesion model.

problem and using linear programming methods. Just as described in Sections 4.1.1 and 4.1.2, this produces an optimal set of contact forces that are furthest away from violating any of the contact constraints given by the contact model.

4.2.2   Implications for Control of Foot Orientation

This analysis can be used to explore how foot orientation affects the overall stability of the three-dimensional model in Figure 4.8. However, the added orientation of each foot creates a relatively large parameter space to explore. Just as only a few cases needed consideration in the two-dimensional analysis, only a subset of the full range of foot orientations will be studied here. The restriction on the range of orientations is chosen to roughly match foot angles that are possible in climbing animals such as geckos. The orientations of the right feet (Contacts 1 and 4) are fixed to be equal

Parameter	Value
Model Parameters	
g	$9.8\mathrm{m/s}^2$
m	$50\mathrm{g}$
x_1, x_4	$5\mathrm{cm}$
x_2, x_3	$-5\mathrm{cm}$
y_1, y_2	$5\mathrm{cm}$
y_3, y_4	$-5\mathrm{cm}$
z_1, z_2, z_3, z_4	$-2\mathrm{cm}$
ϕ_1	$0° : -90°$
ϕ_2	$-\phi_1$
ϕ_3	$-\phi_4$
ϕ_4	$0° : -180°$
θ	$0° : 180°$
3D Directional Adhesion Parameters	
$\mu_1, \mu_2, \mu_3, \mu_4$	1.0
$\alpha_1^*, \alpha_2^*, \alpha_3^*, \alpha_4^*$	$30°$
$F_{1max}, F_{2max}, F_{3max}, F_{4max}$	$75\% \ \frac{mg}{\tan(\alpha_n^*)}$

Table 4.3: Model and contact parameters for three-dimensional internal force and stability analysis using three-dimensional directional adhesion to describe the foot-substrate interaction.

to and opposite of the orientations of the left feet (Contacts 2 and 3). The front right foot is rotated clockwise from pointing forward ($\phi_1 = 0$) to pointing to the right ($\phi_1 = -\pi/2$). The rear right foot is rotated clockwise from pointing forward ($\phi_4 = 0$) to pointing backward ($\phi_4 = -\pi$). The range of orientations considered for each foot is shown graphically in Figure 4.10.

The full set of geometric and contact model parameters is given in Table 4.3. Values are again chosen to approximately match typical characteristics of the Tokay gecko. Contact model parameters are chosen to roughly match data from the gecko adhesion system and from the synthetic directional adhesive tested in Chapter 3. The maximum adhesion at each foot is set to 75% of the body weight of the model. Optimal contact forces are solved for as a function of different inclination angles and different foot orientation angles.

Figures 4.11 and 4.12 show the stability margin function at inclination angles of

$0°$ and $90°$, respectively. On a horizontal surface, maximum stability is achieved by keeping the front feet pointing forward and reversing the rear feet. This behavior is identical to that of the two-dimensional analysis shown earlier. In this configuration the feet are able to simultaneously pull inward and increase the tangential loads in each contact frame, which in turn increases the maximum adhesion available at each contact. While adhesion is not required for stability on a horizontal surface, it nevertheless increases the system's tolerance to disturbance forces. Such strategies may be used by animals to resist forces imparted by wind or predators.

Unlike the two-dimensional case, when on a horizontal surface there is a continuous range of foot orientations over which the maximum stability margin is constant. Starting with just the rear feet reversed, as the rear foot angle decreases and the front foot angle increases by the same amount, the feet remain oppositely aligned and are still able to pull inward against each other. Continuing in this way, eventually all of the feet point sideways with the right feet pointing toward the right and the left feet pointing toward the left. On a horizontal surface, this configuration is identical to the starting configuration in which just the rear feet are reversed. The stability margin is equal and maximum at all these combinations of orientation angles as opposed to the two-dimensional case in which one discrete configuration clearly produces the best stability margin (since only discrete orientation configurations can be tested).

An optimal range of foot orientations all providing the same maximum stability margin is seen at all angles of inclination, not just for the horizontal case. However, the actual range changes as the inclination angle changes. For a vertical surface, Figure 4.12 shows how the optimal range has shifted and also widened, from the single curve seen in the horizontal case, to a patch in this case. On vertical surfaces, gravity can be used advantageously to increase adhesion by increasing the tangential forces, but only if the feet are in the proper configuration. Essentially, the force of gravity acts as a bias on the optimal foot orientation angles that tends to push them toward being aligned with the body frame. On a vertical surface, if $\phi = 0$ then gravity produces tangential forces on the contacts that increase the maximum adhesion at each contact. This causes the optimal front and rear orientation angles to shift toward $0°$ from their values for a horizontal surface.
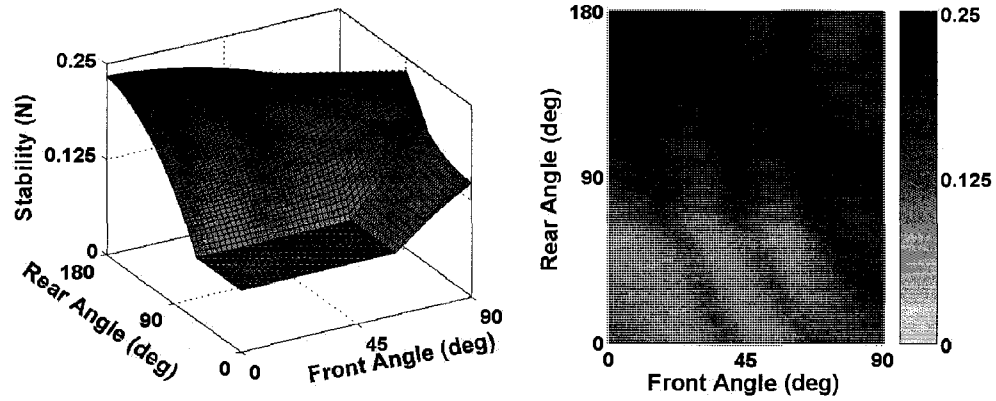
Figure 4.11: Stability margin on a horizontal surface ($\theta = 0°$) for the different combinations of foot orientations studied. A maximum stability of 0.23 is achieved over a range of front and rear orientation angles. Optimal orientation angles form a straight line that goes from the configuration in which the front angle is $0°$ and the rear angle is $180°$ to the configuration in which the front and rear angles are both $90°$.
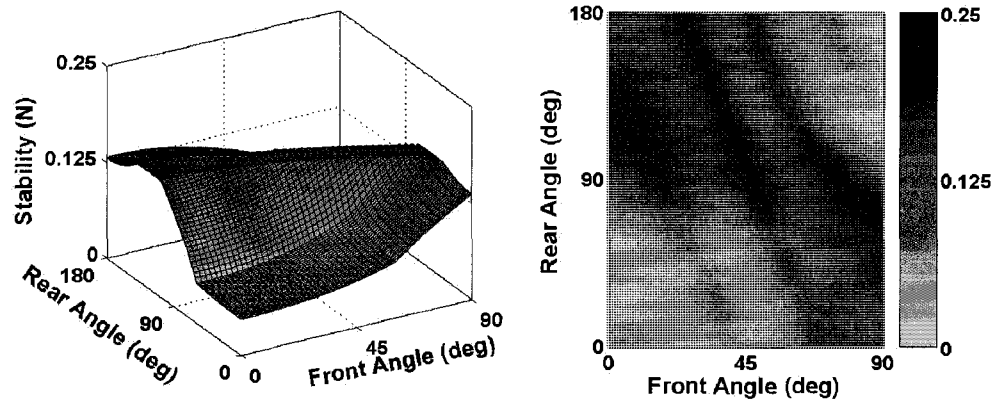
Figure 4.12: Stability margin on a vertical surface ($\theta = 90°$) for the different combinations of foot orientations studied. Maximum stability has decreased to 0.15 and the range of optimal orientation angles has changed compared to the horizontal case (Figure 4.11). Optimal orientation angles form a plateau rather than a line and both front and rear angles are shifted toward $0°$ compared to the horizontal case.
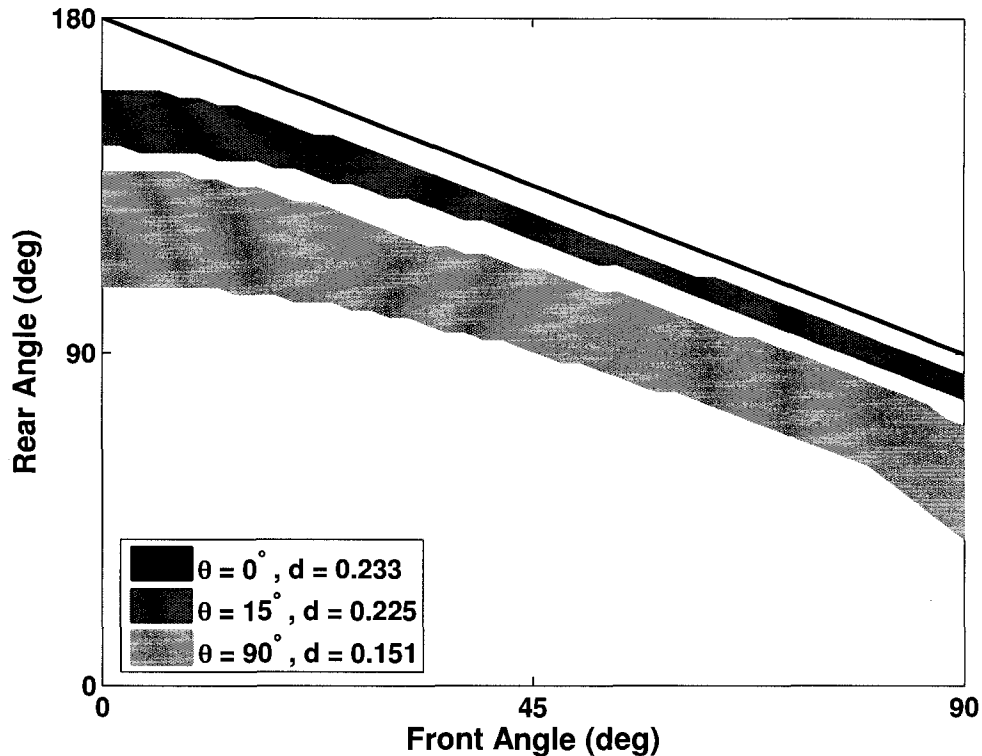
Figure 4.13: Optimal combinations of front and rear foot orientations for a few different inclination angles. As inclination angle increases, front and rear foot angles shift toward 0°. Optimal ranges are symmetric about an inclination of 90°, i.e. optimal patch shown for 15° is identical to optimal patch for 165° (not shown), although stability margins are lower.

Figure 4.13 better shows how the patches of maximum stability change as a function of the inclination angle. At each inclination angle, the same general relationship between optimal front and rear foot orientations is seen. As inclination angle increases from 0° to 90°, the foot angles are pushed toward an orientation in which the foot contacts are pointing forward (aligned with the body frame). Although not shown, further increases in inclination angle toward 180° result in the patches returning to their starting point at 0°, although the associated stability margins continue to decrease. In other words, the optimal foot orientation ranges are symmetric in shape about an inclination angle of 90° (i.e. the optimal foot orientations are identical at
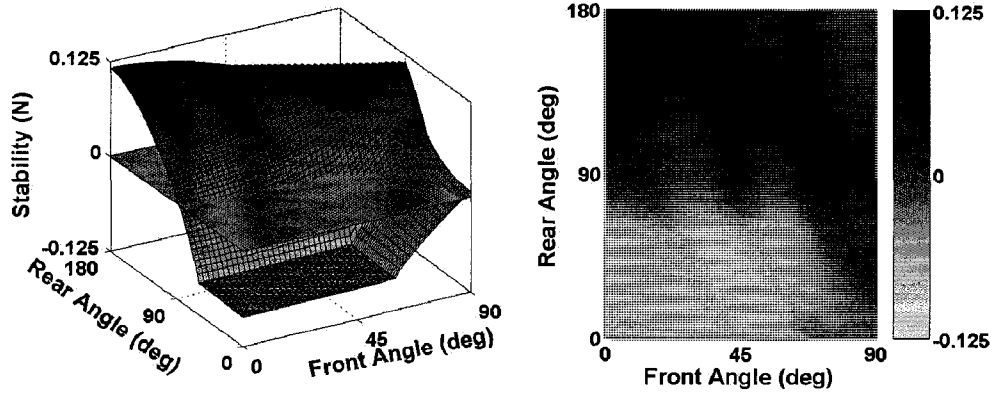
Figure 4.14: Stability margin on an overhanging or inverted surface ($\theta = 180°$) for the different combinations of foot orientations studied. Shape of the stability margin is identical to the horizontal case (Figure 4.11) and optimal orientation angles again form a line. However, overall stability has decreased uniformly across all combinations of front an rear orientation angles. Some orientation combinations are not able to produce positive stability margins.

inclines of 45° and 135°), but the stability margins monotonically decrease as the inclination angle goes from 0° to 180°.

Figures 4.11 and 4.14 show how the results are almost identical at inclination angles of 0° and 180°. The similarities at these inclination angles are produced because these configurations are almost identical. The only difference between these cases is that gravity is pulling in the opposite direction with respect to the body frame in the inverted case (180°). This causes a uniform decrease in the stability margin over all combinations of front and rear foot orientation. The shape of the stability margin function remains the same and is simply shifted downwards. On an inverted surface, some combinations of front and rear orientation angles do not produce positive stability margins. In these configurations the model is not able to achieve static stability on an overhanging surface.

These results are useful for a variety of different purposes. One is to increase our understanding of the climbing behavior seen in animals such as the gecko. It has been noted that geckos do indeed change their foot orientations depending on the inclination angle of the climbing surface and the direction in which they are
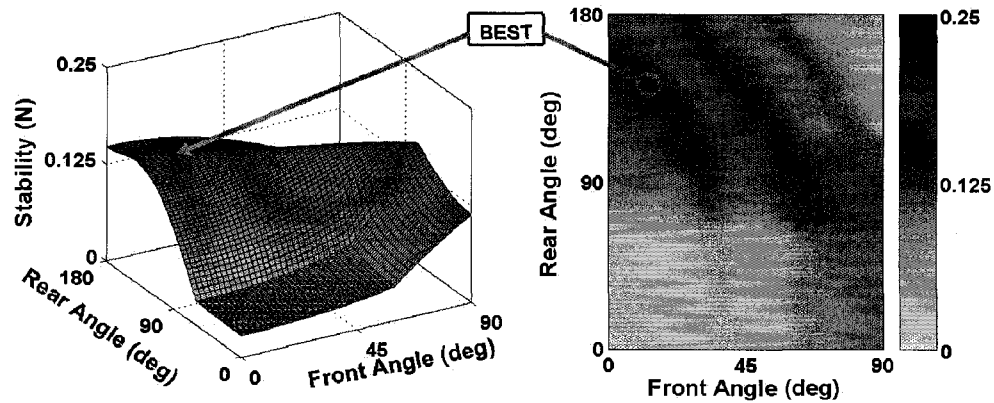
Figure 4.15: Mean stability margin over all inclines (0° to 180°) for the different combinations of foot orientations studied. Contour of maximum stability exists for a range of front and rear orientation angles. Best combination over all angles is chosen along this contour at a region where the drop off in stability away from the contour is minimized. This results in a front angle of approximately 15° and a rear angle of approximately 150°.

climbing (Personal Communications with Kellar Autumn, 2006). The results shown here qualitatively match experimental observations of geckos and explain why geckos may be varying their foot orientations.

These results can also aid in the design and/or control of a climbing robot. If foot orientations are controllable then it is possible to increase the climbing stability of a robot using a directional adhesive such as the DPS (Chapter 3). Depending on the current inclination angle, the foot orientations can be set to optimal combinations determined using the previous figures. Even when foot orientation must be fixed the results can be used to select a "good" overall foot orientation in the design of a robot. Figure 4.15 shows the stability margin averaged over the entire range of inclination angles (0° to 180°). Using these results, a set of foot orientations can be chosen that balances the stability requirements over the full range of inclines. In the example shown in Figure 4.15, this occurs along the contour of maximum stability at a region where the drop off away from the optimal contour is slowest, resulting in a front angle of approximately 15° and a rear angle of approximately 150°.

4.3 Other Considerations

The studies presented in this chapter consider only a subset of what can be explored using some of these techniques. There are variations to the model setup and analysis formulation that can be used to gain more insight into climbing. In particular, the above analysis can be extended to understand the potential role of a tail in climbing and the relationship between the safety margin and the magnitudes of the internal forces necessary to achieve that safety margin. The analysis also does not consider the problem of efficiently and accurately controlling the internal forces in order to achieve the predicted safety margins, which is an entire problem in and of itself.

4.3.1 Model and Analysis Variations

Both the two- and three-dimensional models in the preceding analysis are used to illustrate general principles involved when climbing with directional adhesion. The models are based on the geometric and climbing behaviors observed in geckos. As such, a tail was not included in either of the models shown in Figures 4.1 or 4.8. The tail of a gecko does not generally contact the surface during typical climbing; however, the gecko is known to use its tail when foot failures occur in order to regain good contact with the climbing surface (Personal Communications with Kellar Autumn, 2006). Inclusion of a tail has also been shown to increase the robustness of certain climbing robots [68].

A tail could be added to the models in Figures 4.1 or 4.8 by including another contact point behind the rear foot or feet. The tail is essentially treated as just another contact point. Its addition will lead to an increased number of internal forces; however, depending on whether or not the tail is actuated, some of those internal forces may need to be eliminated from the analysis if they cannot be controlled. Also, an appropriate contact model must be chosen for the tail, which may be as simple as a frictionless contact point.

In the case of a frictionless tail the static equilibrium requirements given in Equation 4.24 must be augmented by the normal force at the tail contact. Equation 4.26 becomes

$$W = \begin{bmatrix} & & & & 0 \\ \mathbf{I_3} & \mathbf{I_3} & \mathbf{I_3} & \mathbf{I_3} & 0 \\ & & & & 1 \\ & & & & y_5 \\ \mathbf{\hat{R}_1} & \mathbf{\hat{R}_2} & \mathbf{\hat{R}_3} & \mathbf{\hat{R}_4} & -x_5 \\ & & & & 0 \end{bmatrix}, \tag{4.42}$$

where x_5 and y_5 are the coordinates of the tail contact with respect to the center of mass. The vector of contact forces, $\mathbf{C}$, becomes 13×1 instead of 12×1 to account for the normal force at the tail, but $\mathbf{F}$ remains the same in Equation 4.25. There is one added degree-of-freedom in the nullspace of internal forces if the tail is actuated (i.e. the normal force of the tail can be controlled). Finally, the contact constraint for the tail is simply that the normal force be positive,

$$F'_{5N} \geq 0. \tag{4.43}$$

Equation 4.31 must be augmented by one row with Equation 4.43 to account for this contact constraint. The rest of the analysis continues as before.

An example of such an analysis including the tail is presented in [99], where the model parameters have been chosen to approximate a climbing robot instead of a gecko. While specific details in the results do change, the overall behaviors and trends predicted with and without the tail remain the same. Variations to the contact model at the tail can also be included by appropriately formulating the contact constraints and including the lateral and tangential forces in Equation 4.42 (e.g. if Coulomb friction is used to model the tail contact). In general, appropriate control of the internal forces requires that the analysis be adapted to the specific system in question.

There are also opportunities to explore variations in how the analysis is formulated. In the analysis presented, safety is maximized without regard to the magnitudes of internal forces required to achieve said safety. In both Nature and real robots, there is an energy penalty associated with sustained application of forces. Animals tend to employ a more "lazy" control system in which energy is only expended to maintain

a minimum safety margin rather than simply maximizing the safety margin.

Such factors can be added to the above analysis. In the two-dimensional case, with only one internal force, it is easy to simply search over all values of internal force to find the one that provides the desired safety margin. Results from such a formulation were presented in [11], where, when possible, the least-magnitude internal force was determined in order to produce a minimum safety margin. The three-dimensional case is more complicated because a brute-force search may be infeasible; however, there may be other ways of including the magnitudes of the internal forces in the cost function of the optimization.

4.3.2 Representing and Controlling Internal Forces

While not the primary focus of this work, accurate control of internal body forces is another complicated subject. The preceding analysis can calculate desired internal forces but is only useful if those forces can be applied at the contacts via actuator torques. Many researchers have tackled the subject of internal force control using various methods [73, 81, 82] based on the singular value decomposition formulation of the nullspace. A more physically meaningful formulation, termed the virtual linkage method, has been proposed as an alternative description of the nullspace and will be briefly discussed here [117, 118]. These various formulations have as yet only been applied to multi-fingered manipulation and multiple-robot cooperation but are equally suited to the control of a climbing robot.

The virtual linkage formulation differs from the analysis earlier in this chapter in that it directly specifies the internal forces in a physically meaningful way. In general, any set of basis vectors that span the nullspace of W can describe the internal forces of the system. The earlier analysis simply uses the singular value decomposition method for calculating the nullspace vectors since it is easily computed mathematically for any given configuration. However, such a set of basis vectors is often difficult to interpret in a physical sense.

The virtual linkage method represents the internal forces by using a set of prismatic and spherical actuators — the internal forces are specifically chosen as opposed to
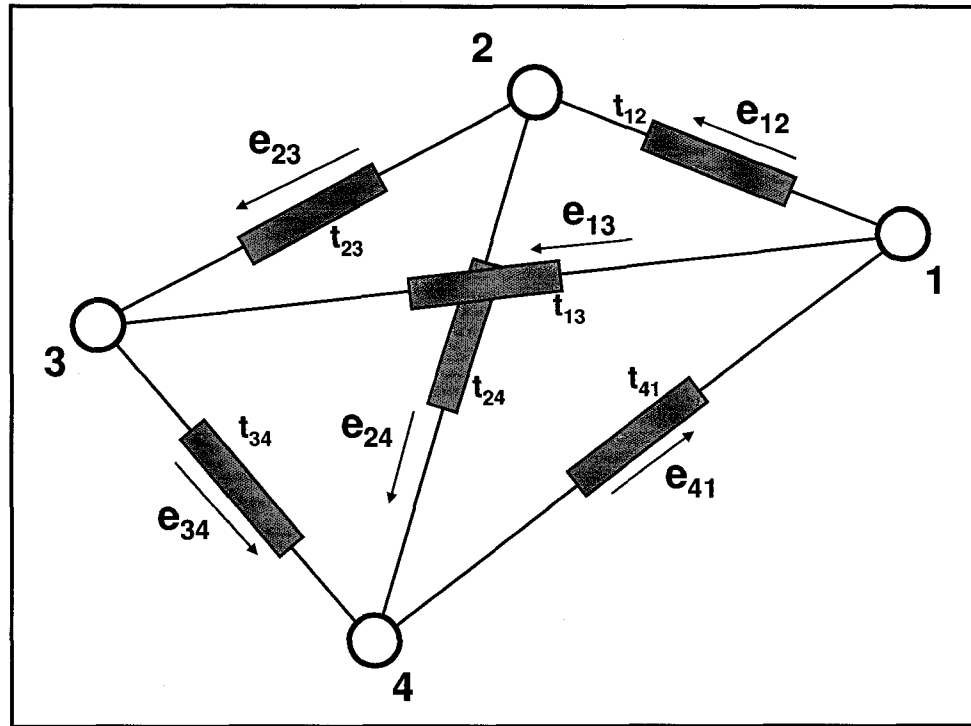
Figure 4.16: Virtual linkage representation of internal forces for the case of four non-coplanar contact points that cannot transmit moments. Each internal force is represented by a prismatic actuator with an associated tension. If moments can be transmitted by the contact points, a spherical actuator can be added at each contact point to represent the added internal moments. When four contact points are coplanar, the general method must be modified because the prismatic actuators shown will not span the entire nullspace (i.e. the tension in one of the prismatic actuators becomes dependent on the others and a different type of joint must be used to fully span the nullspace).

mathematically calculated. When no three of the contact points are collinear and no four of the contact points are coplanar and the contact points cannot transmit moments, the internal forces can be constructed by adding a prismatic joint between every combination of contact points. This is shown schematically in Figure 4.16 for the case of four contact points. When either three points are collinear or four points are coplanar it is slightly more difficult to directly specify an independent set of internal forces but the general framework still applies. When the contact points

can transmit moments, spherical joints can be introduced at each contact point to represent the internal moments of the system.

For the case of the two-dimensional model in Figure 4.1, using the singular value decomposition method to find the nullspace produces the same result as the virtual linkage method. Namely, the internal force can be represented by the tension applied by a prismatic joint connecting the front and rear contacts. The three-dimensional model in Figure 4.8 is slightly more complicated. For the general case when the four contact points are not coplanar, as shown in Figure 4.16, a set of basis vectors for the nullspace with a more physical interpretation is

$$
\mathbf{E} = \begin{bmatrix} -\mathbf{e}_{12} & 0 & 0 & \mathbf{e}_{41} & -\mathbf{e}_{13} & 0 \\ \mathbf{e}_{12} & -\mathbf{e}_{23} & 0 & 0 & 0 & -\mathbf{e}_{24} \\ 0 & \mathbf{e}_{23} & -\mathbf{e}_{34} & 0 & \mathbf{e}_{13} & 0 \\ 0 & 0 & \mathbf{e}_{34} & -\mathbf{e}_{41} & 0 & \mathbf{e}_{24} \end{bmatrix},
\tag{4.44}
$$

where $\mathbf{e}_{ij}$ is the unit vector from contact i to contact j. Using this representation, the tension between each pair of contacts can be directly specified. The contact forces resulting from these internal forces can be given as

$$
\mathbf{C_h} = \mathbf{E}t,
\tag{4.45}
$$

where t is the vector of tensions between different combinations of contacts. Finally, the entire system can be described using

$$
\mathbf{C} = \begin{bmatrix} \mathbf{W}^\dagger & \mathbf{E} \end{bmatrix} \begin{bmatrix} -\mathbf{F} \\ t \end{bmatrix}.
\tag{4.46}
$$

The block matrix $\begin{bmatrix} \mathbf{W}^\dagger & \mathbf{E} \end{bmatrix}$ is now a 12×12 square matrix. Equation 4.46 is useful for relating the forces at each contact to the internal forces and the resultant force and moment of the system. In the case when the four contact points are coplanar, $\mathbf{E}$ loses rank but the pseudo-inverse can still be used to calculate internal tensions (t) and the resultant ($\mathbf{F}$) from the individual contact forces.

Formulating the nullspace vectors using this method allows the internal forces

to be represented by traditional prismatic joints, whereas using the singular value decomposition method results in a generalized set of basis vectors that cannot be directly correlated to any kind of traditional robotic joints. The earlier analysis can still be applied using this representation of the internal forces by merely replacing $\mathbf{C_h}$ with its new representation in terms of $\mathbf{E}$ and t. The final results for the stability and the contact forces will be the same; however, the internal forces returned by the optimization will have a more direct meaning.

While direct physical interpretation of the internal forces is useful, the main advantage to using the virtual linkage representation involves control. Because the virtual linkage formulation can represent internal forces as prismatic or spherical joints, they can be treated in the same control framework as other joints in the manipulator. In particular, this allows force control of the internal forces to be decoupled from position control of an operational point on the manipulator.

Decoupling of the internal force control from the position control is particularly important when dynamics are involved. In the static equilibrium case, a good feed-forward controller can directly apply the joint torques necessary to achieve the optimal internal forces. However, in the case of poor torque control or when dynamic effects become large, internal force control can lead to undesirable motions, or vice versa, large inertial forces can lead to improper control of the internal forces. Decoupling the force control from the position control in a unified framework can provide a better closed-loop response of the system.

4.4 Summary

This chapter has presented a general procedure for analyzing the static equilibrium of simple models of climbing animals or robots. Two- or three-dimensional climbers are reduced to a center of mass and a set of contact points. The forces at the contact points and any external forces such as gravity must sum to zero to maintain static equilibrium. The systems have more unknowns than equations. The extra degrees-of-freedom correspond to internal body forces that the feet can exert and create an infinite solution space.

The stability requirements of the contacts constrain the solution space by imposing inequality constraints on the forces at each contact. In the formulation presented, the only requirement on the contact constraints is that they are linear in the contact forces. The problem of finding a stable solution is reformulated into an optimization problem in which the best set of internal forces is found. The optimal set of internal forces is that which maximizes the distance from violating any of the contact constraints given by the contact model for each foot. Optimal internal forces are used to reconstruct the optimal contact forces, and using various control methodologies can themselves be controlled. These forces and the associated stability margin can be studied as a function of the various geometric parameters of the model as well as for different types of contact models operating at the foot-substrate interfaces.

The stability and internal force of the two-dimensional model was studied at different angles of an inclined plane. The contacts were assumed to be governed by Coulomb friction, Embedded Cone, or the Frictional Adhesion contact model. The Coulomb friction model showed that stability is only possible up to a finite angle less than 90° when the contact model does not contain any adhesion. The Embedded Cone and Frictional Adhesion models highlighted the differences between isotropic and anisotropic contacts. While both these contact models are able to produce comparable levels of stability using comparable levels of maximum adhesion, they do so via opposite strategies for the internal force. The Embedded Cone model predicts that the rear foot should bear more of the net tangential load and that the model should "push" itself up a wall. In contrast, the Frictional Adhesion model predicts that the model's front foot should bear more shear and "pull" itself up a wall. The results from the two-dimensional analysis qualitatively match published results for climbing geckos [13].

The data presented in Chapter 3 was used to construct a three-dimensional directional adhesion limit surface for use in the three-dimensional analysis. The results for both the two- and three-dimensional analyses illustrated an important characteristic that must considered when dealing with an anisotropic contact model — orientation. In both the 2D Frictional Adhesion model and the 3D directional adhesion model, it was necessary to introduce the orientation of the contact as an extra parameter. The
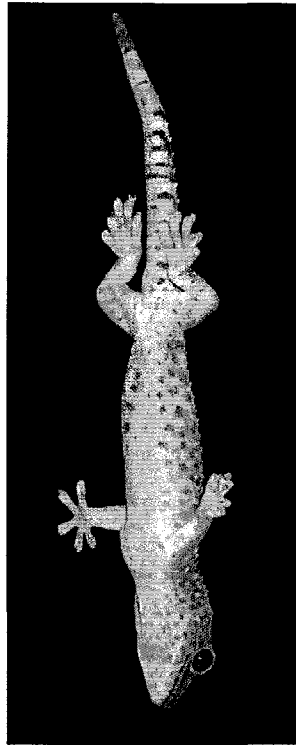
Figure 4.17: Picture of a gecko climbing downward (head first) with both feet reversed. Foot reversal allows the gecko to use gravity to load the contacts in a way that increases adhesion. These effects can be studied using the analytical techniques presented in this chapter. Image reproduced with permission [9].

results showed that the orientation of the foot contacts can greatly affect the level of stability that can be achieved and the associated optimal internal and contact forces.

When dealing with models such as Frictional Adhesion, it is beneficial to orient the contacts with gravity when on vertical surfaces. This will cause gravity to increase stability by passively loading the contacts in a way that increases adhesion. However, other issues arise due to the anisotropy. When on inverted surfaces, the Frictional Adhesion model requires the rear foot to reverse so that internal forces can generate the shear forces required for adhesion. These results qualitatively match observations of geckos climbing surfaces of various inclinations. Essentially, the anisotropy of the model provides controllability but then necessitates control. This discussion is epitomized in Figure 4.17. A gecko that is climbing downward (head first) has reversed

both of its rear feet in order to properly load its adhesive structures, highlighting the importance of proper force control and foot orientation strategies when using directional adhesion.

Chapter 5

Conclusion

Climbing robots have the potential to perform a wide variety of useful tasks. This thesis explored the use of contact modeling and directional adhesion to gain insights into fundamental climbing principles, using the gecko lizard as a source of inspiration. These principles can be applied in the design and control of climbing robots in order to improve their performance.

5.1 Summary

The importance of the interaction between the feet and the climbing substrate was discussed. This interaction dictates the forces that can be applied at the foot-substrate interface without causing failure of the contact through either sliding or pulloff. The force limits associated with a contact model can be graphically described in a concise manner by using the concept of a limit surface.

Different adhesive models were presented, including the JKR, Kendall peel, and Frictional Adhesion models. The benefits of a directional adhesive, such as the gecko adhesion system, for climbing were compared to other symmetric adhesion models. The gecko's directional adhesive enables adhesion to be controlled and enables smooth attachment and detachment of the adhesive from the substrate. These aspects of the gecko adhesion system are highly desirable for climbing.

An experimental setup able to test directional adhesion was described. Non-directional adhesives have previously only been tested in the normal direction. These tests generally consist of preloading the sample and pulling the sample away from the substrate using motions and applying forces only in the normal direction. This one-dimensional characterization of adhesion is insufficient for a directional adhesive.

Procedures were developed to apply motions and measure forces in three directions — the normal axis and the two parallel axes. Like previous tests, these tests also consist of applying preloads and then pulling a sample away from a substrate, but do so in three dimensions. This allows construction of three-dimensional experimental limit surfaces and characterization of the directionality of an adhesive.

A new synthetic directional adhesive, based roughly on the gecko's adhesive structures, was described and results from testing this adhesive were presented. The new adhesive is indeed directional, exhibiting adhesion when pulled in one direction and only friction when pulled in the opposite direction. The affects of various experimental parameters were explored, including preload magnitude, preload trajectory, and pulloff speed. The synthetic adhesive exhibited approximately the same behavior as the gecko adhesion system, more or less matching the Frictional Adhesion model.

Simple two- and three-dimensional climbing models were used to study clinging performance. An analysis was formulated that uses internal forces to maximize the stability of the system. Different contact models lead to different force distribution strategies. When the contact is described by the Frictional Adhesion model, the results qualitatively match those seen for the gecko when climbing. This analysis highlighted the differences between directional and non-directional adhesives and, in particular, the importance of proper force balancing and foot orientation when using directional adhesion.

5.2 Future Work

The synthetic adhesive (Directional Polymer Stalks) presented in Chapter 3 is quite simple when compared to the gecko's adhesive structures (Chapter 2). Creating better gecko-inspired adhesives is and will continue to be an ongoing active area of research.

The DPS use a relatively soft bulk material and only one level of hierarchy to achieve good conformation to a substrate. Using stiffer bulk materials can enable the adhesive to resist contamination; however, this also requires more complex micro-structures to achieve the same level of conformation to a surface. Incorporating multiple levels of hierarchy, reducing feature sizes, and increasing material stiffness are all potential avenues for improving the current generation of DPS.

Improvements to the experimental system for testing directional adhesives can also be performed. The main focus of the setup described in Chapter 3 was to test an adhesive in three directions instead of just the normal direction. Because of the relatively large feature sizes of the DPS, positioning resolution on the order of tens of micrometers and alignment by visual inspection were adequate for testing purposes. New synthetic adhesives will most likely require smaller positioning resolution and better methods for alignment of flat samples to flat substrates.

The experiments described in Chapter 3 are only a small subset of the variety of experiments that can be performed. They highlight the main aspects of directional adhesion, but there are subtle characteristics that can be further explored. Parameters such as the dwell time, which was held at zero for all experiments described, between preload and pulloff phases can be varied. The relationship between speed and adhesion can be further explored in order to answer the question of whether or not a true static limit exists for a particular adhesive. This could be done by applying step motions at the contact interface instead of continuous ones. And of course, testing different geometries of the DPS or DPS made with different materials can lead to better directional adhesives.

Finally, while research has discovered much about the gecko adhesion system, there is still much that can be learned. It is currently unknown how lateral forces affect the adhesion of the gecko's foot structures. The analytical techniques presented in Chapter 4 can be used to better understand the climbing behavior of the gecko. Qualitatively, the simple models are able to predict some of the forces seen in climbing geckos. However, few if any experiments have been performed that look at the foot orientation of the gecko in a quantitative manner.

All of these avenues of research can further our understanding of climbing and can

lead to better climbing robots.

5.3 Final Thoughts

This thesis has provided the background and an experimental framework for understanding and studying directional adhesion in regards to climbing. An example directional adhesive was tested in order to illustrate various characteristics of directional adhesion. These tests also highlighted some of the added difficulties that arise when testing directional adhesives as opposed to non-directional adhesives. Models of directional adhesion can be used in simple analyses of climbing robots on inclined planes. These analyses reveal important differences between directional and non-directional adhesives. They are also able to qualitatively predict some of the behaviors seen in climbing geckos.

Directional adhesion provides mechanisms for controlling the adhesion at a contact. It enables smooth attachment with small attachment forces and effortless detachment under the proper conditions. However, in providing control, directional adhesion then necessitates control. Proper force balancing strategies must be used to take advantage of directional adhesion, and foot orientation also plays a crucial role in determining overall stability. Nevertheless, with proper understanding, directional adhesion can increase the robustness and performance of climbing robots.

Appendix A

JKR Limit Surface Derivation

This Appendix will outline the derivation of the Johnson-Kendall-Roberts (JKR) Limit Surface. The derivation begins with two assumptions: 1) any applied tangential loads do not affect the area of the contact given by the JKR model, and 2) the maximum tangential force that can be sustained is given by

$$F_T = \sigma_T \pi a^2, \tag{A.1}$$

where F_T is the maximum tangential force, σ_T is the shear strength of the contact interface, and a is the radius of the contact circle given by the JKR model. From the JKR model [61], the contact circle radius is given by

$$a^3 = \frac{R}{K} \left(P + 3\gamma\pi R + \sqrt{6\gamma\pi RP + (3\gamma\pi R)^2} \right), \tag{A.2}$$

where R is the equivalent radius, K is the equivalent stiffness, and γ is the surface energy of the two solids. The equivalent radius, R, is given by

$$\frac{1}{R} = \frac{1}{R_1} + \frac{1}{R_2}, \tag{A.3}$$

where R_1 and R_2 are the radii of the two contacting spheres. The equivalent stiffness, K, is given by

$$K = \frac{4}{3}\left(\frac{1 - \nu_1{}^2}{E_1} + \frac{1 - \nu_2{}^2}{E_2}\right)^{-1}, \tag{A.4}$$

where ν_1 and ν_2 are the Poisson's ratios for the two solids and E_1 and E_2 are the Moduli of Elasticity for the two solids. The equivalent stiffness in JKR theory, K, is related to the equivalent stiffness in Hertz theory, E^*, by

$$K = \frac{4}{3}E^*. \tag{A.5}$$

Finally, P, the applied normal load in the JKR model, can be simply replaced by F_N, also noting that the lower bound on F_N is given by

$$F_N = P \geq -\frac{3}{2}\gamma\pi R. \tag{A.6}$$

The previous sets of equations can then be normalized and solved to provide a relationship between F_N and F_T. First, the lower adhesive pulloff limit given in Eq. A.6 is normalizes such that

$$F_N^* = -\frac{3}{2}\gamma\pi R, \tag{A.7}$$

where F_N^* is the arbitrary adhesive pulloff limit. This allows calculation of the following constant

$$C_1 = -\frac{2}{3}F_N^* = \gamma\pi R. \tag{A.8}$$

Equation A.2 can then be written as

$$a = \left(\frac{R}{K}\left(F_N + 3C_1 + \sqrt{6C_1F_N + 9C_1{}^2}\right)\right)^{\frac{1}{3}}. \tag{A.9}$$

Next, the maximum tangential force at zero applied normal load can be normalized to F_T^*, an arbitrary shear limit. Setting $F_N = 0$, Eq. A.9 simplifies to

$$a_0 = \left(6\frac{R}{K}C_1\right)^{\frac{1}{3}}. \tag{A.10}$$
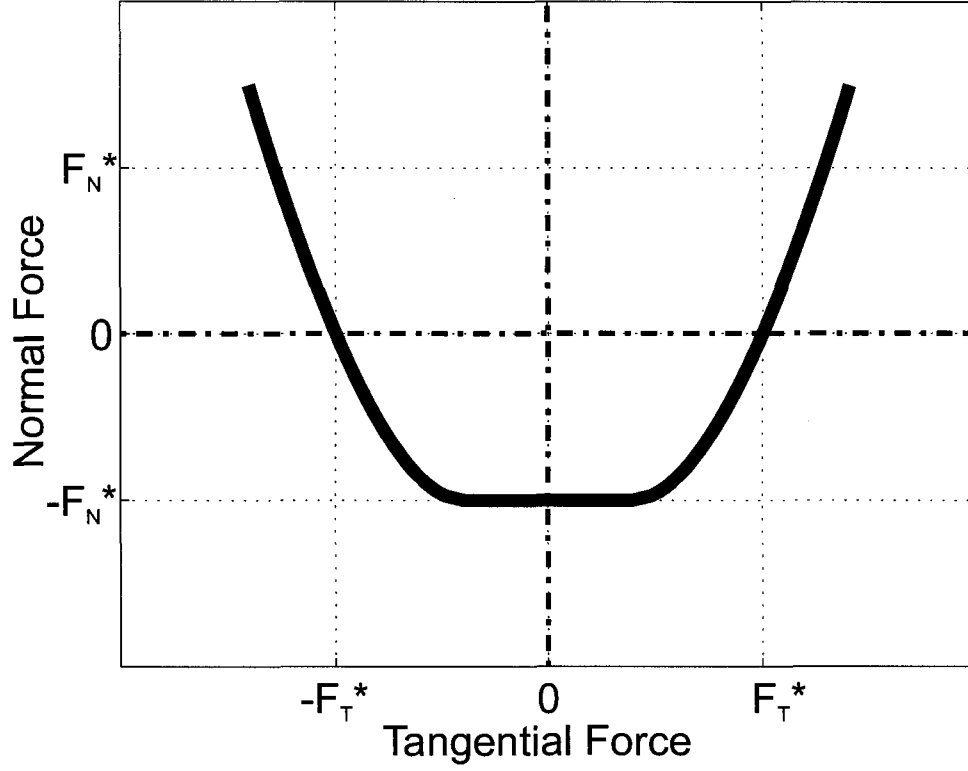
Figure A.1: JKR Model Limit Surface. Results are shown in terms of F_N^* and F_T^* based on Eq. A.14

This can then be substituted back into Eq. A.1 to give

$$F_T^* = \sigma \pi a_0^{\ 2}$$

$$F_T^* = \sigma \pi \left(6 \frac{R}{K} C_1 \right)^{\frac{2}{3}}$$

$$F_T^* = \left[\sigma \pi \left(\frac{R}{K} \right)^{\frac{2}{3}} \right] (6 C_1)^{\frac{2}{3}}.$$

(A.11)

The following constant can then be introduced as

$$C_2 = (6 C_1)^{-\frac{2}{3}} F_T^* = \sigma \pi \left(\frac{R}{K} \right)^{\frac{2}{3}}.$$

(A.12)

Finally, Eq. A.1 can be written and simplified as

$$F_T = \sigma \pi a^2$$

$$F_T = \sigma \pi \left(\frac{R}{K} \left(F_N + 3C_1 + \sqrt{6C_1 F_N + 9C_1{}^2} \right) \right)^{\frac{2}{3}} \tag{A.13}$$

$$F_T = \left[\sigma \pi \left(\frac{R}{K} \right)^{\frac{2}{3}} \right] \left(F_N + 3C_1 + \sqrt{6C_1 F_N + 9C_1{}^2} \right)^{\frac{2}{3}}$$

resulting in a final relationship between F_T and F_N given by

$$F_T = C_2 \left(F_N + 3C_1 + \sqrt{6C_1 F_N + 9C_1{}^2} \right)^{\frac{2}{3}}, \tag{A.14}$$

where $C_1 = -\frac{2}{3} F_N^*$ and $C_2 = 6 C_1^{\frac{2}{3}} F_T^*$. Equation A.14 can be plotted in terms of F_N^* and F_T^*. This is shown in Fig. A.1.

Bibliography

[1] A. Aasbeck, S. Kim, M. Cutkosky, W. Provancher, and M. Lanzetta. Scaling hard vertical surfaces with compliant microspine arrays. *International Journal of Robotics Research*, 25(12):1165–1179, 2006.

[2] B. Aksak, M. Murphy, and M. Sitti. Adhesion of biologically inspired vertical and angle polymer microfiber arrays. *Langmuir*, 23(6):3322–3332, 2007.

[3] Guillaume Amontons. De la reistance causee dans les machines. *Memoires de l'Academie des Sciences*, pages 203–222, 1699.

[4] Aristotle. *Historia Animalium*, volume 9. Clarendon, Oxford, 1918.

[5] B. Armstrong. *Control of Machines with Friction*. Kluwer Academic Publishers, Boston, MA, 1991.

[6] B. Armstrong, P. Dupont, and C. Canudas de Wit. A survey of models, analysis tools and compensation methods for the control of machines with friction. *Automatica*, 30(7):1083–1138, 1994.

[7] E. Arzt, S. Gorb, and R. Spolenak. From micro to nano contacts in biological attachment devices. *Proceedings of the National Academy of Sciences of the United States of America*, 100(9):10603–10606, 2003.

[8] K. Autumn. Properties, principles, and parameters of the gecko adhesive system. In A. Smith and J. Callow, editors, *Biological Adhesives*. Springer-Verlag, Berlin Heidelberg, 2006.

[9] K. Autumn. Autumnlab images, www.lclark.edu, 2007.

[10] K. Autumn, M. Buehler, M. Cutkosky, R. Fearing, R. Full, D. Goldman, R. Groff, W. Provancher, A. Rizzi, U. Saranli, A. Saunders, and D. Koditschek. Robotics in scansorial environments. *Proceedings of the SPIE*, 5804:291–302, 2005.

[11] K. Autumn, A. Dittmore, D. Santos, M. Spenko, and M. Cutkosky. Frictional adhesion: a new angle on gecko attachment. *Journal of Experimental Biology*, 209(18):3569–3579, 2006.

[12] K. Autumn and W. Hansen. Ultrahydrophobicity indicates a non-adhesive default state in gecko setae. *Journal of Comparative Physiology A: Neuroethology, Sensory, Neural, and Behavioral Physiology*, 192(11):1205–1212, 2006.

[13] K. Autumn, S. T. Hsieh, D. M. Dudek, J. Chen, C. Chitaphan, and R. J. Full. Dynamics of geckos running vertically. *Journal of Experimental Biology*, 209(2):260–272, 2006.

[14] K. Autumn, Y. Liang, S. Hsieh, W. Zesch, W.-P. Chan, T. Kenny, R. Fearing, and R. Full. Adhesive force of a single gecko foot-hair. *Nature*, 405(6787):681–685, 2000.

[15] K. Autumn, C. Majidi, R. Groff, and R. Fearing. Effective elastic modulus of isolated gecko setal arrays. *Journal of Experimental Biology*, 209:3558–3568, 2006.

[16] K. Autumn and A. Peattie. Mechanisms of adhesion in geckos. *Integrative and Comparative Biology*, 42:1081–1090, 2002.

[17] K. Autumn, M. Sitti, Y. Liang, A. Peattie, W. Hansen, S. Sponberg, T. Kenny, R. Fearing, J. Israelachvili, and R. Full. Evidence for van der waals adhesion in gecko setae. *Proceedings of the National Academy of Sciences of the United States of America*, 99(19):12252–12256, 2002.

[18] B. Bhushan. Contact mechanics of rough surfaces in tribology: multiple asperity contact. *Tribology Letters*, 4(1):1–35, 1998.

[19] B. Bhushan. *Introduction to Tribology*. John Wiley and Sons, New York, 2002.

[20] B. Bhushan, A. G. Peressadko, and T. W. Kim. Adhesion analysis of two-level hierarchical morphology in natural attachment systems for 'smart adhesion'. *Journal of Adhesion Science and Technology*, 20(13):1475–1491, 2006.

[21] B. Bhushan and R. A. Sayer. Surface characterization and friction of a bio-inspired reversible adhesive tape. *Microsystem Technologies*, 13(1):71–78, 2006.

[22] A. Bicchi and V. Kumar. Robotic grasping and contact: A review. In *IEEE International Conference on Robotics and Automation*, pages 348–353, 2000.

[23] F.P. Bowden and D. Tabor. The area of contact between stationary and between moving surfaces. *Proceedings of the Royal Society of London. Series A, Mathematical and Physical Sciences*, 169(938):391–413, 1939.

[24] T. Bretl. Motion planning of multi-limbed robots subject to equilibrium constraints: The free-climbing robot problem. *International Journal of Robotics Research*, 25(4):317–342, 2006.

[25] T. Bretl, S. Rock, and J.-C. Latombe. Motion planning for a three-limbed climbing robot in vertical natural terrain. In *IEEE International Conference on Robotics and Automation*, pages 2946–2953, Taipei, Taiwan, 2003.

[26] M. Buss, H. Hashimoto, and J. B. Moore. Dextrous hand grasping force optimization. *IEEE Transactions on Robotics and Automation*, 12(3):406–418, 1996.

[27] M. Cartmill. Climbing. In M. Hildebrand, D. Bramble, K. Liem, and D. Wake, editors, *Functional Vertebrate Morphology*, pages 73–88. Harvard University Press, Cambridge, MA, 1985.

[28] S. Chen and T. Wang. General solution to two-dimensional nonslipping jkr model with a pulling force in an arbitrary direction. *Journal of Colloid and Interface Science*, 302(1):363–369, 2006.

[29] Charles-Augustin Coulomb. Theorie des machines simples. *Memoires de Mathematique et de Physique de l'Academie des Sciences*, pages 161–331, 1785.

[30] A. J. Crosby, M. Hageman, and A. Duncan. Controlling polymer adhesion with "pancakes". *Langmuir*, 21(25):11738–11743, 2005.

[31] A. J. Crosby and K. R. Shull. Adhesive failure analysis of pressure-sensitive adhesives. *Journal of Polymer Science. Part B, Polymer Physics*, 37(24):3455–3472, 1999.

[32] C.A. Dahlquist. Pressure-sensitive adhesives. In R.L. Patrick, editor, *Treatise on adhesion and adhesives*, volume 2, pages 219–260. Marcel Dekker, New York, 1969.

[33] W.-D. Dellit. Zur anatomie und physiologie der geckozehe. *Z. Naturwiss*, 68:613–656, 1934.

[34] B.V. Derjaguin. *Kolloid Z.*, 69:155, 1934.

[35] B.V. Derjaguin, V.M. Muller, and YU.P. Toporov. Effect of contact deformations on the adhesion of particles. *Journal of Colloid and Interface Science*, 53(2):314–326, 1975.

[36] D. Dowson. *History of Tribology*. Professional Engineering Publishing Limited, London, 2nd edition, 1998.

[37] K. Fuller and D. Tabor. The effect of surface roughness on the adhesion of elastic solids. *Proceedings of the Royal Society of London. Series A, Mathematical and Physical Sciences*, 345(1642):327–342, 1975.

[38] H. Gao, X. Wang, H. Yao, S. Gorb, and E. Arzt. Mechanics of hierarchical adhesion structures of geckos. *Mechanics of Materials*, 37(2-3):275–285, 2005.

[39] H. Gao and H. Yao. Shape insensitive optimal adhesion of nanoscale fibrillar structures. *Proceedings of the National Academy of Sciences of the United States of America*, 101(21):7851–7856, 2004.

[40] A. K. Geim, S. V. Dubonos, I. V. Grigorieva, K. S. Novoselov, A. A. Zhukov, and S. YU. Shapoval. Microfabricated adhesive mimicking gecko foot-hair. *Nature Materials*, 2(7):461–463, 2003.

[41] B. Geisler, A. Dittmore, B. Gallery, T. Stratton, R. Fearing, and K. Autumn. Deformation of isolated gecko setal arrays: bending or buckling? 2. kinetics. In *Society for Integrative and Comparative Biology*, San Diego, 2005.

[42] N. J. Glassmaker, A. Jagota, C.-Y. Hui, and J. Kim. Design of biomimetic fibrillar interfaces: 1. making contact. *Journal of The Royal Society Interface*, 1(1):23–33, 2004.

[43] S. Gorb, M. Varenberg, A. Peressadko, and J. Tuma. Biomimetic mushroom-shaped fibrillar adhesive microstructure. *Journal of The Royal Society Interface*, 4(13):271–275, 2007.

[44] S. Goyal, A. Ruina, and J. Papadopoulos. Limit surface and moment function descriptions of planar sliding. In *IEEE Internaional Conference on Robotics and Automation*, Scottsdale, AZ, 1989.

[45] S. Goyal, A. Ruina, and J. Papadopoulos. Planar sliding with dry friction, part 1. limit surface and moment function. *Wear*, 143:207–330, 1991.

[46] J. Grieco, M. Prieto, M. Armada, and P. Santos. A six-legged climbing robot for high payloads. In *IEEE International Conference on Control Applications*, Trieste, Italy, 1998.

[47] W. Hansen and K. Autumn. Evidence for self-cleaning in gecko setae. *Proceedings of the National Academy of Sciences of the United States of America*, 102(2):385–389, 2005.

[48] F. Henkel and W. Schmidt. *Geckos*. Andreas S. Brahm, Germany, 2003.

[49] H. Hertz. Uber die beruhrung fester elastische korper und uber die harte (on the contact of rigid elastic solids and on hardness). *Verhandlungen des Vereins zur Beforderung des Gewerbefleisses*, 1882.

[50] U. Hiller. Untersuchungen zum feinbau und zur funktion der haftborsten von reptilien. *Zoomorphology*, 62(4):307–362, 1968.

[51] K. Hirai, M. Hirose, Y. Haikawa, and T. Takenaka. The development of honda humanoid robot. In *IEEE International Conference on Robotics and Automation*, Leuven, Belgium, 1998.

[52] S. Hirai and H. Asada. Kinematics and statics of manipulation using the theory of polyhedral convex cones. *The International Journal of Robotics Research*, 12(5):434–447, 1993.

[53] D. W. Hong and R. J. Cipra. Optimal force distribution for tethered climbing robots in unstructured environments. In *ASME Design and Engineering Technical Conference and Computers and Information in Engineering Conference*, Montreal, Canada, 2002.

[54] D. W. Hong and R. J. Cipra. Visualization of the contact force solution space for multi-limbed robots. *Journal of Mechanical Design*, 128:295–302, 2006.

[55] C.-Y. Hui, N. J. Glassmaker, T. Tang, and A. Jagota. Design of biomimetic fibrillar interfaces: 2. mechanics of enhanced adhesion. *Journal of The Royal Society Interface*, 1(1):35–48, 2004.

[56] J. Israelachvili. *Intermolecular and Surface Forces*. Academic Press, New York, 1992.

[57] H. E. Jeong, S. H. Lee, P. Kim, and K. Y. Suh. Stretched polymer nanohairs by nanodrawing. *Nano Letters*, 6(7):1508–1513, 2006.

[58] K.L. Johnson. *Contact Mechanics*. Cambridge University Press, 1987.

[59] K.L. Johnson. Continuum mechanics modeling of adhesion and friction. *Langmuir*, 12:4510–4513, 1996.

[60] K.L. Johnson. Adhesion and friction between a smooth elastic spherical asperity and a plane surface. *Proc. of the Royal Society A: Mathematical, Physical and Engineering Sciences*, 453(1956):163–179, 1997.

[61] K.L. Johnson, K. Kendall, and A.D. Roberts. Surface energy and the contact of elastic solids. *Proc. of the Royal Society A: Mathematical, Physical and Engineering Sciences*, 324(1558):301–313, 1971.

[62] I. Kao and M. Cutkosky. Quasistatic manipulation with compliance and sliding. *International Journal of Robotics Research*, 11(1):20–40, 1992.

[63] K. Kendall. Thin-film peeling - the elastic term. *Journal of Physics D: Applied Physics*, 8(13):1449–1452, 1975.

[64] K. Kendall. *Molecular Adhesion and its Applications*. Kluwer Academic Publishers, New York, 2001.

[65] J. Kerr and B. Roth. Analysis of multifingered hands. *The International Journal of Robotics Research*, 4(4):3–17, 1986.

[66] D. S. Kim, H. S. Lee, J. Lee, S. Kim, K.-H. Lee, W. Moon, and T. H. Kwon. Replication of high-aspec-ratio nanopillar array for biomimetic gecko foot-hair prototype by uv nano embossing with anodic aluminum oxide mold. *Microsystem Technologies*, 13(5-6):601–606, 2007.

[67] S. Kim, A. Aasbeck, M. Cutkosky, and W. Provancher. Spinybotii: Climbing hard walls with compliant microspines. In *IEEE International Conference on Advanced Robotics*, Seattle, WA, USA, 2005.

[68] S. Kim, J. Clark, and M. Cutkosky. isprawl: Design and tuning for high-speed autonomous open-loop running. *International Journal of Robotics Research*, 25(9):903–912, 2006.

[69] S. Kim and M. Sitti. Biologically inspired polymer microfibers with spatulae tips as repeatable fibrillar adheisves. *Applied Physics Letters*, 89(26):261911, 2006.

[70] S. Kim, M. Spenko, S. Trujillo, B. Heyneman, V. Mattoli, and M. Cutkosky. Whole body adhesion: hierarchical, directional and distributed control of adhesive forces for a climbing robot. In *IEEE International Conference on Robotics and Automation*, pages 1268–1273, Rome, Italy, 2007.

[71] T. W. Kim and B. Bhushan. Adhesion analysis of multi-level hierarchical attachment system contacting with a rough surface. *Journal of Adhesion Science and Technology*, 21(1):1–20, 2007.

[72] C. A. Klein and S. Kittivatcharapong. Optimal force distribution for the legs of a walking machine with friction cone constraints. *IEEE Transactions on Robotics and Automation*, 6(1):73–85, 1990.

[73] V. Kumar and K. Waldron. Force distribution in closed kinematic chains. *IEEE Journal of Robotics and Automation*, 4(6):657–664, 1988.

[74] V. Kumar and K. Waldron. Suboptimal algorithms for force distribution in multifingered grippers. *IEEE Transactions on Robotics and Automation*, 5(4):491–498, 1989.

[75] V. Kumar and K. Waldron. Force distribution in walking vehicles. *Journal of Mechanical Design*, 112:90–99, 1990.

[76] J. E. Lennard-Jones. Cohesion. *Proceedings of the Physical Society*, 43(5):461–482, 1931.

[77] R. Ling. Tokay gecko, 1998.

[78] Y.-H. Liu. Qualitative test and force optimization of 3-d frictional form-closure grasps using linear programming. *IEEE Transactions on Robotics and Automation*, 15(1):163–173, 1999.

[79] A. Madhani and S. Dubowsky. Motion planning of mobile multi-limb robotic systems subject to force and friction constraints. In *IEEE International Conference on Robotics and Automation*, pages 233–239, Nice, France, 1992.

[80] D. Maugis and M. Barquins. Fracture mechanics and the adherence of viscoelastic bodies. *Journal of Physics D: Applied Physics*, 11:1989–2024, 1978.

[81] K. Nagai and T. Yoshikawa. Dynamic manipultion/grasping control of multifingered robot hands. In *IEEE International Conference on Robotics and Automation*, volume 3, pages 1027–1033, Atlanta, GA, 1993.

[82] Y. Nakamura, K. Nagai, and T. Yoshikawa. Mechanics of coordinative manipulation by multiple robotic mechanisms. In *IEEE International Conference on Robotics and Automation*, pages 991–998, 1987.

[83] W. Neubauer. A spider-like robot that climbs vertically in ducts or pipes. In *IEEE International Conference on Intelligent Robots and Systems*, Munich, Germany, 1994.

[84] M. T. Northen and K. L. Turner. A batch fabricated biomimetic dry adhesive. *Nanotechnology*, 16(8):1159–1166, 2005.

[85] M. T. Northen and K. L. Turner. Meso-scale adhesion testing of integrated micro- and nano-scale structures. *Sensors and Actuators. A, Physical*, 130:583–587, 2006.

[86] M. T. Northen, K. L. Turner, C. Greiner, and E. Arzt. A hierarchical gecko-inspired switchable adhesive. In *Solid-State Sensors, Actuators, and Microsystems Workshop*, pages 43–46, Hilton Head Island, SC, 2006.

[87] A. Peressadko and S. Gorb. When less is more: Experimental evidence for tenacity enhancement by division of contact area. *The Journal of Adhesion*, 80(4):247–261, 2004.

[88] B. N. J. Persson. *Sliding Friction*. Springer, New York, 1998.

[89] B. N. J. Persson, O. Albohr, U. Tartaglino, A. I. Volokitin, and E. Tosatti. On the nature of surface roughness with application to contact mechanics, sealing, rubber friction and adhesion. *Journal of Physics: Condensed Matter*, 17(1):R1–R62, 2005.

[90] B. N. J. Persson and S. Gorb. The effect of surface roughness on the adhesion of elastic plates with application to biological systems. *Journal of Chemical Physics*, 119(21):11437–11444, 2003.

[91] E. Rabinowicz. The intrinsic variables affecting the stick-slip process. *Proceedings of the Physical Society*, 71(4):668–675, 1958.

[92] M.H. Raibert. *Legged Robots That Balance*. MIT Press, Cambridge, MA, 1986.

[93] M.H. Raibert. Running with symmetry. *The International Journal of Robotics Research*, 5:3–19, 1986.

[94] O. Reynolds. On the theory of lubrication and its application to mr. beauchamp tower's experiments, including an experimental determination of the viscosity of olive oil. *Philosophical Transactions of the Royal Society of London*, 177:157–234, 1886.

[95] N. Rizzo, K. Gardner, D. Walls, N. Keiper-Hrynko, T. Ganzke, and D. Hallahan. Characterization of the structure and composition of gecko adhesive setae. *Journal of The Royal Society Interface*, 3(8):441–451, 2006.

[96] R. Ruibal and V. Ernst. The structure of the digital setae of lizards. *Journal of Morphology*, 117(3):271–193, 1965.

[97] A. P. Russell. Integrative functional morphology of the gekkotan adhesive system (reptilia: Gekkota). *Integrative and Comparative Biology*, 42:1154–1163, 2002.

[98] Y. Sakagami, R. Watanabe, C. Aoyama, S. Matsunaga, N. Higaki, and K. Fujimura. The intelligent asimo: System overview and integration. In *IEEE International Conference on Intelligent Robots and Systems*, Lausanne, Switzerland, 2002.

[99] D. Santos, B. Heyneman, S. Kim, N. Esparza, and M. Cutkosky. Gecko-inspired climbing behaviors on vertical and overhanging surfaces. In *IEEE International Conference on Robotics and Automation*, Pasadena, CA, 2008. Submitted.

[100] D. Santos, S. Kim, M. Spenko, A. Parness, and M. Cutkosky. Directional adhesive structures for controlled climbing on smooth vertical surfaces. In *IEEE International Conference on Robotics and Automation*, pages 1262–1267, Rome, Italy, 2007.

[101] U. Saranli, M. Buehler, and D. Koditschek. Rhex: A simple and highly mobile hexapod robot. *International Journal of Robotics Research*, 20(7):616–631, 2001.

[102] A.R. Savkoor and G.A.D. Briggs. The effect of tangential force on the contact of elastic solids in adhesion. *Proc. of the Royal Society A: Mathematical, Physical and Engineering Sciences*, 356(1684):103–114, 1977.

[103] G. J. Shah and M. Sitti. Modeling and design of biomimetic adhesives inspired by gecko foot-hairs. In *IEEE International Conference on Robotics and Biomimetics*, pages 873–878, Shenyang, China, 2004.

[104] M. Sitti and R. S. Fearing. Nanomolding based fabrication of synthetic gecko foot-hairs. In *IEEE Conference on Nanotechnology*, pages 137–140, Piscataway, NJ, 2002.

[105] M. Sitti and R. S. Fearing. Synthetic gecko foot-hair micro/nano-structures as dry adhesives. *Journal of Adhesion Science and Technology*, 17(8):1055–1073, 2003.

[106] M. Sitti and R. S. Fearing. Synthetic gecko foot-hair micro/nano-structures for future wall-climbing robots. In *IEEE International Conference on Robotics and Automation*, Taipei, Taiwan, 2003.

[107] S. Skiena. *The Algorithm Design Manual.* Springer-Verlag, New York, 1998.

[108] R. Spolenak, S. Gorb, H. Gao, and E. Arzt. Effects of contact shape on the scaling of biological attachments. *Proceedings of the Royal Society A: Mathematical, Physical and Engineering Sciences*, 461(2054):305–319, 2005.

[109] P. Stewart. Geckos, 2003.

[110] R. Stribeck. Die wesentlichen eigenschaften der gleitund rollenlager - the key qualities of sliding and roller bearings. *Zeitschrift des Vereins Deutsher Ingenieure*, 46(38-39):1342–1348, 1432–1437, 1902.

[111] W. Sun, P. Neuzil, T. Kustandi, S. Oh, and V. Samper. The nature of the gecko lizard adhesive force. *Biophysical Journal: Biophysical Letters*, 89(2):L14–L17, 2005.

[112] D. Tabor. Surface forces and surface interactions. *Journal of Colloid and Interface Science*, 58(1):2–13, 1977.

[113] C. Thornton. Interparticle sliding in the presence of adhesion. *Journal of Physics D: Applied Physics*, 24:1942–1946, 1991.

[114] O. Unver, A. Uneri, A. Aydemir, and M. Sitti. Geckobot: A gecko inspired climbing robot using elastomer adhesives. In *IEEE International Conference on Robotics and Automation*, Orlando, FL, USA, 2006.

[115] M. Varenberg, A. Peressadko, S. Gorb, and E. Arzt. Effect of real contact geometry on adhesion. *Applied Physics Letters*, 89(12):121905, 2006.

[116] K. Waldron. Force and motion management in legged locomotion. *IEEE Journal of Robotics and Automation*, RA-2(4):214–220, 1986.

[117] D. Williams. *Characterization and Control of Multiple-Grasp Robotic Systems.* PhD thesis, Stanford University, 1995.

[118] D. Williams and O. Khatib. The virtual linkage: A model for internal forces in multi-grasp manipulation. In *IEEE International Conference on Robotics and Automation,* volume 1, pages 1025–1030, Atlanta, GA, 1993.

[119] W. Yan, L. Shuliang, X. Dianguo, Z. Yanzheng, S. Hao, and G. Xueshan. Development and application of wall-climbing robots. In *IEEE International Conference on Robotics and Automation,* Detroit, MI, USA, 1999.

[120] H. Yao and H. Gao. Mechanics of robust and releasable adhesion in biology: Bottom-up designed hierarchical structures of gecko. *Journal of the Mechanics and Physics of Solids,* 54(6):1120–1146, 2006.

[121] H. Yoshizawa, Y. Chen, and J. Israelachvili. Fundamental mechanisms of interfacial friction. 1. relation between adhesion and friction. *Journal of Physical Chemistry,* 97:4128–4140, 1993.

[122] B. Yurdumakan, N. Raravikar, P. Ajayan, and A. Dhinojwala. Synthetic gecko foot-hairs from multiwalled carbon nanotubes. *Chemical Communications,* 30:3799–3801, 2005.

[123] Y. Zhao, T. Tong, L. Delzeit, A. Kashani, M. Meyyapan, and A. Majumdar. Interfacial energy and strength of multiwalled-carbon-nanotube-based dry adhesive. *Journal of Vacuum Science and Technology. B, Microelectronics and Nanometer Structures,* 24(1):331–335, 2006.